SISSA
Scuola
Internazionale
Superiore di
Studi Avanzati

Neuroscience Area – PhD course in Neurobiology

Cytoskeletal scaffolds in neuronal development

Thesis submitted for the degree of "*Doctor Philosophiae*"

Candidate:

Simone Mortal

Advisor:

Vincent Torre

Academic Year 2018 - 2019

SISSA | Via Bonomea, 265 | 34316 | Trieste, Italy

Notes

The work described in this thesis was carried out at SISSA, Trieste, between November 2015 and October 2019. The data reported in the present thesis have been published, are submitted, or in preparation, as indicated.

Table of of contents

Abstract

Neuronal polarization is one of the most studied topics in neuroscience. In less than seven days neurites sprout out from the neuron, explore the surrounding environment and mature in axon or dendrites. This process is possible because the neuronal cytoskeleton can rapidly modify its architecture changing neuronal shape and length. Among all, two main proteins are involved: tubulin that supports the neurite elongation and builds a solid frame, while actin supports pathfinding. In this period of important cytoskeletal changes, it is possible to observe the actin waves (AW) that are highly dynamic structures emerging at the neurite base which move up to its tip, causing a transient retraction of the growth cone (GC). Since their discovery in 1988, there have been only few studies about AWs, usually linked to the neurite outgrowth and axon elongation.

In the present work, I used long term live cell imaging to investigate alternative roles of such cytoskeletal phenomena. I examined in details AWs and I concluded that they do not promote the neurite outgrowth and that neurites can elongate for hundreds of microns without the AWs. Super resolution nanoscopy indicates that myosin II shapes the GC like AWs structure. The highly concentrated myosin inside the wave can bend the tubulin that support the neurite provoking twists and kinks in the microtubular cytoskeleton. These tubulin twists (TT) cause the GC retraction and are completely abolished with the inhibition of myosin II, that compromises the AW morphology.

My results indicate that myosin II has an important role in the AWs dynamics and can bend the tubulin in a way that was not previously observed. Finally, we suggested a role for AWs and TTs in GC exploration and in neurite maturation.

Part of these results have already been published in Frontiers in Cellular Neuroscience in the article: Actin waves do not boost neurite outgrowth in the early stages of neuron maturation.

We have a second manuscript in preparation entitled “Tubulin twists drive Growth Cone retraction and promote tubulin mixed polarity”.

Introduction

Neurons are highly specialized cells, with different structural and functional districts. Neuronal polarization generates the fundamental asymmetries that are necessary for the function of neurons.

These cells have two unique regions at the end of the development: axons and dendrites, that extends from the soma to transmit signals through the nervous system. The axon is typically a long process that mediate information to other neurons releasing neurotransmitters. Dendrites are multiple processes that are specialized in receiving signals from other neurons with the neurotransmitter receptors located on the dendritic spines.

In this introduction I review the state of art of the field to set the background of my PhD work. Therefore, I will initially describe the neuronal polarization, then the role of individual cytoskeletal elements and of myosin II in force generation and motility will be discussed.

1.1 Neuronal polarization

In 1980s, Banker and colleagues established the first basic model for the neuronal polarization, that is still nowadays used, and divided the morphological changes of cultured neurons into five stages (Figure 1)[1].

Upon dissociation, although they have lost the original connectivity, hippocampal neurons re-grow their processes and recapitulate the morphological, synaptic and neurochemical features of their *in vivo* counterparts.

Shortly after plating, cells extend a motile lamellipodia around the cell body, an event known as **stage 1** of polarization. Next, during **stage 2**, the lamellipodia clusters at particular sites until small cylindrical processes, the ‘minor’ neurites, form. These neurites are highly dynamic, exhibiting periods of extension and retraction, until one of them initiates a sudden and sustained growth; this neurite becomes the neuron’s axon, and this event characterizes **stage 3**. Stage 2 and 3 are characterized by the presence of the growth cones located at the tips of

growing neurites. Growth cones (GCs) located at the tip of growing axons are the major motile structures guiding neuronal navigation. GCs are composed of a lamellipodium, flat (sheet-like) protrusion from which thin finger-like projections called filopodia emerge and are decorated by a variety of receptors able to sense the presence of appropriate chemical cues, such as guidance molecules[2]. During **stage 4**, the remaining minor neurites develop as dendrites, and in **stage 5**, synaptic specializations and contacts are established.

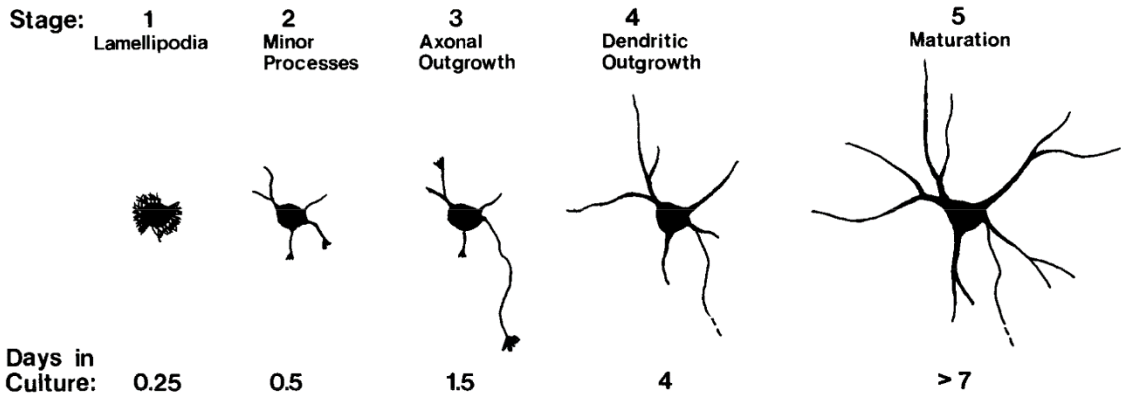

Figure 1. Stages of development of hippocampal neurons in culture. The approximate time at which cells enter each of the stages is indicated[3].

1.2 Neurite Cytoskeleton

The function, polarity, motility and efficiency of the cell are defined by intracellular filamentous networks that constitute the cytoskeleton. Structural proteins such as actin, tubulin and those of intermediate filaments by their polymerization and depolymerization can create highly ordered structures and orchestrate the driving forces of cell movement, neuronal shape and stability.

In this work I focused on the early stages of neuronal polarization (stage 2 and 3). In this time window, the main cytoskeletal proteins are actin and tubulin. On the other hand, neurofilaments are very important for the axonal support and function, but they can reach a significant number only after axon myelination[4]. For these reasons in the present work I will discuss only the role of Actin and Tubulin.

1.2.1 Actin

Actin is one of the most plentiful protein and is involved in multiple processes, such as: membrane protrusion, cell division and morphogenesis. In developing neurons, actin cytoskeleton is essential to generate mechanical forces required for many cellular functions, like neurite outgrowth, cell motility, active shape control and exocytosis.

Actin is an enzyme that slowly hydrolyzes ATP, it is able to make interactions with a lot of other proteins and performs a variety of functions. However, actin is codified by a gene family, with more than 30 elements, therefore there is not a unique type of actin. These genes give rise to α-actin, which is usually found in contractile structures, β-actin localized at the leading edge of cells that project their cellular structures as their means of mobility and γ-actin which is peculiar of the stress fibers.

In the cell is possible to found actin in two different forms: the globular actin, *G-actin* and the polymerized filamentous form, called *F-actin* (Figure 2)[5].

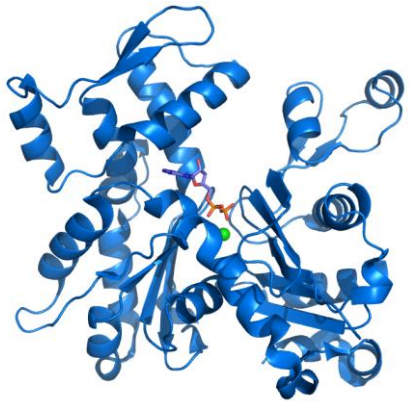

Figure 2. Ribbon diagram of G-actin. ADP bound to actin's active site (multi color sticks near center of figure) as well as a complexed calcium dication (green sphere) are highlighted[5].

G-actin has a globular structure, formed by two domains separated by a cleft which is a center of enzymatic catalysis that binds ATP and Mg^{2+} and hydrolyzes ATP to ADP + Pi. G-actin can operate only when it is bound with ADP or ATP, but the ATP form is predominant in cells with actin in its free state[6].

F-actin is a levorotatory filament with a rotation of 166° around the helical axis, it is a polarized structure because all the subunits point towards the same end. Therefore, the (-) end has an actin with its ATP binding site exposed, while the (+) end is where the cleft is directed towards the adjacent monomer[6,7].

1.2.1.1 Growth cones

During the development of the nervous system, neurons extend multiple neurites, through a complex environment to reach their final destinations. At the tip of each neurite is the growth cone (GC). They were firstly observed on fixed cells by a famous Spanish scientist Santiago Ramòn y Cajal in 1890. GCs are located at the tip of neurites and are composed by filopodia and lamellipodia.

The GC builds its cytoskeleton to move forward and turn continuously progressing through three stages of advance, influenced by environmental factors: protrusion, engorgement and consolidation[8]. To understand the motility of the GC and the mechanism that influence its way it is essential to understand the cytoskeletal mechanisms that move forward and can be affected asymmetrically.

GC have fine extensions finger like called filopodia, they contain bundles of actin filaments that can extend several micrometers beyond the edge of the growth cone. Between filopodia there are flat regions of dense actin meshwork called lamellipodia, these areas appear like a thin veil and usually new filopodia emerge from inter filopodia veils[9–11].

In the GC we can define three regions: the peripheral domain, the transitional domain and the central domain[12] (Figure 3). The peripheral domain is the external part of the GC, it is mainly composed by an actin-based cytoskeleton. Filopodia play an important role in sensing guidance cues while lamellipodia are responsible for the advancement of the GC. Transiently microtubules can enter in the peripheral region via a process called dynamic instability[13]. The central domain is in the central part of the GV and contains a dense microtubule cytoskeleton and is generally thicker. It is enriched in cellular organelles such as

mitochondria and exocytotic vesicles. The transitional domain is the region that is located where the actin filaments from the peripheral domain and the microtubules from the central domain overlap at the interface.

Although actin might not be the only propellent for the neurite outgrowth, it plays a central role in the advancement and growth cone exploration. It has been observed that F-actin retrograde flow is directly related to growth cone motility. This movement is driven both by contractility of the motor protein myosin II which seems to interact through a protein-protein link in the transition (T) zone and the push from F-actin polymerization in the peripheral (P) domain[12]. Myosin II activity can create compressions across the T zone circumference that cause buckling of the F-actin bundles, this might be enhanced by pushing from the leading-edge actin polymerization. This leads to bundle severing, then the actin fragments can be recycled into individual actin subunits G-actin, available for further actin polymerization at the leading edge[14].

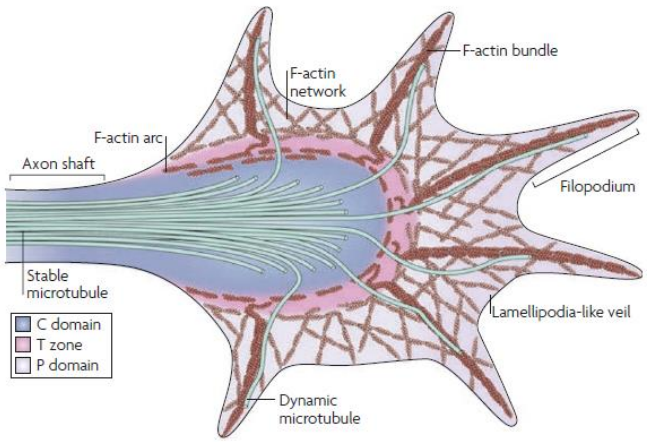

Figure 3. The structure of the growth cone[8].

How does the growth cone advances using actin as an engine? This was explained by Mitchison and Kirschner with the “clutch hypothesis” also called substrate-cytoskeletal coupling model. They proposed the growth cone receptors bind an adhesive substrate to form a complex that works like a molecular clutch, they are mechanically coupled to the F-actin flow, that prevent the retrograde flow and drives actin-based forward protrusion of the growth cone on the adhesive substrate[15,16]. Filopodia are considered the guidance sensors at the front line of

the growth cone, in fact they have a major role in the detection of the substrate adhesive contacts during the environmental exploration.

Commonly the GC advancement is divided into three stages: protrusion, engorgement and consolidation. The binding of growth cone receptors activates intracellular signalling cascade, starting the formation of a molecular “clutch” that connects the actin cytoskeleton to the substrate. During protrusion, the clutch gets stronger, slowing down locally the F-actin retrograde flow. This fix the actin to the substrate, as F-actin polymerization continues in front of the clutch site and lamellipodia and filopodia of the peripheral (P) domain move forward to extend the leading edge. Engorgement starts after the actin behind the clutch is removed, F-actin are reoriented from the C domain to the site of new growth and the microtubles in the C domain invade this region[17].

We have described the cytoskeletal machinery that drive the progression of the growth cone, but growth cone pathfinding does not consist only in moving forward. There are a multiple signals that participate to the guidance of the growth cone, including kinases, phosphatases and calcium ions, our most comprehensive is the Rho family of GTPases, a group of molecules that control the cytoskeleton rearrangement with the guidance of the signalling receptors[18]. Rho GTPases are a subfamily of the Ras superfamily. Cdc 42, Rac 1 and RhoA regulates the F-actin assembly and disassembly and the actomyosin complex[19].

1.2.1.2 Actin Waves

In 1988, Ruthel and Banker documented for the first time a growth cone-like structure that moves through the neurites in cultures of immature hippocampal neurons[3,20] (Figure 4). These cultures provide an excellent model to analyse these events, in fact these events can be easily identified along the neurite shaft, forming lamellipodia and filopodia, as in the neuronal growth cone.

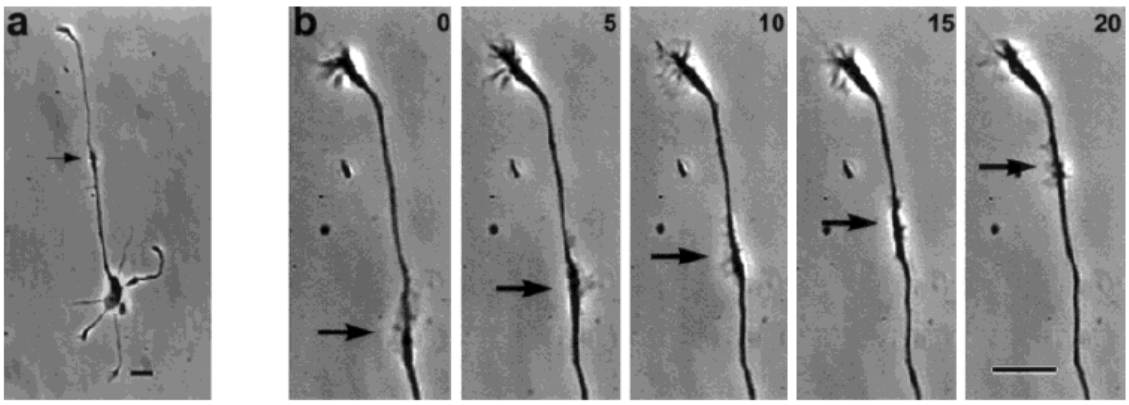

Figure 4. Time-lapse series showing the progression of a wave along an axon a: A typical neuron is pictured at approximately 34 h in culture. A growth-cone-like structure, or "wave," (arrow) was present on the axonal shaft. The cell was not in contact with any other cells within the culture, indicating that this structure was not the growth cone of a fasciculating axon. b: The wave is shown at higher magnification in successive 5-min intervals taken from a time-lapse recording of the wave as it moved along the axon. The wave (arrow) was approximately the size of the growth cone and moved unidirectionally toward the tip of the axon at a fairly constant rate, about 2 μm/min. The wave's lamellipodia and filopodia extended and retracted as it advanced toward the tip. Relative times in minutes are indicated in the upper right corner. Scale bars = 10 μm.

Actin waves are observed mainly during neuronal polarization and are dependent on actin polymerization. They emerge at the cell body and travel along the immature neurites migrating toward the tip at an average rate of 3 μm/min. In addition, these structures are enriched with actin filaments and actin-related molecules, such as cortactin, shootin1, GAP-43, ezrin, cofilin, LIM-kinase, Slingshot, phosphatidylinositol (3,4,5)-trisphosphate (PIP_3), Arp2/3, Cdc42, Rap1, Rac1, and doublecortin (DCX)[21–23].

Ruthel and Banker, in their seminal paper, proposed that the role of actin waves is associated to transport proteins to the growth cone at the tip of an extending neurite. Indeed, the arrival of an actin wave increase the actin concentration in the GC[20]. As in the GC, the actin associated proteins cortactin, cofilin, Arp2/3, ezrin, shootin1 and Slingshot colocalize and move within the AW[24,25]. The actin migration is anterograde and is characterized by an anterograde movement of actin and actin filament binding proteins. The actin filaments in AWs migrate to the GC through a directional process of polymerization and depolymerization. The actin filament binding proteins comigrate through a cycle of association, dissociation and directional movement with the filaments, given by passive diffusion from the region of depolymerizing to the polymerizing ends. Therefore,

from a district with high concentration of actin and actin associated proteins, depolymerizing ends, to a district with low concentration, polymerizing ends, allowing the recycling of depolymerized molecules. This mechanism can translocate actin subunits and actin binding proteins to the growth cone and it is very different from the largely studied model involving motor proteins such as dynein and kinesin[26,27].

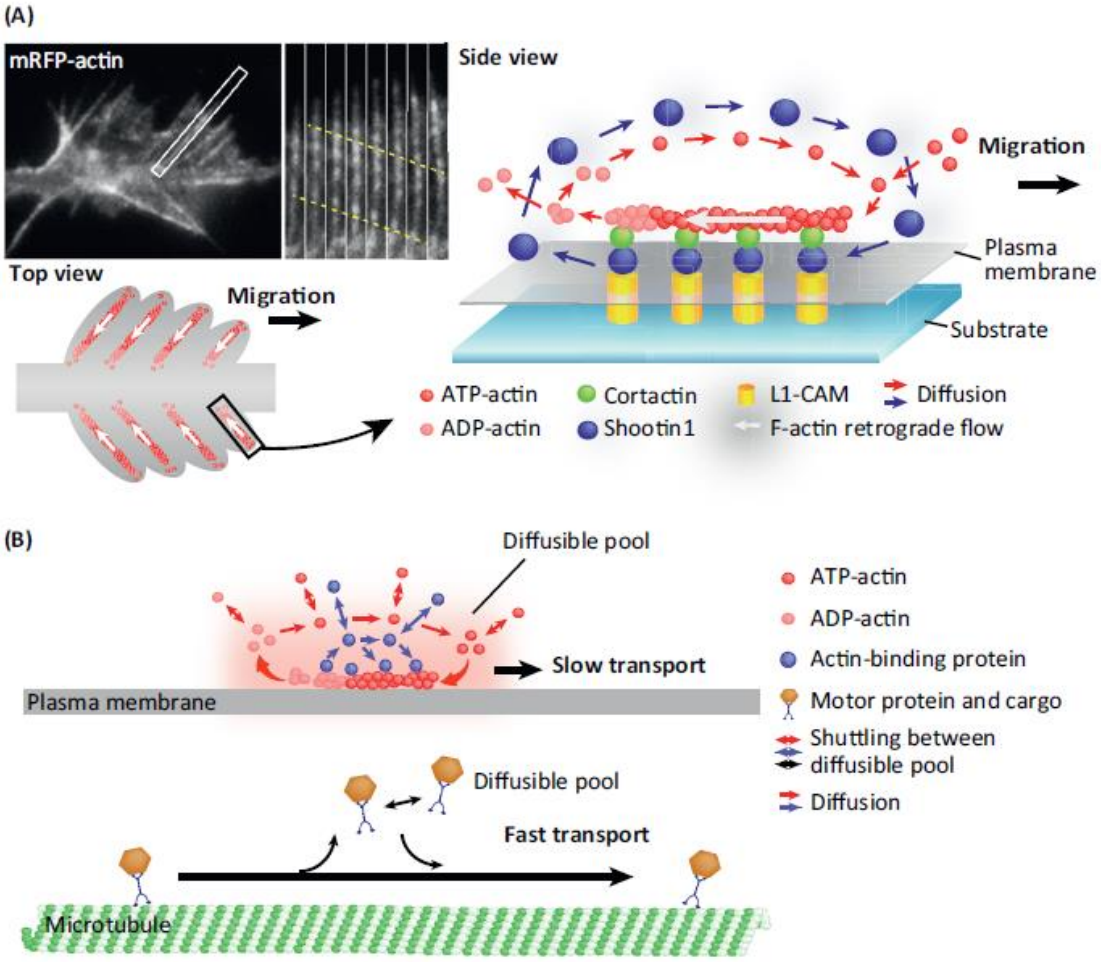

Figure 5. Directional Assembly–Disassembly Mechanism for Actin Wave Migration and Protein Transport along Axons. (A) Mechanism for axonal actin wave migration. The upper left panel shows a fluorescent speckle image of mRFP-actin in a wave. A kymograph of the indicated rectangular region at 5-second intervals is shown to the right. Actin filaments polymerize at the leading edge, accompanied by their retrograde flow (dashed yellow lines). The illustrations describe the molecular mechanism. The actin filaments in axonal actin waves undergo directional polymerization and depolymerization, in which the polymerizing ends are on average oriented toward the neurite tip (top view, lower left), and are anchored to the plasma membrane and substrate through the linker clutch molecules shootin1 and cortactin and the cell adhesion molecule L1-CAM (side view, right). As actin filaments in the wave are anchored in parallel with the membrane, directional polymerization/depolymerization of actin filaments leads to wave migration on the membrane toward the neurite tip. (B) Axonal actin waves as a new type of intracellular transport system.

Arrays of actin filaments in a wave migrate through directional polymerization and depolymerization (upper panel). Actin filament-binding proteins comigrate with the actin filament array through cycles of dissociation, directional diffusion, and association with the filaments. The transport velocity is approximately 100 times slower than that of motor protein-based transport (lower panel). Although individual actin subunits and actin-associated proteins may shuttle between the reutilizing pool and the other diffusible pool (double arrows), net amounts of actin and actin-associated proteins that are equivalent to those constituting the actin wave are translocated by the directional diffusion. Scale bar, 5 mm (A).

AWs are usually associated with neurite outgrowth, in fact live imaging experiments have revealed that the arrival of AWs at the GC produce neurite protrusion, that is preceded by a GC retraction. In addition, waves after their arrival can promote neurite branching and increase of the growth cone size. In this way, AWs play an important role in the maintenance of the GCs[20,21,24,28]. Furthermore, recently it was reported that waves enhance microtubules polymerization along neurites and transiently enlarge the neurite shaft, promoting the microtubule polymerization and kinesin driven transport for neurite outgrowth[29].

1.2.2 Tubulin

During all the different stages of neuronal development, besides the actin cytoskeleton, the assembly, organization and remodelling of the microtubule (MT) cytoskeleton are essential. MTs provide tracks for intracellular transport and vesicular release, act as signalling devices, or generate cellular forces[27,30–32].

MT cytoskeleton have a huge important in neuronal development and to understand that, it is sufficient to consider the wide range of nervous system abnormalities and several human neurodevelopmental disorders linked to altered microtubules mediated processes. In addition, several developmental problems are linked to mutations in microtubule related genes that encode for microtubule-associated proteins (MAPs), MT motor associated regulators or MT severing proteins[33,34].

Although many of the molecular mechanisms regarding the assembly of microtubules remain largely unknow, in the last decades the neuronal MT architecture has been studied in detail using electron microscopy and live cell imaging[35,36].

The MT structure is built from heterodimers of α and β tubulin, bound in a head to tail relation to form polarized structures that associate laterally to form a hollow tube, with a diameter of 25 nm[30]. MTs are very dynamic structures, they continuously switch between growth and disassembly, in a process called dynamic instability, which allow individual MT to explore cellular regions and retract if it does not find the proper environment[37].

MT dynamics are regulated by the properties of tubulin, free tubulin binds GTP, which is hydrolysed after incorporation into MT structure. The growth of the MT promoted by the GTP cap, in fact, GDP-tubulin tends to destabilize the architecture, therefore stable growth is believed to depend on the presence of a GTP-tubulin cap at the MT plus end[38]. In this model, the loss of the cap will result in a collapse of the structure, called catastrophe.

At the tip of the microtubule there is a minus end and a plus end, these can grow and depolymerize, but the two dynamics are very different. The plus end, terminated by β-tubulin, grows with polymerization of the subunits, undergoes catastrophe more frequently and is a crucial site for regulating MT dynamics[39]. Plus end tracking proteins (+TIPs) accumulate at the ends of growing MTs and control different aspects of neuronal development and function. Nevertheless, the polymerization of microtubule based structures not only depends on +TIPs, but also requires many factors, such as MAPs, motor proteins and tubulin isotypes[30].

Relying on different mode of action, five groups of proteins can be deduced from the microtubule related proteins. The proteins that can bind to MT ends and regulate their dynamics, that contains the +TIPs and minus end targeting proteins (-TIPs)[30,39]. The group of proteins that bind to the MT lattice and can stabilize or crosslink MTs[40,41]. The third group contains proteins that modulate the MT numbers, enzymes that sever MTs and regulators of the nucleation[42,43]. The fourth group includes the kinesin and dynein families that generate forces and move directionally along MTs[44]. The last group comprises tubulin folding cofactors and tubulin modifying enzymes that through post translational modifications can generate distinct MT subtypes[45] (Figure 6).

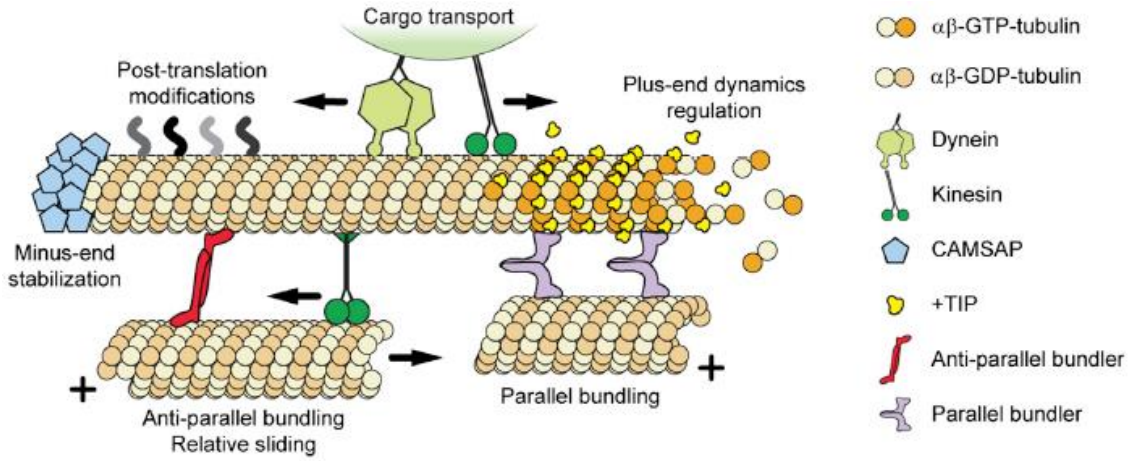

Figure 6. Cartoon illustrating how different microtubule-related proteins interact with microtubules[46].

1.2.2.1 Neuronal Microtubule Cytoskeleton

Neuronal MTs are involved in the morphological changes during the phases of neuronal development, in the intracellular transport and synapse formation.

For neurons is fundamental to have an active and efficient transport mechanism, to properly distribute many cellular components and establish signalling pathways. Kinesin and dynein families are the transporters that travel along the neuronal MTs. These proteins carry many types of neuronal cargo, including synaptic vesicles, neurotransmitter receptors, organelles, cell adhesion molecules, cell signalling molecules and mRNAs. In addition, cargo-adaptor proteins, regulatory molecules and MT cytoskeleton play an important role in the delivering of the cargo in the correct location[44].

The selective presence of minus end in dendrites enable the dynein to selectively transport the cargoes in the dendrites. On the other hand, kinesin 1 has been shown to selectively transport cargoes into the axon, formed by plus end MT out oriented[47,48].

MTs are very important also for morphological transitions that occur during neuronal development, such as neurite initiation, migration, polarization and differentiation.

Neuronal migration is a complex sequence of motile and morphogenetic events, in which neurons extend leading process and translocate the nucleus into this

process. These movements are driven by actin and MT: actin promotes neuronal migration by propulsive contractions at the cell rear and MTs which are anchored to the centrosome extends the leading process and form a cage like structure around the nucleus. Cytoskeletal forces in the leading edge can pull the centrosome into the proximal part of the leading process and move the nucleus in the direction of migration[49].

Neurite initiation and outgrowth begins with the breakage of the round shape of newborn neurons by sprouting neurites. These neurites are formed by bundled MTs and a growth cone which mediate the pushing and pulling forces that contribute to membrane protrusion[50,51].

MT stabilization plays a key role in the a*xon differentiation* during neuronal polarization. The increased MTs stability in the future axon lead to kinesin mediated flow and contribute to determining the axon formation. The whole mechanism of axon differentiation remains unknown, but internal signals like Golgi position, centrosome localization and cytoskeleton architecture could initiate a local imbalance inside the MT network and stabilize MTs in only one of the neurites[47,52].

During a*xon elongation* MT cytoskeleton participates in functional interactions with adhesion complex and actin, that with +TIPs can modulate the MT dynamics and stability[47]. In addition, to MT polymerization recent studies found that translocation of whole MT bundles in the axon contribute to the axon elongation, presumably generated by molecular motors[53,54].

Dendritic spine morpho dynamic and *synapse functioning* are linked directly to MT dynamics, in fact, evidences suggest that MTs are associated with transient changes in spine shape, such as the formation of the spine and the spine enlargement. MTs entire into the spines are regulated by neuronal activity and brain derived neurotrophic factor (BDNF), these MTs with microtubule dependent motors are responsible to drive postsynaptic cargoes into spines[55].

MTs architectures are organized in bundles, axonal cross sections are usually composed by 10-100 MTs. In many cell types, MTs are nucleated at the microtubule organizing centre (MTOC), such as the centrosome, but they can be generated even in other position, such as the Golgi apparatus or along existing

MTs, where not all the minus ends are directed towards a central organization centre[46,56]. In newborn neurons the centrosome first acts as an active MTOC, but with time this activity is completely lost. Electron microscopy and super resolution studies have shown that MTs are not anchored to the centrosome and often the ends are free in the mature neuron (Figure 7).

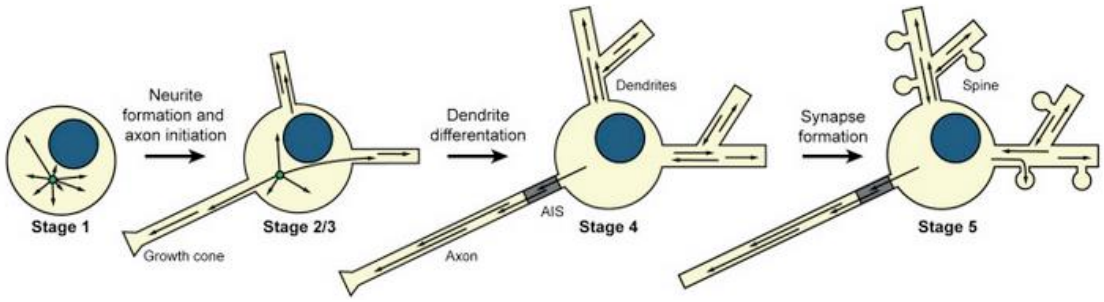

Figure 7. Changes in Microtubule Organization during Development. After their final division, neurons transit through several developmental stages and the MT cytoskeleton has a pivotal role at all stages. During these stages, the MT organization changes from a radially centrosome-based and largely plus-end outward-oriented network to an acentrosomal network with uniform orientations in the axon and mixed orientation in dendrites.

Because most MTs do not emerge from the MTOC, their relative orientations can vary. Electron microscopy with hook decoration technique revealed that MT orientations in axons and dendrites have different patterns[35]. Whereas in axons we can observe uniformly plus end out oriented MTs, in proximal dendrites the orientations of MTs are non-uniformly, in fact MTs are half plus end out and half minus end out.

This different distribution in MTs orientation contribute to polarize the trafficking to dendrites or axons, allowing dyneins to act as a anterograde motor in dendrites[57].

1.2.3 Force generation protein non-muscle myosin II

Myosins are mechanoenzymes that generate forces through the interaction with actin filaments and the hydrolyzation of ATP. These proteins can influence the structure and the dynamics of actin cytoskeleton and affect the localization of cellular components[58,59].

There are 35 known classes of myosin and humans have 40 myosin genes that produce 13 classes (I, II, III, V, VI, VII, IX, X, XV, XVI, XVIII, XIX and XXXV)[60].

Here we will focus on a neuronal myosin that participate in growth cone and actin wave remodelling, the non-muscle myosin II (NMII).

Class II myosins are composed by six monomers, two myosin heavy chains and four calmodulin-related light chains. A peculiar feature of myosins II is their ability to assemble into bipolar filaments that contain 14 -20 copies (NMII) or several hundred copies (sarcomeric myosin II) of hexameric molecules with actin binding heads oriented towards opposite ends[61,62].

NM II is fundamental in cell migration, protrusion, cytokinesis and cell adhesion. It mediates the retrograde flow of lamellar actin and attenuates cell protrusion and is very important in the recruitment of focal adhesions proteins.

The actin retrograde flow in the neuronal GC determine the growth cone protrusion or retraction, myosin is the key player in this phenomenon with the rate of actin polymerization. To do the retrograde flow myosin II binds actin filaments, forming the actomyosin complex which exert a contractile force on anti-parallel actin filaments. Furthermore, NMII mediates adhesion with actin and adhesion related proteins such as integrins that are clustered at the end of these actin filaments[62].

In neurons, there are three isoforms of NMII: *myosin II A, B, C*. All these isoforms have a similar structure and properties, but they have different functions and localizations. *Myosin II B* is the predominant form in the nervous system, it promotes the neurite outgrowth, modulate dendritic spines morphology and synaptic function. On the other hand, *myosin II A* is required to maintain tensile adhesion and favour the neurite retraction. *Myosin II C* is the least represented isoform and it is involved in the regulation of cell membrane extension and the formation of focal contacts in collaboration with *Myosin II A* and *B*[61,63].

A further demonstration of the importance that myosin II plays an important role in the neuronal cytoskeleton is confirmed by the observation that inhibition of myosin II with blebbistatin promote the reorganization of both actin and MTs in the GC[64].

Blebbistatin is a myosin II specific inhibitor, it is used in research for NMII in neurons and for skeletal muscle myosin. Blebbistatin blocks the myosin ATPase activity, it binds between the nucleotide binding pocket and the actin binding cleft

of myosin, relaxing the acto-myosin filaments. The blebbistatin was found to promote the outgrowth of neurites in neurons and it is widely used to study the involvement of myosin II in the cytoskeleton dynamics[64,65]. On the other hand, the 4-hydroxyacetophenone (4-HAP), a myosin II activator was recently discovered and this compound can alter the mechanics of myosin II heavy chain phosphorylation in an independent manner, specifically targeting the myosin II power stroke of the myosin II ATPase cycle[66].

Results

Neuronal polarization is a very complex and large field of research, usually people try to understand the small changes in the protein levels or study the colocalization of particular proteins. To do that they commonly use molecular biology or fixed preparations of developing neurons at different stages, mainly alter 5 DIV when you can start to see the firsts mature axons. We thought that it is necessary a more physiological approach to observe protein interactions and avoid fixation artefacts. Starting from that we started to study the period before the axonal maturation and we focused our attention on a phenomenon that is highly spectacular and surprisingly poor studied, the actin waves. Our team performed live imaging experiments to study these particular events and in doing that we find out that some dynamics of these actin waves were not correctly characterised and that they can have a fundamental relevance in the neurite maturation.

2.1 Actin Waves Do Not Boost Neurite Outgrowth in the Early Stages of Neuron Maturation

Simone Mortal, Federico Iseppon, Andrea Perissinotto, Elisa D'Este, Dan Cojoc, Luisa M. R. Napolitano and Vincent Torre

Original Research ARTICLE

Front. Cell. Neurosci., 18 December 2017 |
https://doi.org/10.3389/fncel.2017.00402

frontiers in Cellular Neuroscience

ORIGINAL RESEARCH
published: 18 December 2017
doi: 10.3389/fncel.2017.00402

Actin Waves Do Not Boost Neurite Outgrowth in the Early Stages of Neuron Maturation

Simone Mortal[1†], Federico Iseppon[1†], Andrea Perissinotto[1], Elisa D'Este[2], Dan Cojoc[3], Luisa M. R. Napolitano[1] and Vincent Torre[1*]*

[1] Neurobiology Department, International School for Advanced Studies, Trieste, Italy, [2] Department of NanoBiophotonics, Max Planck Institute for Biophysical Chemistry, Göttingen, Germany, [3] Optical Manipulation Lab, Istituto Officina dei Materiali (CNR), Trieste, Italy

During neurite development, Actin Waves (AWs) emerge at the neurite base and move up to its tip, causing a transient retraction of the Growth Cone (GC). Many studies have shown that AWs are linked to outbursts of neurite growth and, therefore, contribute to the fast elongation of the nascent axon. Using long term live cell-imaging, we show that AWs do not boost neurite outgrowth and that neurites without AWs can elongate for several hundred microns. Inhibition of Myosin II abolishes the transient GC retraction and strongly modifies the AWs morphology. Super-resolution nanoscopy shows that Myosin IIB shapes the growth cone-like AWs structure and is differently distributed in AWs and GCs. Interestingly, depletion of membrane cholesterol and inhibition of Rho GTPases decrease AWs frequency and velocity. Our results indicate that Myosin IIB, membrane tension, and small Rho GTPases are important players in the regulation of the AW dynamics. Finally, we suggest a role for AWs in maintaining the GCs active during environmental exploration.

Keywords: actin waves (AWs), growth cones (GCs), Myosin IIB, β-cyclodextrin, RhoGTPases

OPEN ACCESS

Edited by:
Keith Murai,
McGill University, Canada

Reviewed by:
Kyle Miller,
Michigan State University, United States
Annie Andrieux,
Commissariat à l'Énergie Atomique et aux Énergies Alternatives, France

***Correspondence:**
Luisa M. R. Napolitano
napolita@sissa.it
Vincent Torre
torre@sissa.it

†These authors have equally contributed to this work.

***Received:** 21 September 2017*
***Accepted:** 01 December 2017*
***Published:** 18 December 2017*

Citation:
Mortal S, Iseppon F, Perissinotto A, D'Este E, Cojoc D, Napolitano LMR and Torre V (2017) Actin Waves Do Not Boost Neurite Outgrowth in the Early Stages of Neuron Maturation. Front. Cell. Neurosci. 11:402. doi: 10.3389/fncel.2017.00402

INTRODUCTION

The actin cytoskeleton is a highly dynamical system that facilitates the transduction of mechanical signals and generates the intracellular forces required for many cellular functions such as cell motility, polarization, active cell shape control, neurite outgrowth, and exocytosis (Madden and Snyder, 1998; Morales et al., 2000; Pollard and Borisy, 2003). Growth Cones (GCs) are located at the tip of neurites and are composed of a veil-like structure, referred to as the lamellipodium, from which thinner filopodia emerge (Lowery and Van Vactor, 2009; Dent et al., 2011). A characteristic feature of all these processes is the dynamical assembly of filamentous actin (F-actin) from its subunits (G-actin) that sustains a constant and rapid reshaping of the actin network. Actin Waves (AWs) are growth cone–like structures that emerge at the base of neurites, slowly migrating up to their tips with a speed of ∼2–3 μm/min, flaring the plasma membrane during transit (Ruthel and Banker, 1998, 1999; Flynn et al., 2009; Katsuno et al., 2015). AWs have been observed mainly in growing neurons and are present in cultured primary hippocampal neurons as well as in organotypic slices (Ruthel and Banker, 1998; Flynn et al., 2009; Katsuno et al., 2015). They have been proposed to be associated with outbursts of neurite growth and to constitute, in concert with microtubules, a transport mechanism that brings actin and actin associated proteins toward the GC (Flynn et al., 2009; Katsuno et al., 2015; Winans et al., 2016).

An important component of the actin dynamics is thought to be the acto-myosin force-generating machinery. Myosin II, a central player during cell contraction, is an actin-dependent molecular motor moving toward the plus (barbed) end of the actin filament. Myosin IIA and IIB are the most prominent type II myosin expressed in neurons migrating within the CNS (Golomb et al., 2004). In particular, Myosin IIB is required for maintaining normal growth cone shape and traction force, polarization size, and actin organization (Bridgman et al., 2001). Although the role of Myosin II in the rear of motile cells is conventionally associated with mechanical force generation and contraction, it is now clear that Myosin IIB also has a specific role in driving actin network disassembly (Wilson et al., 2010). Over the last years it has also become clear that Myosin II is regulated by the Rho family members of small GTPases (Rac, RhoA, and Cdc42). In general, RhoA/Rho-kinase (ROCK) activates Myosin II contractility, whereas its effector PAK often regulates Myosin II negatively decreasing cell contractility (Lee et al., 2010). The Rho GTPases act as molecular switches to control signal transduction pathways by cycling between a GDP-bound, inactive form, and a GTP-bound, active form (Raftopoulou and Hall, 2004). They have also been considered as putative Nucleation Promoting Factors (NPFs) (Weiner et al., 2007; Holmes et al., 2012) that modulate actin filament nucleation influencing many aspects of the cell behavior such as cell migration. Indeed, Cdc42 induces actin polymerization to generate filopodia often seen at the front of migrating cells, while Rac has a key role in generating a protrusive force through the localized polymerization of actin (Nobes and Hall, 1995; Raftopoulou and Hall, 2004; Ridley, 2011). Consistent with this view, it is not surprising that the use of a Raichu FRET reporter (Komatsu et al., 2011) has revealed an increase of Rac activity in and behind the AWs showing a role for Rac in generating the AWs (Winans et al., 2016). In addition, Machacek et al (Machacek et al., 2009) showed a tight correlation between GTPases activation and morphological edge dynamics and in (Wu et al., 2013), waves of Cdc42 proved to be correlated in both space and time with waves of F-actin.

We investigated the function of AWs and their regulating mechanisms using live cell-imaging. Our work aimed to solve three main issues: (1) Do AWs really promote neurite outgrowth? (2) Which is the AWs subcellular organization and to what extent AWs and GCs are similar? (3) What is the mechanism allowing the migration of AWs along the neurites? Indeed, AWs might create tension and exert pulling forces along the neurites (Ruthel and Banker, 1999; Lamoureux et al., 2002; Tomba et al., 2017). In the present manuscript, we use STED nanoscopy and live-cell imaging to tackle these questions.

Our results show that AWs do not contribute to neurite outgrowth regardless of the substrates used (matrigel/laminin, poly-D-lysine, poly-L-ornithine). We also observed that, in accordance with Flynn et al. (2009), as an AW approaches the distal neurite, the GC moves closer to the incoming AW and merges with it. Furthermore, our data highlight that, despite the similarities in shape and appearance, AWs and GCs exhibit a different response to the blebbistatin, a cell permeant inhibitor of Myosin II (Kovács et al., 2004), that leads to a substantial collapse of the GC but not of the AW. We then investigated the cross-talk between AWs and Rho GTPases and our data support the idea that cytoskeletal dynamics and Rac1/Cdc42 activities are tightly coupled at subcellular levels.

MATERIALS AND METHODS

DNA Constructs

mCherry-Lifeact-7 was a gift from Michael Davidson (Addgene plasmid #54491) and was verified by full-length sequencing.

Primary Hippocampal Neuron Culture and Transfection

Hippocampal neurons from Wistar rats (P2-P3) were prepared in accordance with the guidelines of the Italian Animal Welfare Act, and their use was approved by the Local Veterinary Service, the SISSA Ethics Committee board and the National Ministry of Health (Permit Number: 2848-III/15) in accordance with the European Union guidelines for animal care (d.l. 26, March 4th 2014 related to 2010/63/UE and d.1. 116/92; 86/609/C.E.). The animals were anesthetized with CO_2 and sacrificed by decapitation, and all efforts were made to minimize suffering. The coverslips were coated with 50 μg/ml poly-L-ornithine (Sigma-Aldrich, St. Louis, MO, USA) overnight and with Matrigel before cells seeding (Corning, Tewksbury MA, USA). In control experiments, the coverslips were coated with 50 μg/ml poly-L-ornithine (Sigma-Aldrich, St. Louis, MO, USA) overnight or 0.5 mg/ml poly-D-lysine (Sigma-Aldrich, St. Louis, MO, USA) for 1 h at 37°C. Dissociated cells were plated at a concentration of 4×10^4 cells/ml in Minimum Essential Medium (MEM) with GlutaMAX™ supplemented with 10% Fetal Bovine Serum (FBS, all from Invitrogen, Life Technologies, Gaithersburg, MD, USA), 0.6% D-glucose, 15 mM Hepes, 0.1 mg/ml apo-transferrin, 30 μg/ml insulin, 0.1 μg/ml D-biotin, 1 μM vitamin B12 (all from Sigma-Aldrich), and 2.5 μg/ml gentamycin (Invitrogen). The neuronal cultures were maintained in an incubator at 37°C, 5% CO_2, and 95% humidity. Hippocampal neurons were transfected immediately or 24 h after dissection with the LifeAct plasmid using Lipofectamine 3000® reagent (Invitrogen) following the manufacturer's protocol, and imaged 1 day after transfection. To stain the membrane, cells were incubated with Vybrant DiI (5 μL/mL) (Thermofisher) for 20 min at 37°C. SiR-Actin (Spirochrome) was used at 200 μM, incubating it for 30 min at 37°C.

Drug Application

Blebbistatin (Sigma) and β-cyclodextrin (Sigma) were used at a final concentration of 20 and 250 μM respectively. ML141 (TOCRIS bioscience, Bristol, UK) was used at a final concentration of 10 μM (for low concentration experiments) and 30 μM (for high concentration experiments); EHT1864 (TOCRIS) was used at a final concentration of 10 μM. All inhibitors used were added after about 60–90 min of imaging, and the acquisition continued for at least 90 min after addition, at the conditions described in paragraph Live Cell Imaging.

STED Nanoscopy

Hippocampal neurons prepared from P0-P2 Wistar rats were plated on Poly-ornithine/Laminin coated coverslips. At DIV 1, cells were washed with PBS and fixed in 4% PFA and 0.25% Glutaraldehyde in PHEM buffer (60 mM PIPES, 25 mM HEPES, 10 mM EGTA, 2 mM $MgCl_2$, pH 6.9) for 20 min at room temperature, quenched with ammonium chloride and glycine (100 mM each) for 5 min, permeabilized with 0.1% Triton X-100 for another 5 min and blocked in PBS supplemented with 1% BSA for 30 min. Primary antibodies against β-III Tubulin (Abcam, cat. ab7759), Myosin-IIB (Sigma, cat. M 7939) and Actin (Phalloidin) were incubated in PBS for 1 h or overnight at 4°C. Secondary antibodies (sheep anti-mouse, Dianova, cat. 515-005-003; goat-anti-rabbit, Dianova, cat. 111-005-003) were labeled with STAR580 (Abberior, cat. 1-0101-005-2), and Alexa 488 secondary antibodies (Invitrogen, goat anti-mouse IgG, cat. A11001; goat anti-rabbit, cat. A-11008) were used for confocal imaging. Phalloidin was coupled to STAR635 (Abberior, cat. 2-0205-002-5). Both secondary antibody and phalloidin incubations were performed in PBS for 1 h at room temperature or overnight at 4°C. Samples were then mounted in Mowiol supplemented with DABCO. Imaging was performed on a two-color Abberior STED 775 QUAD scanning microscope (Abberior Instruments GmbH, Göttingen, Germany) equipped with 488 nm, 561 nm, and 640 nm pulsed excitation lasers, a pulsed 775 nm STED laser, and a 100x oil immersion objective lens (NA 1.4).

Live Cell Imaging

Live cell imaging experiments were performed on an epi-fluorescence microscope (Olympus IX-83, Olympus) equipped with LED illumination ($\lambda = 590$ nm for LifeAct-mCherry; $\lambda = 530$ nm for Vybrant DiI; $\lambda = 660$ nm for SirActin, all purchased from Thorlabs). During all imaging experiments cells were kept at 37°C, 5.0% CO_2, 95% humidity by using an imaging chamber incubator (Okolab, Pozzuoli, Italy). Time-lapse images were taken for up to 10 h, with 1 s exposure time, every 1–5 min using a 20X air objective (Olympus, NA = 0.75) or every 5-10s using a 40X oil immersion objective (Olympus, NA = 1.3). All acquisitions were done with a CCD sensor at 12bit depth (ORCA-D2, Hamamatsu).

Image Analysis Tools

Image analysis was performed using ImageJ software (NIH) and a custom-build MATLAB code (Mathworks). The software consists in three main modules: the first image of the sequence is processed with a user customizable 2d Gaussian filter in order to remove the noise. The user then needs to select a point inside the soma of the cell under investigation. This action identifies the origin of the coordinate system that allows the automatic extraction of the cell body. Subsequently, a phase congruency algorithm is applied in order to detect line features such as neurites: this results in a black and white map where the user selects the position of the neurite hillock and its edge (Kovesi, 2000; Wu et al., 2010). The identification of the soma and neurite geometries allows the user to restrict the area of the possible locations in which the neurite hillock and the neurite edge can be found. In our experiments, the length of the neurite was evaluated as the minimum path necessary to connect the two points passing through the above-threshold pixels, defining the neurite in the map. The AW position was also selected manually by the user and, applying the method above mentioned, the distance covered along the neurite was evaluated. Finally, the algorithm was applied to all the images in the sequence using the same parameter, adjusting the position of the soma and the three points on the neurite (the neurite hillock, its edge and AW position) according to the corresponding map obtained from the phase congruency algorithm. The user supervised the whole operation, correcting the algorithm when necessary.

Morphological Analysis of Actin Waves and Growth Cones

For the morphological analysis of each AW, the area was determined manually at different time-points of the wave progression along the neurite, before and after drug addiction. The mean AW area throughout the neurite was then obtained by averaging the areas previously studied. For the morphological analysis of the GCs, the area was determined manually at different time-points of the wave progression and also every 30 s for about 5–10 min after arrival and merging of the AW with the growth cone. The mean GC areas were then obtained by averaging the areas previously calculated.

Intensity Line Scans

Line scans were performed with ImageJ software. Images were background subtracted and thresholded to select the neurite of interest, and then a line was traced in the neurite to have an intensity profile trace. Traces were then aligned to the half-maximum value of the front of the actin wave (oriented toward the growth cone). Half maximum values were determined by manual identification of the maximum actin signal at the front half of the actin curve. Traces were then computationally aligned using a custom-built MATLAB software.

Myosin Puncta Density Measurements

STED images were background subtracted and thresholded to highlight Myosin puncta. Regions of Interest were traced in the central and peripheral regions of AWs and GCs, in the rear and front halves of the AWs, and in two neurite sections of the same area for each AW (8–12 μm^2) immediately before and after the AWs. The areas were then analyzed through the SynPAnal software (Danielson and Lee, 2014) to detect the puncta density in the areas of interest. In the same regions, the actin mean intensity was calculated using an ImageJ software, and the resulting puncta density measurements were normalized for the highest actin intensity data for each AW and GC that have been considered.

Analysis of the Actin Wave Position, Velocity, and Frequency along the Neurite

All the analyses of the AW position were performed using an ImageJ program and custom-built codes written in MATLAB (Mathworks) (see Image Analysis Tools paragraph). Time-lapse sequences were background corrected and thresholded to select

the neurite of interest. The positions of the soma and of the neurite's end were tracked automatically, whereas the AW position along the neurite was tracked manually. The distances calculated from the soma were then extrapolated and plotted as a function of time. The time-points when no wave was traveling along the neurite were eliminated. The velocity of the AW was calculated by extracting the distance covered and the time taken from the position data previously described, then by dividing distance over time. The frequency of AW was calculated as AW per hour by manually counting all the AW events before and after drug addiction.

Statistical Analysis

All results have been obtained from at least three independent experiments and expressed as the mean ± S.E.M. Experimental data were analyzed with Student's *t*-test or U-Mann Whitney test using a SigmaPlot 10.0 software (Systat Software Inc.). Differences among samples were considered statistically significant when $p < 0.05$.

RESULTS

Due to their highly dynamic behavior, study of the AWs requires live imaging. Hence, we performed long-term live cell imaging of AWs on rat hippocampal cells plated on Matrigel/Laminin at 1–2 days *in vitro* (1–2 DIV) using the actin label mCherry-LifeAct (Riedl et al., 2008; Winans et al., 2016). In this experimental setting, the morphology and dynamics of the AWs were comparable to what had been previously reported (Ruthel and Banker, 1998; Flynn et al., 2009; Katsuno et al., 2015; Winans et al., 2016). Indeed, hippocampal AWs exhibited a growth cone-like morphology and behavior forming filopodia and lamellipodia on one or both sides of the neurite shaft and travel mainly in an anterograde fashion in our 1 and 2 DIV imaging windows (**Figure 1A**; Supplementary Video 1). The analysis of 114 neurites showed that the AWs are generated at a median frequency of 2–3 per hour and move at an average speed of 2–3 μm/min, in agreement with previous reports. Strikingly, no difference in AWs' behavior was observed plating the hippocampal neurons on different substrates such as poly-D-lysine and poly-L-ornithine (**Figure 1**; Supplementary Videos 2, 3).

LifeAct is known to induce bundling of actin filaments (Riedl et al., 2008). Therefore, to rule out any effect of our experimental setup on the dynamics of the AWs, we tested other staining approaches. As an alternative actin label, we used SiR-Actin (Lukinavicius et al., 2014), a membrane-permeable based on the jasplakinolide, a drug that promotes actin polymerization by enhancing the rate of filament nucleation (Bubb et al., 1994). SiR-Actin caused a decrease of the AWs number and of actin motion, presumably due to the residual activity of jasplakinolide (Supplementary Figure 1) that was shown to freeze AWs (Winans et al., 2016). Therefore, we tested the membrane marker Vybrant DiI which is well known to not interfere with actin dynamics. Vybrant DiI enabled the visualization of AWs (Supplementary Video 4), which exhibited velocities (2–3 μm/min) and frequencies (2–3 AW/h) similar to what observed when mCherry-LifeAct is present. Hence, we concluded that LifeAct does not have any effect on the AWs dynamics and can be used in this experimental system.

Actin Waves Do Not Boost Neurite Elongation

The live cell imaging of the rat hippocampal cells showed that as an AW moves toward a distal GC at the tip of a neurite, the GC retracts by about 15–20 μm approaching the incoming AW and merges with it (**Figure 1B**). This pulling effect, already described by Flynn et al. (2009), was observed in almost all neurites both 1 and 2 DIV. The arrival of AWs is associated to a transient retraction of the GC and also to a transient increase of the GC size (Supplementary Figure 2) so that the cyclic behavior is observed. These events, however, do not result in a net neurite elongation (**Figure 1C**). We then analyzed in detail the relation between AWs reaching the neurite tips and neurite outgrowth (**Figure 2A**) and we could not observe any positive correlation between the number of migrating AWs and neurite elongation in a total of 126 neurites emerging from the cell body of hippocampal neurons (**Figure 2A** and Supplementary Figure 3). Our data clearly show that neurites exhibiting either no or a small number of AWs grow much more than neurites with a larger quantity of AWs (**Figures 2A,B**): the former can grow up to 400–450 μm, while the latter <50 μm or do not grow at all. In contrast with what reported in previous papers (Flynn et al., 2009; Winans et al., 2016), no difference was observed between 1 and 2 DIV (**Figure 2A**).

Remarkably, in several developing neurons, we observed a continuous neurite growth with an almost constant elongation speed in the absence of migrating AWs (2–3 μm/min), which slowed down (0.5 μm/min) in the presence of AWs (**Figure 3A**). The kymographs of the neurite tip (white) and AWs (red) in **Figure 3B** show that when AWs started to reach the GC tip its elongation stopped completely. When developing hippocampal DIV1 or DIV2 neurons were stained with Vybrant DiI we could follow for up to 20 h—and even for 1 day—the neurite growth and the appearance and migration of AWs. In the example shown in **Figure 3C**, during the initial 10 h of observation many AWs were seen propagating along the neurite shaft and reaching the tip (red cross) but the neurite (blue cross) did not grow and no significant neurite elongation was observed (**Figure 3C**). In the same experiment, when the frequency of AWs decreased substantially the neurite started to grow and in the following 6 h only two AWs were observed. Finally, AWs appeared again, the neurite growth stopped and a small retraction was observed (**Figure 3C**). Within the same time window (**Figure 3D**) we computed the velocity v of the neurite tip (blue line) and the frequency of migrating AWs (red line) and we found that when the frequency increased, the velocity decreased concomitantly and vice versa, suggesting that there is a negative correlation between neurite advancement and frequency of appearance of AWs. We obtained another five live cell experiments with a duration longer than 6 h and in all these experiments we observed a negative correlation between AWs frequency and neurite elongation. In order to have a more complete picture of the

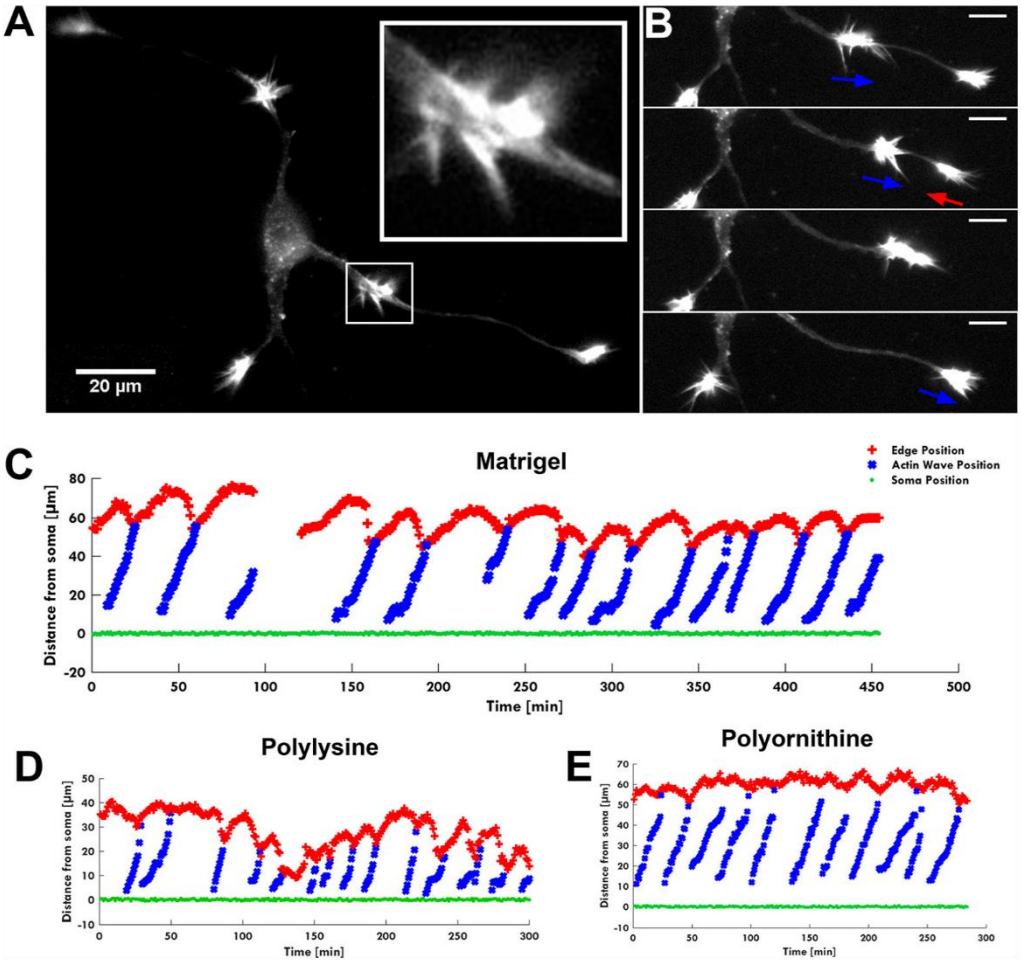

FIGURE 1 | The AW pulling effect on GC. **(A)** Fluorescence image of F-actin showing an actin wave advancing along a neurite with its characteristic growth cone-like shape (white square). The insert shows a higher magnification of the growth cone-like AW. **(B)** Time-lapse images of the neurite shown in **(A)**. When an AW approaches the distal neurite, the GC retracts several microns to reach the wave, then merges with it and advances following the wave arrival. Blue arrows indicate AW direction; red arrows indicate GC retraction. Scale bar refers to **(A,B)** = 20 µm. **(C–E)** Plots showing the progression of several AWs (blue) shown in **(A,B)** and Supplementary Video 1 from the soma (green) along the neurite. The origin of the axes is set to the initial soma position. The edge of the neurite (red) shows the retraction/growth cycles of the GC upon arrival of the AW. The mean velocity of AWs is 2.2 ± 0.4 µm/min. For these experiments, the hippocampal neurons were plated on different substrates: Matrigel/Laminin **(C)**, poly-D-lysine **(D)** and poly-L-ornithine **(E)**.

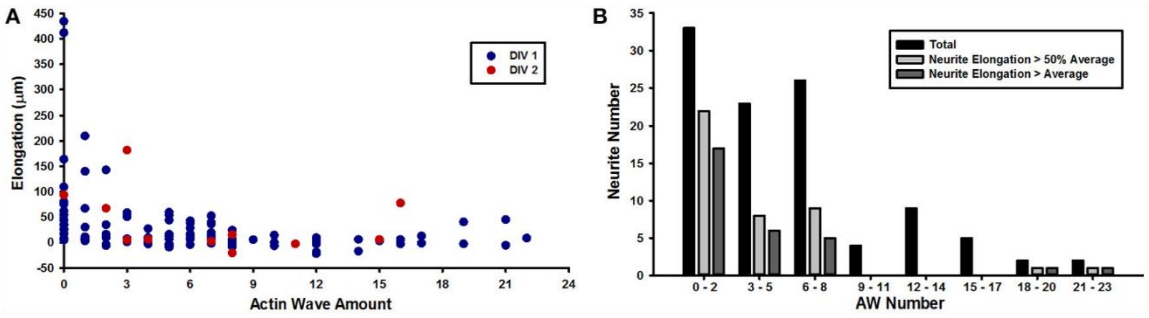

FIGURE 2 | AWs inhibit neurite elongation**. (A)** Graph showing the elongation of the neurites (y axis) per number of actin waves (x axis) imaged at 1–5 min intervals for 8 h. Red dots refer to DIV2 hippocampal culture; blue dots refer to DIV1 hippocampal culture. n =126 neurites **(B)** Quantification of the number of neurites (y axis) per number of actin waves (x axis). n =126 neurites. Black bars refer to all DIV1-DIV2 neurites that present 0–2, 3–5, 6–8, 9–11, 12–14, 15–17, 18–20, or 21–23 AWs; light gray bars refer to neurites that elongate more than 50% of the average length; dark gray bars refer to neurites that elongate up to the average length.

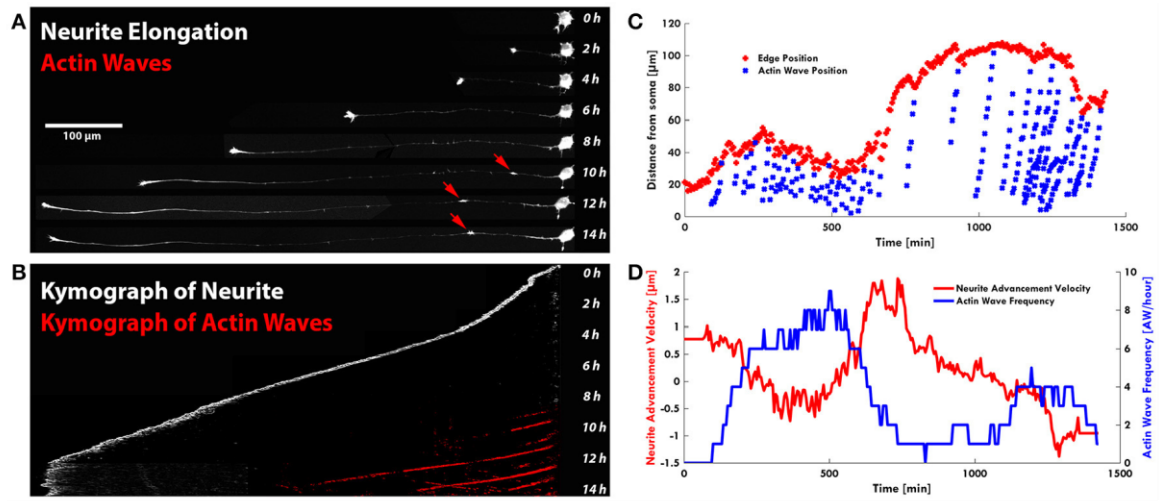

FIGURE 3 | AWs are not associated to neurite outgrowth. **(A)** Timelapse images of the neurite shown in Supplementary Video 5: the neurite grows up to 450 µm in the presence of a few AWs (red arrows) (one of the two points in **Figure 2A** with no AWs). Scale bar = 100 µm **(B)** Kymograph generated from the time lapse images of the F-actin expressing neurite shown in **(A)**. **(C)** Plot highlighting the progression of the AWs (light blue cruises) along the neurite shown in Supplementary Figure 4. The edge trace (red cruises) highlights that neurite outgrowth occurs with a few AWs, while in the presence of high frequency of AWs, in red, the neurite does not grow. **(D)** Graph highlighting in red the advancement velocity (µm/min) of the neurite shown in **(C)** and in blue the AWs frequency in function of time.

AWs' role, we computed the GC area (color scale line) and the AW distance from the soma (blue line) from the experiment reported in **Figure 1**. Interestingly, the GC lost between 30 and 70% of its original area in 30–60 min after fusion with the wave, in the absence of any significant elongation (**Figure 4A**). When we computed the mean area of the GC before and in the 5–10 min after the AW arrival, we observed a two-fold increase in the GC area (Supplementary Figure 2), confirming previous findings on GC size and dynamicity change after the AW arrival (Flynn et al., 2009). These results indicate that AWs have a paramount role in maintaining highly motile the GC which can explore the surrounding environment (**Figure 4B**).

Myosin IIB Is Required for AW Formation and Structure

Next, we investigated the importance of Myosin IIB in the structure and dynamics of the AWs, and their similarities and differences with the GC ultrastructural organization. In GCs, Myosin IIB is localized mainly in the T zone, in the C domain and in the contractile node region (Rochlin et al., 1995; Loudon et al., 2006; Burnette et al., 2008). Since Myosin IIB is required for maintaining GC shape, polarization, size, actin organization, and for normal rates of shape change and traction force (Bridgman et al., 2001), we speculated that it could play a role also in AWs framework, beside the pulling effect observed herein. Recent works have highlighted that AWs generate traction forces that help their anterograde movement (Katsuno et al., 2015) suggesting the importance of Myosin II in the AW dynamics (Flynn et al., 2009). However, none of them have studied the distribution of Myosin IIB in propagating AWs in detail. To address this point, we employed two-color STimulated Emission Depletion (STED) nanoscopy (Göttfert et al., 2013) to verify whether and where Myosin IIB is present in AWs (**Figure 4** and Supplementary Figure 5) with a sub-diffraction resolution. The utilization of a super-resolution technique allowed us to explore in greater detail Myosin IIB localization not only in the neurite shaft and in the propagating AWs, but also in the GC with respect to actin and β-III tubulin. This latter cytoskeletal component was acquired in confocal mode. STED images showed that Myosin IIB appeared as spots localized mostly at the sides of the β-III Tubulin (**Figures 5A,B**) with a net border between the central and the peripheral region of the AW (**Figures 5D,E** and Supplementary Figures 6A–C). The averaged line scan analysis of 16 neurites (**Figure 5C**) highlighted an increase in β-III Tubulin fluorescence intensity in and behind the AW that reflects an increased number of microtubules (MTs), in accordance with previous observations (Winans et al., 2016). Myosin IIB is present in the AW, with a peak at about 10 µm from the wave front that precedes by 5 µm the peak of actin, indicating a possible clustering of Myosin IIB at the rear of the advancing AWs. The quantification of the Myosin IIB puncta density revealed a significant concentration in the central region of the AWs, with a mean density of 7.3 ± 1.6 puncta/µm^2 and a preferential localization in the rear part of the wave (8.2 ± 2.0 puncta/µm^2; **Figures 5F,G**). This tendency was present in 60% of the analyzed AWs, whereas in 20% of cases the distribution appeared stable and in another 20% a slight increase toward the AW front was observed (**Figure 5H**). A comparison of the Myosin IIB puncta density between the regions immediately before and after the traveling AW revealed an aggregation behind the wave (5.8 ± 1.0 puncta/µm^2 behind vs. 3.4 ± 0.8 puncta/µm^2 in front) (**Figures 5I,J**).

STED nanoscopy also allowed us to characterize the structural differences between AWs and GCs. Myosin IIB appeared as spots localized in the transition and central regions of the GC, in correspondence of dense, actin filaments (**Figures 6A,B**), where it showed an arc-like organization (Supplementary Figures 6D,E).

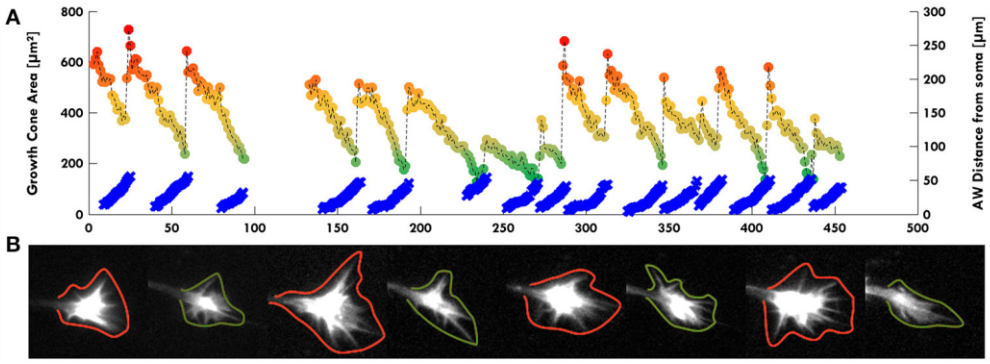

FIGURE 4 | AWs increase GC volume. **(A)** Graph highlighting in color scale (from red to green dots) the change of the GC Area (μm^2 on left scale) and in light blue the AW distance from the cell soma (μm on right scale) in function of time (minutes). The GC size is maximum (red dots) when the AW arrives to the tip of the neurite and merges with the GC itself. The GC minimum size (green dots) is reached immediately before the arrival of the AW when the GC is pulled backwards, and the AW is close to the GC without merging. The dark yellow dots indicate the intermediate states from the maximum GC size (red dots) to the minimum one (green dots). All the points corresponding to the GC size are connected with a dashed line. **(B)** Examples of some timelapse images used in **(A)**. GCs with green contours refer to green dots in **(A)**; GCs with red contours refer to red dots in **(A)**. We observed that AWs induce an increase of the GC volume with filopodia sprouting (see also Supplementary Figure 2) and this suggests a major role for AWs in regulating GC sensing the surrounding environment.

Indeed, the density of the Myosin IIB spots in the central and transition regions of the GC was significantly higher (10.5 ± 1.3 puncta/μm^2) than in the peripheral zone (0.9 ± 0.2 puncta/μm^2), and no significant difference in the Myosin IIB concentration between the GC and the AW was found (**Figures 6C–E**). The analysis of linear profiles along different sections of AWs and GCs showed that in the central regions Myosin IIB puncta are isolated or cluster together along actin-rich structures, whereas in the peripheral regions isolated spots of Myosin IIB are present along thicker actin filaments. However, the arc-like, anti-parallel structure of Myosin IIB molecules and actin filaments present in the transition zone of the GC is completely lost in the AWs (Supplementary Figure 7), where the transition is sharper and flattened along the neurite shaft. Taken together, these findings indicate that, despite being similar in many aspects, the acto-myosin organization of AWs and GCs retains some crucial differences that reflect on the distinct dynamics of the two structures.

Myosin IIB Inhibition Abolishes GC "Pulling" Effect

After having assessed the presence of Myosin IIB in both AWs and GCs, we investigated the mechanisms regulating the pulling effect of the approaching AW on the GC, since this appears to be a basic feature of their dynamics. We speculated that the pulling effect could originate from a retrograde shift of actin likely caused by the interplay between the acto-myosin complex and the membrane of the neurite itself. To this aim, we treated hippocampal cultures with blebbistatin, which inhibits the ATP activity of the Myosin A and of B isoforms (Kovács et al., 2004). Treatment with 20 μM blebbistatin abolishes the growth cone-like shape of the AWs (**Figure 7A** and Supplementary Video 6) suggesting a rearrangement of the actin assembly after Myosin inhibition (**Figure 7Bi**). Indeed, the AWs became longer and thinner, but the area of AWs after blebbistatin addition remains almost unchanged, even if the lamellipodia structures disappear (**Figures 7C,E**). In contrast, the GC of all treated neurites becomes a pointed bundle of actin (**Figure 7Bii**), loses all lamellipodia, and its area shrinks by more than 60% (**Figures 7B,F**). This result suggests a higher impact of Myosin II inhibition on the structure of the GC than that of the traveling AW. Following blebbistatin treatment, the tip of the neurite exhibits a significant outgrowth and the progressive disappearance of the pulling effect when the AW approaches the tip of the neurite. This could be the effect of the inability of the GC to move (**Figure 7D**). We then determined the frequency of the AWs calculating the number of complete waves (i.e., waves able to reach the tip of the growth cone) in an hour. Blebbistatin increased the frequency of AW appearance and, at the same time, reduced AWs velocity, calculated as the time taken by the wave to reach the tip of the growth cone, normalized for the length of the neurite (Flynn et al., 2009; Katsuno et al., 2015; Tilve et al., 2015) (Supplementary Figure 8). Overall, these data show a strong involvement of Myosin II in both structural and dynamical organization of AWs, and highlight a dissimilarity in the role of Myosin in AWs and in the GC itself. In both GCs and AWs Myosin seems to be responsible for the maintenance of lamellipodia.

While in the GC myosin inhibition causes a rapid neurite outgrowth, the AWs traveling speed is reduced and the waves loses their GC-like shape. Since Myosin is important for the retrograde actin flow in both structures—as found in the recent work by Katsuno et al. (Katsuno et al., 2015)—we can assume that the simultaneous disruption of shape and retrograde flow in both structures upon blebbistatin inhibition makes impossible to exert the forces needed to mediate the "pulling" effect and finely regulates the neurite outgrowth.

Cholesterol Depletion Impacts AW Formation and Morphology

As inhibition of Myosin II alters the shape of AW, the surface tension of the membrane surrounding the wave could have a

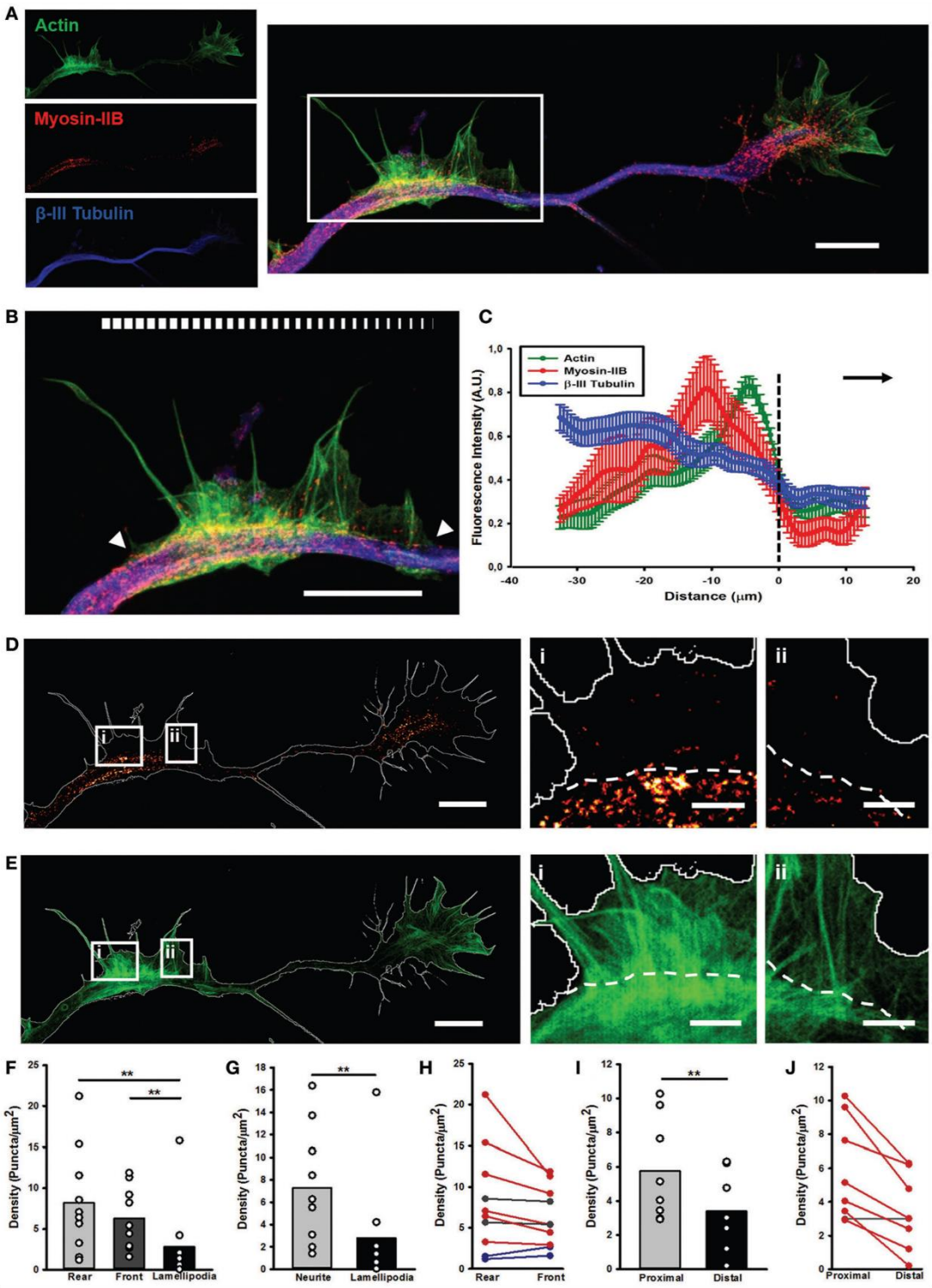

FIGURE 5 | STED microscopy reveals Myosin IIB in AWs. **(A)** STED image of a rat hippocampal neuron at 1 DIV stained with actin (phalloidin, green), non-muscle myosin IIB (red) and β-III tubulin (blue) shows the presence of myosin IIB in the GC and AW. The white box highlights the AW. The insets on the left are the single channel images. Scalebar: 5 μm **(B)** Magnification of the AW [white box in **(A)**] highlighting that myosin IIB is brightest in the rear region of the AW. The white arrowheads indicate the beginning and the end of the AW, and the white bar mimics the myosin intensity. Scalebar = 5 μm **(C)** Averaged line scans (see Methods) show that myosin IIB is highly concentrated at the rear of advancing actin wave. Dashed line indicates AW front, and black arrow highlights wave direction. $N = 9$ neurites. Measurements are performed on STED images. All traces were normalized by mean intensity and smoothed before averaging (Winans et al., 2016). Data shown as Mean ± SEM. **(D,E)** STED images of the myosin IIB **(D)** and actin **(E)** channels showing that the myosin brightest puncta concentrate in the GC and in and

(Continued)

FIGURE 5 | behind the AW. The panels on the right show two magnifications of sections from the back (i) and front (ii) regions of the AW, with a clear border between the neurite and the emerging peripheral lamellipodia, highlighted by the white dashed lines. Scalebars in **(D,E)** = 5 μm. Scalebars in (i, ii) = 1 μm. **(F)** Histogram showing a significant increase in the density of myosin IIB puncta in the rear and front central regions of the AW with respect to the peripheral lamellipodia structures. (n = 10 AWs). **(G)** Histogram showing that the density of the myosin IIB puncta is significantly higher in the central region of the AW than the periphery. (n = 10 AWs). **(H)** Plot showing the changes in the density of myosin IIB puncta between the Rear and Front sections of the AW. **(I)** Histogram showing that the density of the myosin IIB puncta is significantly higher in the region immediately behind the AW (Proximal) than the region immediately after it (Distal). (n = 10 AWs). Student's test was performed for histograms: $^{**}P \leq 0.01$. **(J)** Plot showing the changes in the density of myosin IIB puncta between the region immediately behind and after the AW. Increase in density in **(H,J)** is depicted in blue, decrease in red and stable (change < 12%) tendency is depicted in gray. A conceptual scheme for ROIs used for analysis is found in Supplementary Figure 5.

role in its dynamics. A high cholesterol concentration increases the membrane tension and its reduction has been demonstrated to reduce the stiffness of the cellular membrane enveloping the actin filament network (Amin et al., 2012). To test the effect of the cholesterol depletion on the AWs dynamic, we treated the hippocampal neurons with the β-cyclodextrin that has been reported to be the most efficient compound in extracting cholesterol from membranes (Vladislav et al., 2013). Live-cell imaging showed a loss of the growth cone-like shape of the AW after addiction of β-cyclodextrin (**Figures 8A,B**), a reduction of the AW's pulling effect (**Figure 8C**), and a severe loss of the AWs' area (**Figure 8F**). Treatment with β-cyclodextrin reduced both velocity and frequency of AWs by about 10 and 50% respectively (**Figures 8D,E**). No visible effect was observed on the GC after treatment with β-cyclodextrin. Taken as a whole, our data suggest that the membrane is involved not only in AW shape maintenance, but also in AW dynamics.

RhoGTPases Regulate AW Architecture and Dynamics

RhoGTPases modulate actin nucleation and play a key role in the regulation of GC morphology and dynamics (Dickson, 2001). They are known to act downstream of a plethora of signaling molecules and guidance cues, and to influence the activity of actin and actin-binding molecules (Hall and Nobes, 2000; Lowery and Van Vactor, 2009; Toriyama et al., 2013). Hence, we wondered whether they have a similar role also in AWs.

Since Rac1 and Cdc42 are known to play a part in anterograde propagation of an AW (Winans et al., 2016), we started our study by assessing the function of these NPFs. Cdc42 and Rac1 can be inhibited by the selective guanine nucleotide binders ML141 and EHT1864, respectively, providing a reversible and non-competitive inhibition (Shutes et al., 2007; Surviladze et al., 2010). Cdc42 inhibition (ML141, 10 μM) altered the GC shape (**Figures 9A,B**), decreased AWs velocity (−25%), size (−40%), and frequency 60 min after drug addition (−75%) (**Figures 9C–E**). These effects are concentration-dependent, since ML141 at 30 μM abolishes the wave phenomena without a significant change in the GC dynamics (Supplementary Figure 9).

Similarly to the Cdc42 inhibition, the addition of Rac1 inhibition by EHT1864 at 10 μM concentration caused a complete loss of the growth cone-like shape (**Figures 9F,G**) and a significant reduction of the AW Area (**Figure 9J**). Moreover, a reduction of 75% in AWs frequency (**Figure 8H**) together with a 50% decrease in the AWs velocity (**Figure 9I**) assessed an important role for Rac1 in positively modulating the actin polymerization required for the AWs generation. These findings highlight the role of Rac1 in wave inception and are consistent with previous data, where its activation was sufficient to trigger AW initiation and protrusion (Winans et al., 2016).

Taken together, these data support the hypothesis that Cdc42 and Rac1 have an important role in the AW architecture and dynamics, and suggest a strongest role of Cdc42 in AW inception and of Rac1 in AW traveling, hence pointing at the presence of different actin-regulating mechanisms involved in different steps of the AW biology.

DISCUSSION

The function and role of AWs in neuronal development is still unclear. In the present work, we show that migrating AWs do not boost neurite outgrowth and we suggest an alternative role for it. While the GC size is reduced in the absence of AWs, the arrival of AWs solely restores the original GC extension allowing it to properly explore the environment (**Figure 4**). We also demonstrate that even if AWs resemble the GC in size and appearance, there are important differences in the acto-myosin complex that in the AWs is more involved in shape maintenance, while in the GC it controls both structure and dynamic. In conclusion, we provide clear evidence for the involvement of both membrane and small GTPases in the regulation of the speed and shape of migrating AWs. Let us now discuss in detail the possible functions of AWs and the underlying molecular mechanisms.

Functions of AWs

The AWs have been originally described in 1998 by Ruthel and Banker as wave-like membrane protrusions containing actin filaments along the axons and immature neurites of cultured rat hippocampal neurons. These authors also highlighted a key role for the AWs in transporting actin and associated proteins to the GC at the tip of an extending axon (Ruthel and Banker, 1998). Following their work, different groups have then found a dual role for AWs in neurite outgrowth *in vivo*: they are the drivers in neurite extension and, at the same time, they play an important role in a stochastic search mechanism that allows a set of neurites to explore the surrounding space to sense the polarized growth cues provided by the developing brain (Flynn et al., 2009; Katsuno et al., 2015; Winans et al., 2016). AWs investigated herein are generated at a frequency of 2–3 waves per hour, propagate with an average speed of ∼2–3 μm/min and travel from the base of the neurites to the GC. Our long-term

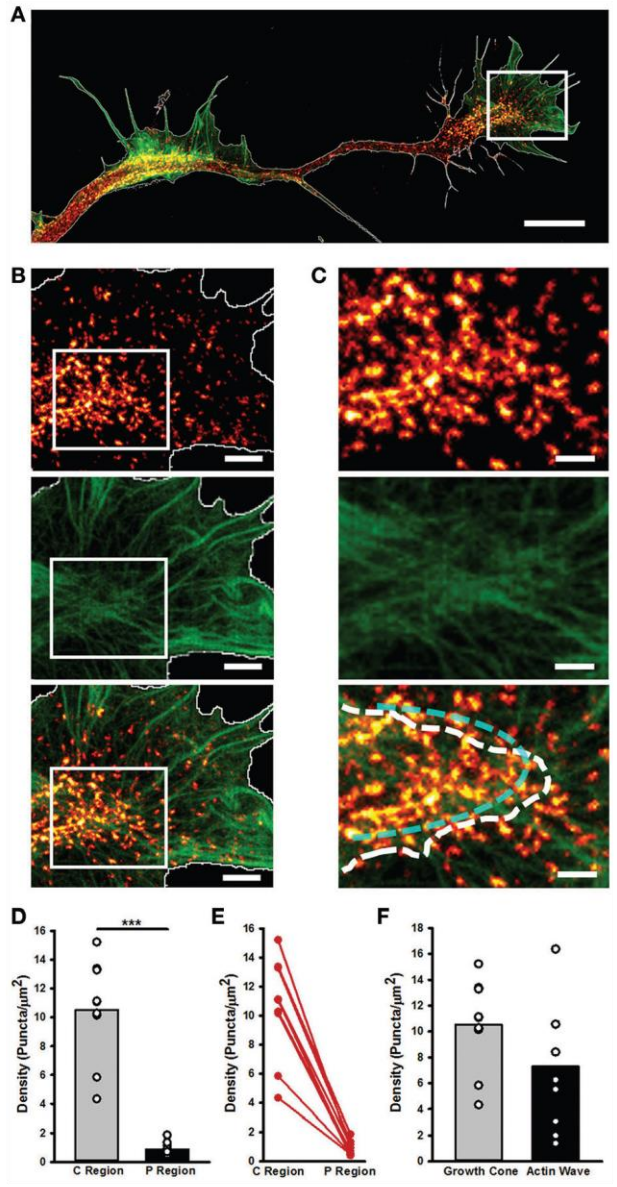

FIGURE 6 | STED microscopy highlights GC and AW similarities and differences in myosin IIB localization. **(A)** Merged Image showing the Myosin IIB and actin channels of the neurite in **Figure 4**. The edge is highlighted in white. Scale bar = 5 μm. **(B)** Magnifications of the region delimited by the white box in **(A)** showing the actin (top panel), Myosin IIB (middle panel) and both (bottom panel) channels. Scale bar = 1 μm. **(C)** Magnifications of the area delimited by the white boxes in **(B)** of the border between the central and peripheral regions of the GC. The white dashed line defines the border between the central and peripheral regions of the GC, while the cyan dashed line highlights the acto-myosin contractile arcs of the transition zone. Scale bar = 500 nm. **(D)** Histogram showing that the density of the Myosin IIB puncta is significantly higher in the central and transition zones than in the peripheral region. (n = 9 GCs). **(E)** Plot showing the constant decrease (depicted in red) in the density of Myosin IIB puncta between the Central and Peripheral regions of the GC. **(F)** Histogram showing the density of Myosin IIB puncta in the GC with respect to the correspondent AWs. (n = 9 neurites). Student's test was performed for histograms: ***$P < 0.001$.

live cell imaging experiments clearly show that the continuous arrival of AWs generates retraction/growth cycles that, although causing a transient increase of the GC size, do not result in a net neurite elongation (**Figures 1–3**). A possible explanation for the discrepancy between our results and what previously reported could be related to the use of P1–P2 hippocampal neurons in our experiments, whereas previous studies used embryonic mouse (E16–E17) or rat (E18) (Flynn et al., 2009; Katsuno et al., 2015; Winans et al., 2016; Tomba et al., 2017). Indeed, although neurogenesis continues postnatally, many more neurons are born at the earlier stages and the "older" neurons might exhibit a different behavior. It is also worth pointing out that our manuscript is the first one to give a complete picture of the long-term behavior of the AWs that, despite not promoting neurite outgrowth, seem to mostly contribute to the stochastic "tug of war"-like growth and retraction that leads to neuron polarization, as already suggested in other papers (Flynn et al., 2009; Winans et al., 2016; Inagaki and Katsuno, 2017). Another possible role of the AWs is suggested by the experiments similar to those shown in **Figure 1** and summarized in **Figure 4**: during the exploration of the environment, GCs become smaller and following the arrival of an AW, GCs recover their original area suggesting that AWs have certainly the role and function of providing fresh actin oligomers and other metabolic products which were lost during the exploration of the environment. Therefore, we propose that AWs have a major role in maintaining the GC lively and active, so that filopodia can remain sufficiently long to explore the environment and lamellipodia can maintain their structure and architecture (**Figure 4B**).

Morphology and Architecture of AWs and GCs: Similarities and Differences

AWs resemble the GC in size and appearance: both structures bear filopodia and lamellipodia (Ruthel and Banker, 1998; Lowery and Van Vactor, 2009) and are enriched with actin and actin-associated proteins (Ruthel and Banker, 1998; Flynn et al., 2009; Toriyama et al., 2013; Kubo et al., 2015) that modulate their structure and movement. Actin and molecules that modulate its dynamics are present in both structures, and contribute to the balance between treadmilling and retrograde flow that produces the traction force on the substrate (Toriyama et al., 2013; Katsuno et al., 2015; Inagaki and Katsuno, 2017). STED nanoscopy revealed the AWs structure with a sub-diffraction resolution: similarly to what observed in the GC, in the AWs F-actin is present in filopodia (bundled F-actin) and lamellipodia (F-actin meshwork). The distribution of Myosin IIB puncta appear to be also similar: it accumulates in the central regions of both GC and AWs, especially in the regions where actin filaments are more densely condensed (**Figure 5**). However, the acto-myosin contractile arcs, that in the GC support the retrograde flow and divide the microtubule-rich central domain from the peripheral region, are substituted in the AW with linear, dense acto-myosin structures organized in a rear-to-front gradient, that separate the main core of the AW from the erupting peripheral elements (Supplementary Figures 6, 7). This difference can be explained with the diverse motion patterns of GCs and AWs: while the former needs to expand and retract to better explore the surrounding environment for neurite elongation (Dent et al., 2011; Coles and Bradke, 2015), the latter travels along the neurite shaft and needs stable, bilateral structures that

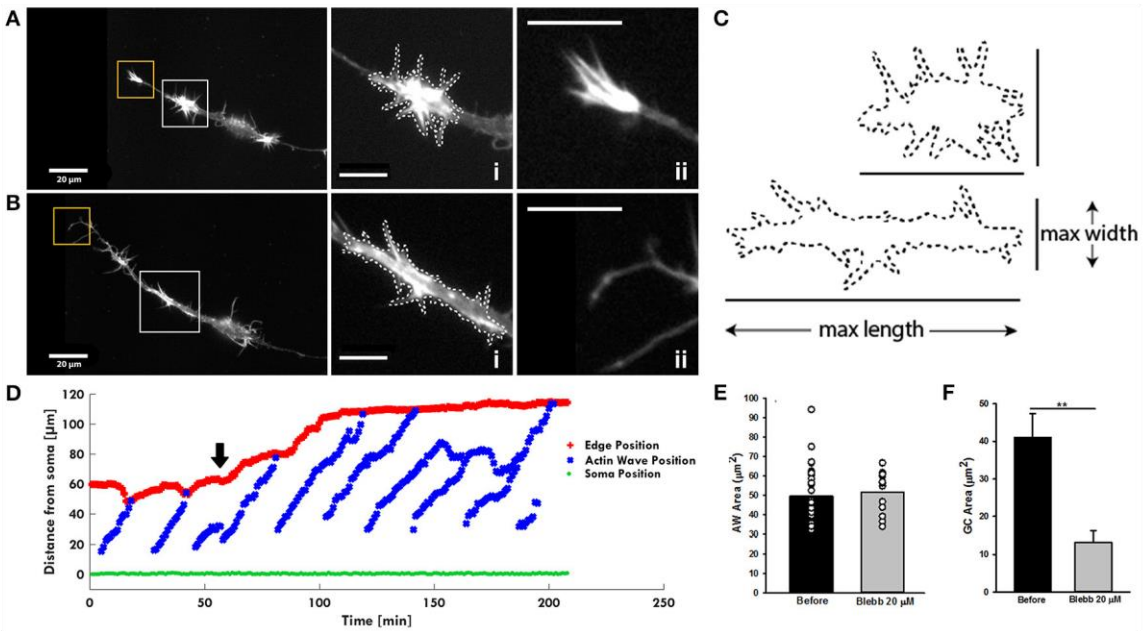

FIGURE 7 | Blebbistatin treatment differently impacts AWs and GCs. **(A,B)** Live-cell images of an AW before **(A)** and after **(B)** Blebbistatin treatment (20 μM) (Supplementary Video 6). Images were collected every 10 seconds. Insets on the right represent a magnified view of the AWs (i) and GC (ii) showed in **(A,B)**. Blebbistatin treatment changes the morphology of the wave that loses the characteristic growth cone shape and abolishes the GC completely. White dashed lines indicate the AWs' shape before **(A)** and after **(B)** the treatment with Blebbistatin. Scale bar in **(A,B)** = 20 μm. **(C)** Comparison of the AWs shape before **(A)** and after **(B)** Blebbistatin treatment. **(D)** Plot highlighting the progression of the AWs (blue) shown in **(A,B)** and Supplementary Video 6 from the soma (green) along the neurite. The origin of the axes is set to the initial soma position. The black arrowhead indicates blebbistatin addition: Myosin II inhibition progressively abolishes the pulling effect. The edge trace (red) highlights the disappearance of the GC retraction upon the AW arrival after blebbistatin treatment. **(E)** Quantification of the AWs mean area (μm^2) calculated on neurons treated with or without blebbistatin for 4 h and imaged as in **(A,B)**. $N = 18$ AWs. **(F)** Quantification of the GC mean area (μm^2) calculated on neurons treated with or without blebbistatin for 4 h and imaged as in **(A,B)**. $N = 6$ GC. Student's and U-Man Whitney tests were performed for all histograms: $^{**}P < 0.01$.

can propel it forward modulating the acto-myosin dynamics and the forces exerted to the substrate, in concert with upstream signaling molecules (Toriyama et al., 2013; Katsuno et al., 2015). Furthermore, in agreement with previous findings, our results indicate that Myosin IIB has a role that goes far beyond the architecture maintenance: indeed, as an AW approaches the distal neurite, the GC retracts by several microns so to merge with the incoming AW and then advances again (**Figure 1**). After treatment with blebbistatin, the retrograde motion of the GCs was abolished together with a significant neurite outgrowth (**Figure 7D**) confirming quantitative measurements done by Flynn et al. (2009). These findings strongly suggest that Myosin IIB activity normally regulates the rate of retrograde flow that pulls the neurite backwards (Katsuno et al., 2015): its absence triggers a strong increase in actin-bundle length. This observation is in agreement with the blebbistatin experiments performed by Flynn and co-workers, who found a decrease in the GC retraction upon low concentration of blebbistatin treatment (Flynn et al., 2009), and supports the view that the "push" of actin assembly and the "pull" of myosin, that disrupts the actin filaments at their rear, combine to guide the retrograde flow (Medeiros et al., 2006). In recent studies, such acto-myosin structural and dynamic interaction was sufficient to induce contractile t-waves in *in vitro* models (Reymann et al., 2012). If the shape and morphology of AWs and of GCs are similar, these two structures present a very different drug response: blebbistatin treatment leads to a substantial collapse of the GC but not of the AW (**Figures 7A,B**). This difference in sensitivity can be rationalized by taking into account a redistribution of the actin filaments packed into the wave which continues traveling along the microtubules-rich neurite shaft, driven by the constant treadmilling of actin filaments that, in concert with adhesion proteins like shootin-1, might be capable of exerting traction forces to drive AWs forward (Katsuno et al., 2015). On the other hand, the GC structure is finely regulated by acto-Myosin arcs in the transition zone that, besides regulating the retrograde flow (Van Goor et al., 2012), keep the microtubules packed in the central region. The prominent role of Myosin IIB in regulating these dynamics affects the GC architecture.

Mechanisms of AWs Migration: Membrane and Membrane-Bound Regulatory Proteins

Actin is known to be associated with membranes and there have been a number of theoretical studies that focus on the connection between the protrusive forces generated by actin polymerization and the dynamics of the membrane-bound activators. Indeed, F-actin network assembly, organization and dynamics are controlled by the spatial and temporal regulation of the activity of actin-binding proteins that are associated

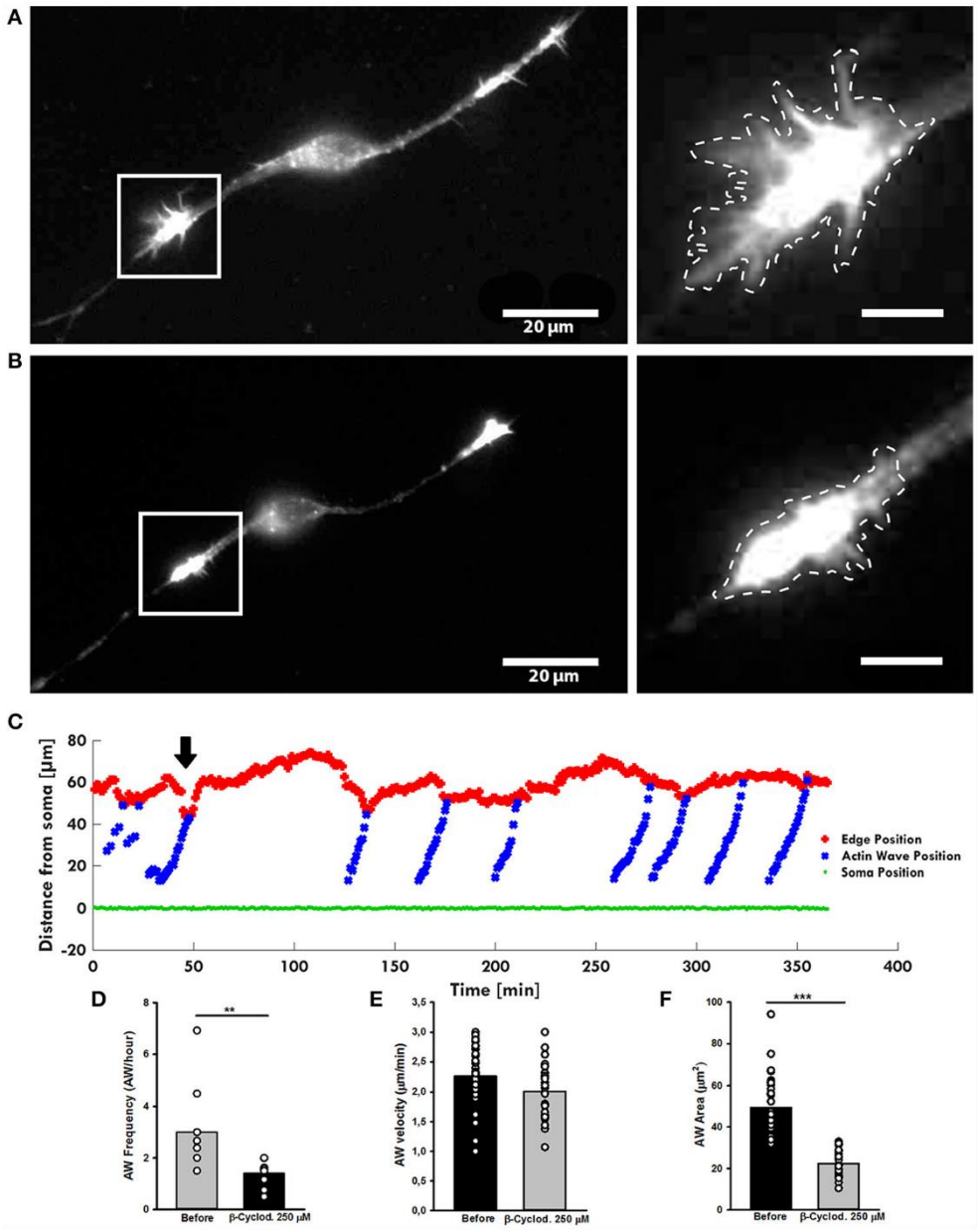

FIGURE 8 | β-cyclodextrin treatment affects AWs structure. **(A,B)** Live-cell images of an AW before **(A)** and after **(B)** β-cyclodextrin treatment (250 µM). On the right, magnified views of the AWs showed in **(A,B)** before and after β-cyclodextrin treatment that abolishes completely the growth cone-like shape. Images were collected every 10 s. Dashed lines indicate the AW's shape before **(A)** and after **(B)** the β-cyclodextrin treatment. Scale bar in **(A)** = 20 µm. Scale bar in **(B)** = 5 µm **(C).** Plot highlighting the progression of the AWs (blue) showed in **(A,B)** from the soma (green) along the neurite. The origin of the axes is set at the initial soma position. The black arrowhead indicates β-cyclodextrin addition: cholesterol depletion decreases the neurite retraction. The edge trace (red) highlights the slight reduction of the GC retraction upon AW arrival after β-cyclodextrin treatment **(D)** Quantification of the AWs frequency calculated on neurons before and after β-cyclodextrin treatment for 4 h and imaged as in **(A,B)**. $N = 9$ neurites. **(E)** Quantification of the AWs velocity (µm/min) calculated on neurons treated with or without β-cyclodextrin for 4 h and imaged as in **(A,B)**. $N = 16$ AWs. **(F)** Quantification of the AWs mean area (μm^2) calculated on neurons treated with or without β-cyclodextrin for 4 h and imaged as in **(A,B)**. $N = 16$ AWs. Student's and U-Man Whitney tests were performed for histograms: $^{**}P < 0.01$; $^{***}P < 0.001$.

with the membrane in a multifaceted way (Bezanilla et al., 2015). To explore the influence of the membrane on the AWs' dynamic, we treated our DIV2 hippocampal cells with β-cyclodextrin, responsible for the depletion of cholesterol from the membrane (Amin et al., 2012). In line with the role of the membrane in the AWs' structure, the elimination of cholesterol decreases AWs' area and causes a loss of the growth cone shape. Interestingly, β-cyclodextrin affects not only the morphology, but also the dynamics of wave phenomena: both frequency and velocity of AWs decreased after β-cyclodextrin addition,

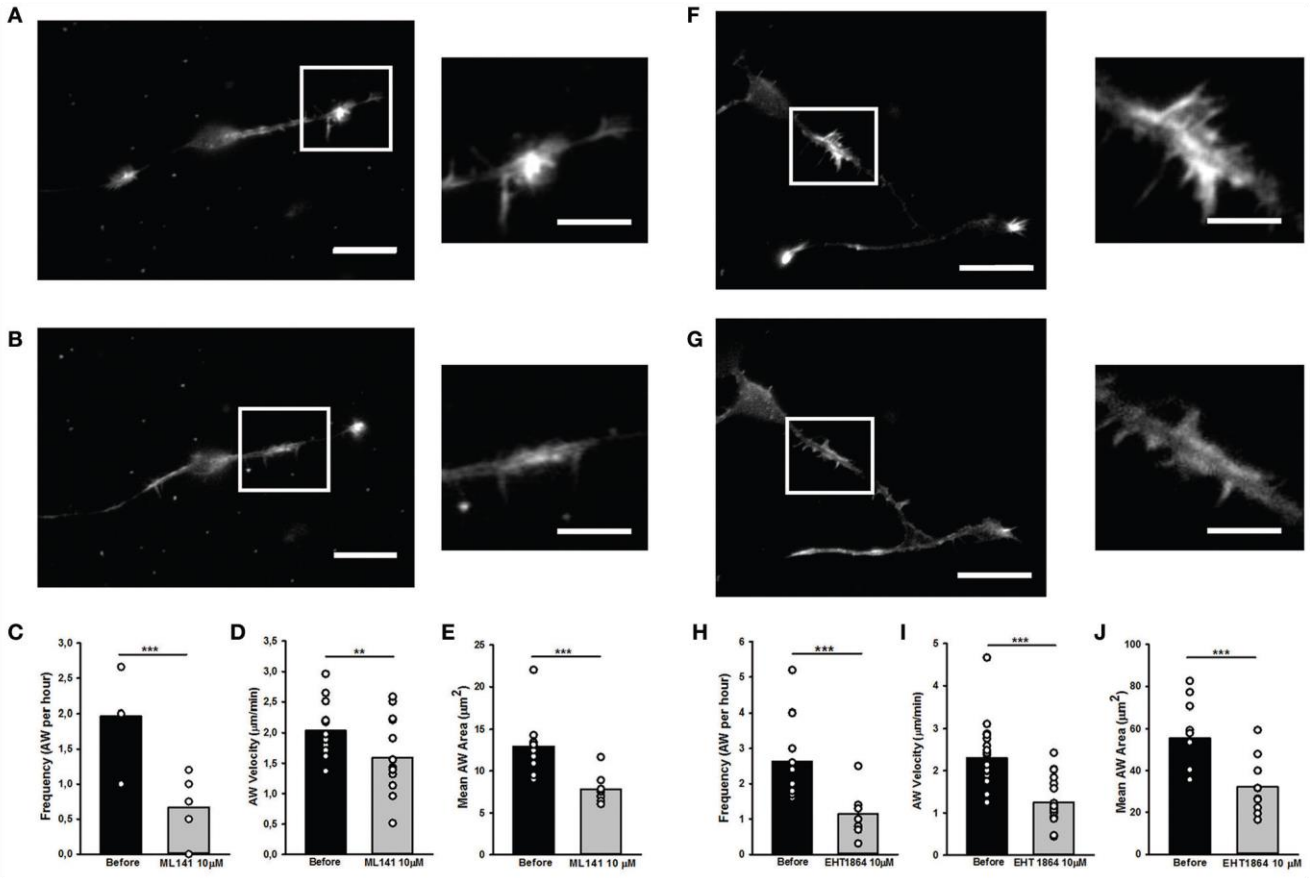

FIGURE 9 | Rho GTPases inhibition affects AW morphology and dynamics **(A,B,F,G)** Live cell imaging of DIV2 rat hippocampal neurons before **(A)** and after **(B)** addition of ML141 (10 μM) and before **(F)** and after **(G)** addition of EHT1864 (10 μM). White boxes indicate the growth cone-like AW. On the right, magnified views of the AW shown in **(A,F)** and **(B,G)** before and after drugs treatment. Scale bar in **(A,B)** = 20 μm. Scale bar in **(F,G)** = 10 μm. **(C,H)** Quantification of the AWs frequency calculated on neurons treated with or without ML141 **(C)** and with or without EHT1864 **(H)** for 4 h and imaged like in **(A,F)** and **(B,G)**. ($n = 10$ neurites). **(D,I)** Quantification of the AWs velocity (μm/min) calculated on neurons treated with or without ML141 **(D)** and with or without EHT1864 **(I)** for 4 h and imaged like in **(A,F)** and **(B,G)**. ($n = 10$ AWs for ML141 and $n = 10$ AWs for EHT1864). **(E,J)** Quantification of the AWs mean area (μm^2) calculated on neurons treated with or without ML141 **(E)** and with or without EHT1864 **(J)** and imaged like in **(A,F)** and **(B,G)**. ($n = 9$AWs for ML141 and $n = 10$AWs for EHT1864). Student's test was performed for all histograms: $^{**}P < 0.01$;$^{***}P < 0.001$.

suggesting a role for the membrane that goes beyond AW shape maintenance. Our data suggest that the membrane may be important for the correct localization of actin filaments and actin-associated proteins in the propagation of AWs, and any perturbation that affects the dynamics of the signaling pathways involved in F-Actin polymerization/depolymerization. The same morphological effect was observed when selective inhibitors of the RhoGTPases Rac1 and Cdc42 were added to the cellular medium. Indeed, the Rho-family GTPases represent a key node for connecting extracellular signals to regulated actin dynamics and, by stimulating actin dynamics, they induce plasma membrane protrusion such as lamellipodia and filopodia (Hall and Nobes, 2000; Burridge and Wennerberg, 2004). Recently, Winans and co-authors demonstrated that Cdc42 exhibit a higher activity in front of an AW, whereas Rac1 activity increases more broadly in the whole AW, and that its activation is sufficient to initiate AWs eruption and propagation (Winans et al., 2016). Indeed, we found that the frequency and the velocity of the AWs, used as parameters of neurite dynamics, decreased in the presence of both the RhoGTPases inhibitors. This significant decrease in AWs initiation capacity and propagation kinetics can be explained with a putative role of these two RhoGTPases in the regulation of both actin polymerization and assembly through the Arp2/3 complex or formins and adhesions strength through an increase in shootin-1 phosphorylation that has been shown to mediate the linkage between F-actin retrograde flow and cell adhesion in GCs (Kubo et al., 2015). A cascade downstream of Cdc42, Rac, and subsequently PAK1 can be considered responsible for the modulation of the balance between adhesion strength and Myosin mediated retrograde flow in maintaining anterograde stable unidirectional motion. Moreover, we observed that Cdc42 inhibition induces a burst in the neurite outgrowth suggesting that it could contribute to the acto-myosin contractility required for modulation of the neurite outgrowth (Wilkinson et al., 2005). Taken together, these results seem to indicate that Cdc42 and

Rac1 could promote AWs migration toward the leading edge and could be involved in the assembly and disassembly of F-actin network also in the AWs. However, the precise spatio-temporal modulation of these RhoGTPases, and of RhoA, that can be an important player for its myosin modulation dynamics, is still unclear, and further experiments to correlate the reciprocal dynamics of these players are needed to fully understand their interactions in the modulation of AWs' inception and movement.

In conclusion, in our study we have analyzed the dynamics of AWs and AW constituent proteins to unravel the mechanisms of wave inception and propagation. Using live cell imaging and STED, we have characterized their growth cone-like morphology and motility and we have provided evidence that Myosin II, membrane composition, as well as small RhoGTPases act as critical components of AW dynamics. Our study suggests the existence of a cross-talk between actin cytoskeleton and its upstream regulators such as RhoGTPases, the motor protein Myosin and the cellular membrane integrity. These interactions are necessary to translocate the actin and associated proteins along the neurite.

AUTHOR CONTRIBUTIONS

VT and LN designed the research; SM and FI performed live-cell imaging experiments; ED performed STED experiments; AP developed the software for the analysis of live-cell imaging experiments; SM, FI, LN and VT analyzed data from live-cell imaging experiments; ED and DC analyzed data from STED experiments; VT, LN, SM and FI wrote the original draft; all the authors contributed to the review and the editing of the manuscript; VT supervised the entire work.

ACKNOWLEDGMENTS

We thank M. Lough for checking the English.

SUPPLEMENTARY MATERIAL

The Supplementary Material for this article can be found online at: https://www.frontiersin.org/articles/10.3389/fncel.2017.00402/full#supplementary-material

REFERENCES

Amin, L., Ercolini, E., Shahapure, R., Migliorini, E., and Torre, V. (2012). The role of membrane stiffness and actin turnover on the force exerted by DRG lamellipodia. *Biophys. J.* 102, 2451–2460. doi: 10.1016/j.bpj.2012.04.036

Bezanilla, M., Gladfelter, A. S., Kovar, D. R., and Lee, W.-L. (2015). Cytoskeletal dynamics: a view from the membrane. *J. Cell Biol.* 209, 329–337. doi: 10.1083/jcb.201502062

Bridgman, P. C., Dave, S., Asnes, C. F., Tullio, A. N., and Adelstein, R. S. (2001). Myosin IIB is required for growth cone motility. *J. Neurosci.* 21, 6159–6169.

Bubb, M. R., Senderowicz, A. M., Sausville, E. A., Duncan, K. L., and Korn, E. D. (1994). Jasplakinolide, a cytotoxic natural product, induces actin polymerization and competitively inhibits the binding of phalloidin to F-actin. *J. Biol. Chem.* 269, 14869–14871.

Burnette, D. T., Ji, L., Schaefer, A. W., Medeiros, N. A., Danuser, G., and Forscher, P. (2008). Myosin II activity facilitates microtubule bundling in the neuronal growth cone neck. *Dev. Cell* 15, 163–169. doi: 10.1016/j.devcel.2008.05.016

Burridge, K., and Wennerberg, K. (2004). Rho and Rac take center stage. *Cell* 116, 167–179. doi: 10.1016/S0092-8674(04)00003-0

Coles, C. H., and Bradke, F. (2015). Coordinating neuronal actin-microtubule dynamics. *Curr. Biol.* 25, R677–R691. doi: 10.1016/j.cub.2015.06.020

Danielson, E., and Lee, S. H. (2014). SynPAnal: software for rapid quantification of the density and intensity of protein puncta from fluorescence microscopy images of neurons. *PLoS ONE* 9:e115298. doi: 10.1371/journal.pone.0115298

Dent, E. W., Gupton, S. L., and Gertler, F. B. (2011). The growth cone cytoskeleton in axon outgrowth and guidance. *Cold Spring Harb. Perspect. Biol.* 3:a001800. doi: 10.1101/cshperspect.a001800

Dickson, B. J. (2001). Rho GTPases in growth cone guidance. *Curr. Opin. Neurobiol.* 11, 103–110. doi: 10.1016/S0959-4388(00)00180-X

Flynn, K. C., Pak, C. W., Shaw, A. E., Bradke, F., and Bamburg, J. R. (2009). Growth cone-like waves transport actin and promote axonogenesis and neurite branching. *Dev. Neurobiol.* 69, 761–779. doi: 10.1002/dneu.20734

Golomb, E., Ma, X., Jana, S. S., Preston, Y. A., Kawamoto, S., Shoham, N. G., et al. (2004). Identification and characterization of nonmuscle myosin II-C, a new member of the myosin II family. *J. Biol. Chem.* 279, 2800–2808. doi: 10.1074/jbc.M309981200

Göttfert, F., Wurm, C. A., Mueller, V., Berning, S., Cordes, V. C., Honigmann, A., et al. (2013). Coaligned dual-channel STED nanoscopy and molecular diffusion analysis at 20 nm resolution. *Biophys. J.* 105, L01–L03. doi: 10.1016/j.bpj.2013.05.029

Hall, A., and Nobes, C. D. (2000). Rho GTPases: molecular switches that control the organization and dynamics of the actin cytoskeleton. *Philos. Trans. R. Soc. Lond. B Biol. Sci.* 355, 965–970. doi: 10.1098/rstb.2000.0632

Holmes, W. R., Carlsson, A. E., and Edelstein-Keshet, L. (2012). Regimes of wave type patterning driven by refractory actin feedback: transition from static polarization to dynamic wave behaviour. *Phys. Biol.* 9:046005. doi: 10.1088/1478-3975/9/4/046005

Inagaki, N., and Katsuno, H. (2017). Actin Waves: origin of cell polarization and migration? *Trends Cell Biol.* 27, 515–526. doi: 10.1016/j.tcb.2017.02.003

Katsuno, H., Toriyama, M., Hosokawa, Y., Mizuno, K., Ikeda, K., Sakamura, Y., et al. (2015). Actin migration driven by directional assembly and disassembly of membrane-anchored actin filaments. *Cell Rep.* 12, 648–660. doi: 10.1016/j.celrep.2015.06.048

Komatsu, N., Aoki, K., Yamada, M., Yukinaga, H., Fujita, Y., Kamioka, Y., et al. (2011). Development of an optimized backbone of FRET biosensors for kinases and GTPases. *Mol. Biol. Cell* 22, 4647–4656. doi: 10.1091/mbc.E11-01-0072

Kovács, M., Tóth, J., Hetényi, C., Málnási-Csizmadia, A., and Sellers, J. R. (2004). Mechanism of blebbistatin inhibition of myosin II. *J. Biol. Chem.* 279, 35557–35563. doi: 10.1074/jbc.M405319200

Kovesi, P. (2000). Phase congruency: a low level image invariant. *Psychol. Res.* 64, 136–148. doi: 10.1007/s004260000024

Kubo, Y., Baba, K., Toriyama, M., Minegishi, T., Sugiura, T., Kozawa, S., et al. (2015). Shootin1-cortactin interaction mediates signal-force transduction for axon outgrowth. *J. Cell Biol.* 210, 663–676. doi: 10.1083/jcb.201505011

Lamoureux, P., Ruthel, G., Buxbaum, R. E., and Heidemann, S. R. (2002). Mechanical tension can specify axonal fate in hippocampal neurons. *J. Cell Biol.* 159, 499–508. doi: 10.1083/jcb.200207174

Lee, C., Choi, C., Shin, E., Schwartz, M. A., and Kim, E. (2010). Myosin II directly binds and inhibits Dbl family guanine nucleotide exchange factors: a possible link to Rho family GTPases. *J. Cell Biol.* 190:663. doi: 10.1083/jcb.201003057

Loudon, R. P., Silver, L. D., Yee, H. F., and Gallo, G. (2006). RhoA-kinase and myosin II are required for the maintenance of growth cone polarity and guidance by nerve growth factor. *J. Neurobiol.* 66, 847–867. doi: 10.1002/neu.20258

Lowery, L. A., and Van Vactor, D. (2009). The trip of the tip: understanding the growth cone machinery. *Nat. Rev. Mol. Cell Biol.* 10, 332–343. doi: 10.1038/nrm2679

Lukinavicius, G., Reymond, L., D'Este, E., Masharina, A., Gottfert, F., Ta, H., et al. (2014). Fluorogenic probes for live-cell imaging of the cytoskeleton. *Nat. Methods* 11, 731–733. doi: 10.1038/nmeth.2972

Machacek, M., Hodgson, L., Welch, C., Elliott, H., Pertz, O., Nalbant, P., et al. (2009). Coordination of Rho GTPase activities during cell protrusion. *Nature* 461, 99–103. doi: 10.1038/nature08242

Madden, K., and Snyder, M. (1998). Cell polarity and morphogenesis in budding yeast. *Annu. Rev. Microbiol.* 52, 687–744. doi: 10.1146/annurev.micro.52.1.687

Medeiros, N. A., Burnette, D. T., and Forscher, P. (2006). Myosin II functions in actin-bundle turnover in neuronal growth cones. *Nat. Cell Biol.* 8, 215–226. doi: 10.1038/ncb1367

Morales, M., Colicos, M. A., and Goda, Y. (2000). Actin-dependent regulation of neurotransmitter release at central synapses. *Neuron* 27, 539–550. doi: 10.1016/S0896-6273(00)00064-7

Nobes, C. D., and Hall, A. (1995). Rho, rac and cdc42 GTPases: regulators of actin structures, cell adhesion and motility. *Biochem. Soc. Trans.* 23, 456–459.

Pollard, T. D., and Borisy, G. G. (2003). Cellular motility driven by assembly and disassembly of actin filaments. *Cell* 112, 453–465. doi: 10.1016/S0092-8674(03)00120-X

Raftopoulou, M., and Hall, A. (2004). Cell migration: Rho GTPases lead the way. *Dev. Biol.* 265, 23–32. doi: 10.1016/j.ydbio.2003.06.003

Reymann, A. C., Boujemaa-Paterski, R., Martiel, J. L., Guérin, C., Cao, W., Chin, F., et al. (2012). Actin network architecture can determine myosin motor activity. *Science* 336, 1310–1314. doi: 10.1126/science.1221708

Ridley, A. J. (2011). Life at the leading edge. *Cell* 145, 1012–1022. doi: 10.1016/j.cell.2011.06.010

Riedl, J., Crevenna, A. H., Kessenbrock, K., Tu, J. H., Neukirchen, D., Bista, M., et al. (2008). Lifeact: a versatile marker to visualize F-actin. *Nat. Methods* 5, 605–607. doi: 10.1038/nmeth.1220

Rochlin, M. W., Itoh, K., Adelstein, R. S., and Bridgman, P. C. (1995). Localization of myosin II A and B isoforms in cultured neurons. *J. Cell. Sci.* 108(Pt 12), 3661–3670.

Ruthel, G., and Banker, G. (1998). Actin-dependent anterograde movement of growth-cone-like structures along growing hippocampal axons: a novel form of axonal transport? *Cell Motil. Cytoskeleton* 40, 160–173. doi: 10.1002/(SICI)1097-0169(1998)40:2<160::AID-CM5>3.0.CO;2-J

Ruthel, G., and Banker, G. (1999). Role of moving growth cone-like 'wave' structures in the outgrowth of cultured hippocampal axons and dendrites. *J. Neurobiol.* 39, 97–106. doi: 10.1002/(SICI)1097-4695(199904)39:1<97::AID-NEU8>3.0.CO;2-Z

Shutes, A., Onesto, C., Picard, V., Leblond, B., Schweighoffer, F., and Der, C. J. (2007). Specificity and mechanism of action of EHT 1864, a novel small molecule inhibitor of Rac family small GTPases. *J. Biol. Chem.* 282, 35666–35678. doi: 10.1074/jbc.M703571200

Surviladze, Z., Waller, A., Strouse, J. J., Bologa, C., Ursu, O., Salas, V., et al. (2010). *Probe Reports from the NIH Molecular Libraries Program*. National Center for Biotechnology Information, 2010.

Tilve, S., Difato, F., and Chieregatti, E. (2015). Cofilin 1 activation prevents the defects in axon elongation and guidance induced by extracellular alpha-synuclein. *Sci. Rep.* 5:16524. doi: 10.1038/srep16524

Tomba, C., Braïni, C., Bugnicourt, G., Cohen, F., Friedrich, B. M., Gov, N. S., et al. (2017). Geometrical determinants of neuronal actin waves. *Front. Cell. Neurosci.* 11:86. doi: 10.3389/fncel.2017.00086

Toriyama, M., Kozawa, S., Sakumura, Y., and Inagaki, N. (2013). Conversion of a signal into forces for axon outgrowth through Pak1-mediated shootin1 phosphorylation. *Curr. Biol.* 23, 529–534. doi: 10.1016/j.cub.2013.02.017

Van Goor, D., Hyland, C., Schaefer, A. W., and Forscher, P. (2012). The role of actin turnover in retrograde actin network flow in neuronal growth cones. *PLoS ONE* 7:e30959. doi: 10.1371/journal.pone.0030959

Vladislav, I. T., Gökmen-Polar, Y., Kesler, K. A., Loehrer, P. J., and Badve, S. (2013). The role of histology in predicting recurrence of type A thymomas: a clinicopathologic correlation of 23 cases. *Mod. Pathol.* 26, 1059–1064. doi: 10.1038/modpathol.2013.49

Weiner, O. D., Marganski, W. A., Wu, L. F., Altschuler, S. J., and Kirschner, M. W. (2007). An actin-based wave generator organizes cell motility. *PLoS Biol.* 5:e221. doi: 10.1371/journal.pbio.0050221

Wilkinson, S., Paterson, H. F., and Marshall, C. J. (2005). Cdc42-MRCK and Rho-ROCK signalling cooperate in myosin phosphorylation and cell invasion. *Nat. Cell Biol.* 7, 255–261. doi: 10.1038/ncb1230

Wilson, C. A., Tsuchida, M. A., Allen, G. M., Barnhart, E. L., Applegate, K. T., Yam, P. T., et al. (2010). Myosin II contributes to cell-scale actin network treadmilling through network disassembly. *Nature* 465, 373–377. doi: 10.1038/nature08994

Winans, A. M., Collins, S. R., and Meyer, T. (2016). Waves of actin and microtubule polymerization drive microtubule-based transport and neurite growth before single axon formation. *Elife* 5:e12387. doi: 10.7554/eLife.12387

Wu, C., Schulte, J., Sepp, K. J., Littleton, J. T., and Hong, P. (2010). Automatic robust neurite detection and morphological analysis of neuronal cell cultures in high-content screening. *Neuroinformatics* 8, 83–100. doi: 10.1007/s12021-010-9067-9

Wu, M., Wu, X., and De Camilli, P. (2013). Calcium oscillations-coupled conversion of actin travelling waves to standing oscillations. *Proc. Natl. Acad. Sci. U.S.A.* 110, 1339–1344. doi: 10.1073/pnas.1221538110

Conflict of Interest Statement: The authors declare that the research was conducted in the absence of any commercial or financial relationships that could be construed as a potential conflict of interest.

frontiers

Supplementary Material

Actin Waves do not boost neurite outgrowth in the early stages of neuron maturation.

S. Mortal[1,*], F.Iseppon[1,*], A. Perissinotto[1], E. D'Este[2], D. Cojoc[3], L.M.R. Napolitano[1], and V. Torre[1]

[1] International School for Advanced Studies, Trieste 34126, Italy;
[2] Department of NanoBiophotonics, Max Planck Institute for Biophysical Chemistry, 37077 Göttingen, Germany
[3] Optical Manipulation Lab, CNR-IOM, Trieste 34149, Italy;

[*]These authors equally contributed to this work

To whom correspondence should be addressed: Vincent Torre; e-mail: torre@sissa.it.

Keywords: Actin Waves (AWs); Growth Cones (GCs); Myosin IIB; ß-cyclodextrin; RhoGTPases.

1.1 Supplementary Figures

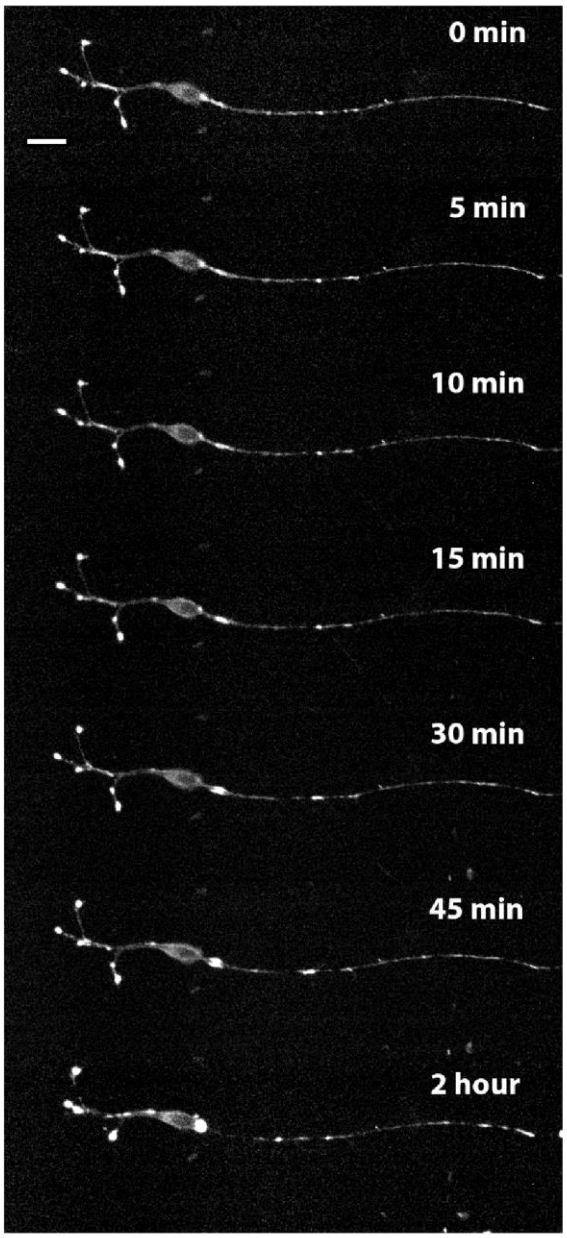

Supplementary Figure 1. SiR-Actin induces a decrease of AWs. Timelapse images of a hippocampal cell expressing the membrane-permeable SiR-Actin [1 μM]. We observed the absence of AWs presumably due to the presence of jasplakinolide (Bubb et al., 1994; Winans et al., 2016). Scalebar = 20 μm.

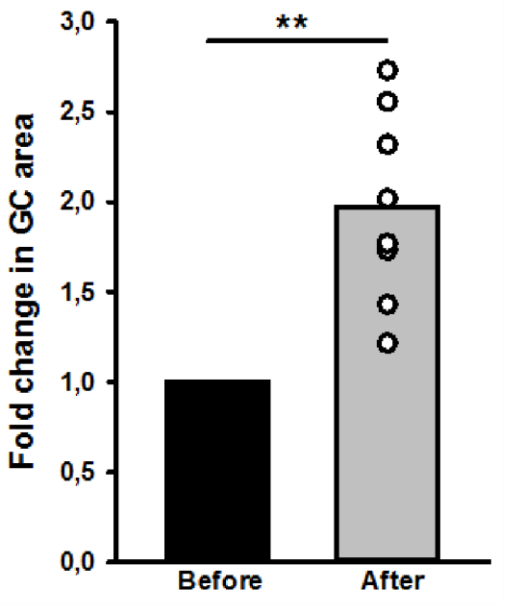

Supplementary Figure 2. Wave arrival affects GC morphology. Histogram showing a significant increase in GC area after the arrival and merge of an AW (n=8 AWs). The data were normalized by the GC area computed before the AW arrival. Student's test was performed for histograms: **P<0.01.

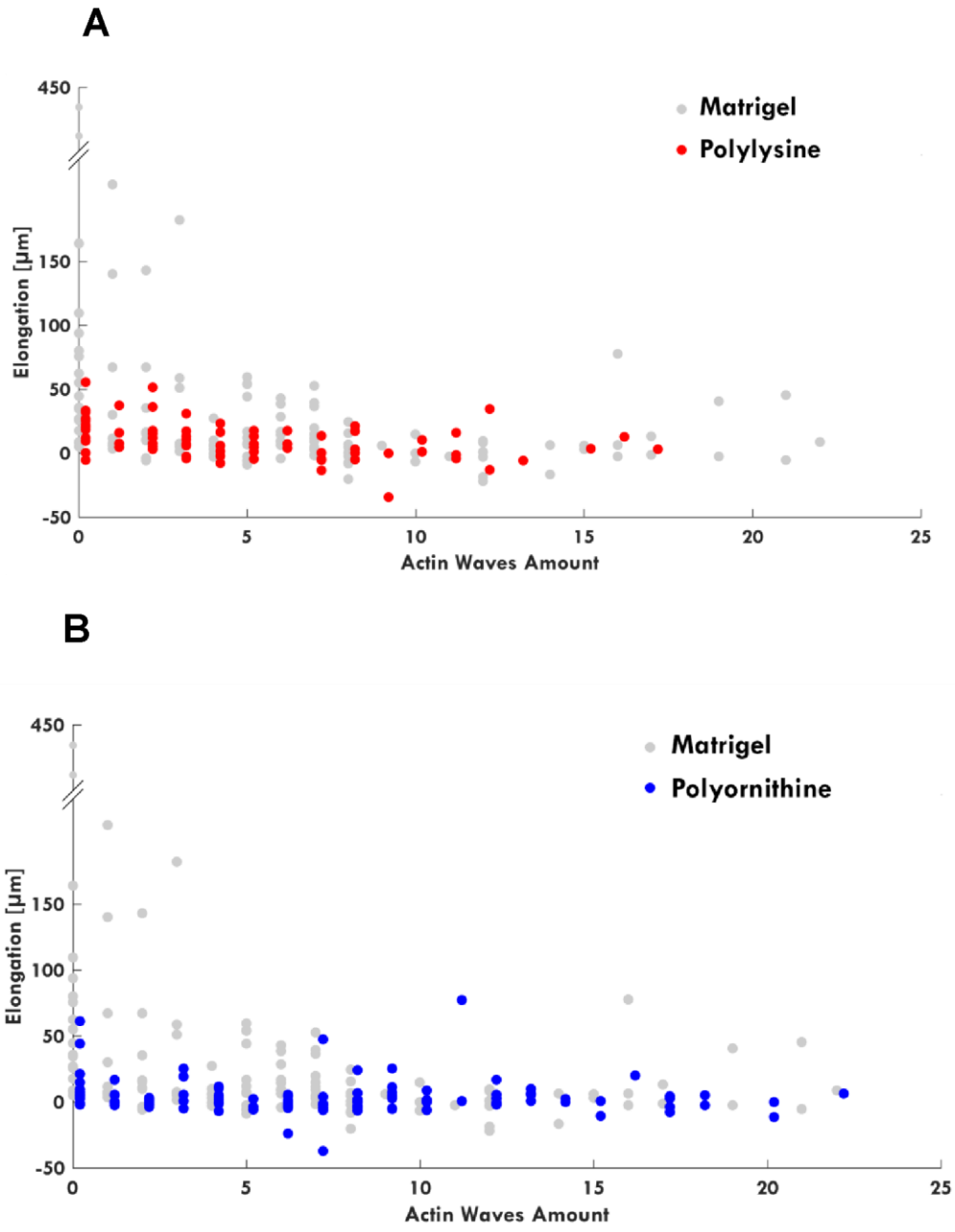

Supplementary Figure 3. AWs behaviour on different substrates. (A-B) Graph showing the elongation of the neurites (y axis) per number of actin waves (x axis) imaged at 1-5 minutes intervals for 8 hours in the presence of different substrates. In all three cases we were able to observe that AWs do not boost neurite outgrowth and neurites without AWs can elongate more. According to the literature (Dent et al., 2007), neurites could grow more on Matrigel than on the other substrates. Red dots refer poly-D-lysine n=76; light grey dots refer to Matrigel; blue dots refer to poly-L-ornithine n=122.

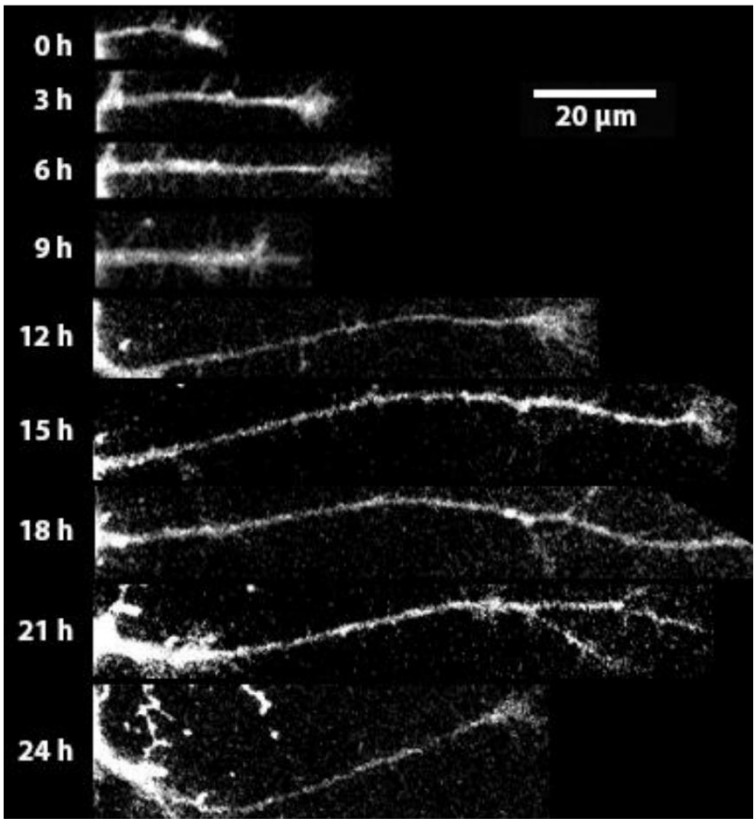

Supplementary Figure 4. AWs do not induce neurite outgrowth. Timelapse images a neurite stained with Vybrant DiI and followed for 24 Hours. As highlighted in the plots showed in Figure 3C-D the neurite elongates in the absence of AWs, while it retracts in the presence of AWs. Scale bar = 20 µm

5

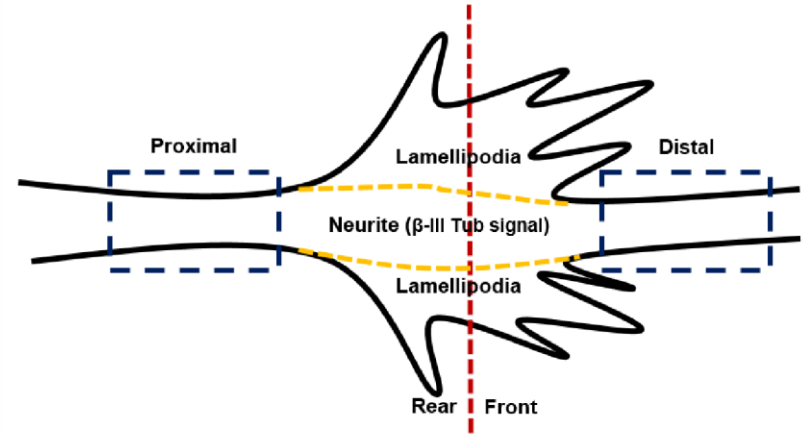

Supplementary Figure 5. STED images analysis scheme. Scheme of the concept and Regions Of Interest (ROIs) taken into consideration in the analysis of Myosin-IIB puncta. The Neurite region (yellow dashed lines) takes into consideration the central region of the AW, the prosecution of the β-III Tubulin-rich neurite, and is divided into Rear and Front (red dashed line) halves. The Lamellipodia region comprises all the peripheral structures that protrude from the central neurite. The Proximal and Distal sections (Blue dashed boxes) refer to the regions (of the same length) immediately before the beginning and after the front of the AW, respectively.

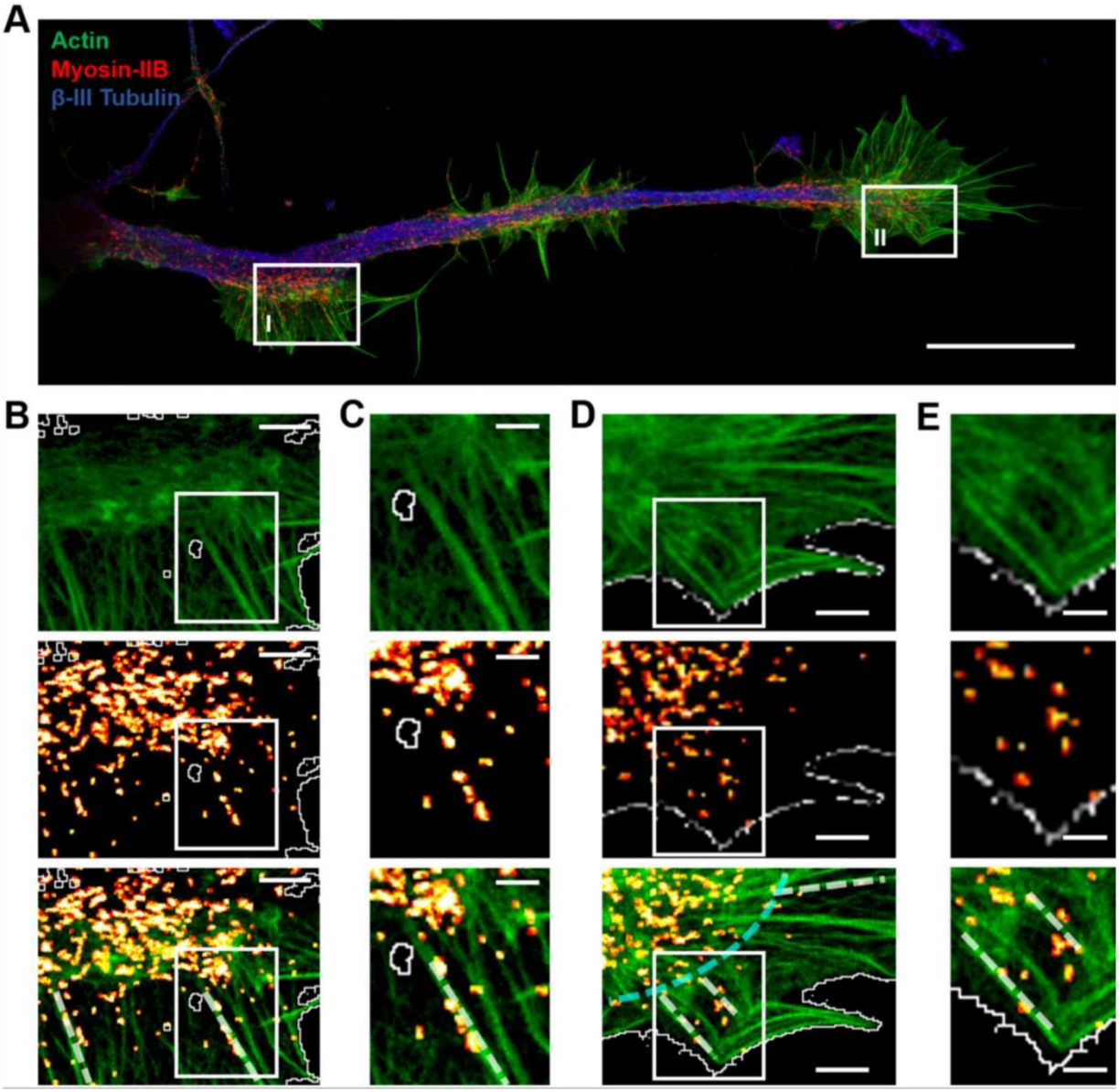

Supplementary Figure 6. Myosin central and peripheral puncta localization in GCs and AWs. **(A)** STED image of a rat hippocampal neuron at 1 DIV stained with actin (phalloidin, green), non-muscle myosin IIB (red) and ß-III tubulin (blue). Scalebar = 10µm **(B)** Magnifications of the region, delimited by white box "I" of the image in (A) showing the actin (top panel), myosin IIB (middle panel) and both (bottom panel) channels highlighting how myosin IIB spots change organization from a sparse localization in the central region of the AW to pinpointing along thicker actin filaments. Scalebar = 1µm **(C)** Magnifications of the area delimited by the white boxes in (B) of the border between the central and peripheral regions of the AW, with a dense actin network sparse myosin spots, and the peripheral region, where the spots organize along actin filaments, as highlighted by the white dashed lines in the bottom panels in (B, C). Scalebar = 500nm. 10µm **(D)** Same as in (B), but the magnifications refer to white box "II". In this case the magnification highlights a clear arc-like myosin organization (cyan dashed line) in the transition region between the dense central region and the periphery, where myosin puncta tend to localize along actin filaments (white dashed lines). Scalebar = 1µm **(E)** Same as in (C), but the magnified area is delimited by the white boxes in (D). Scalebar = 500nm.

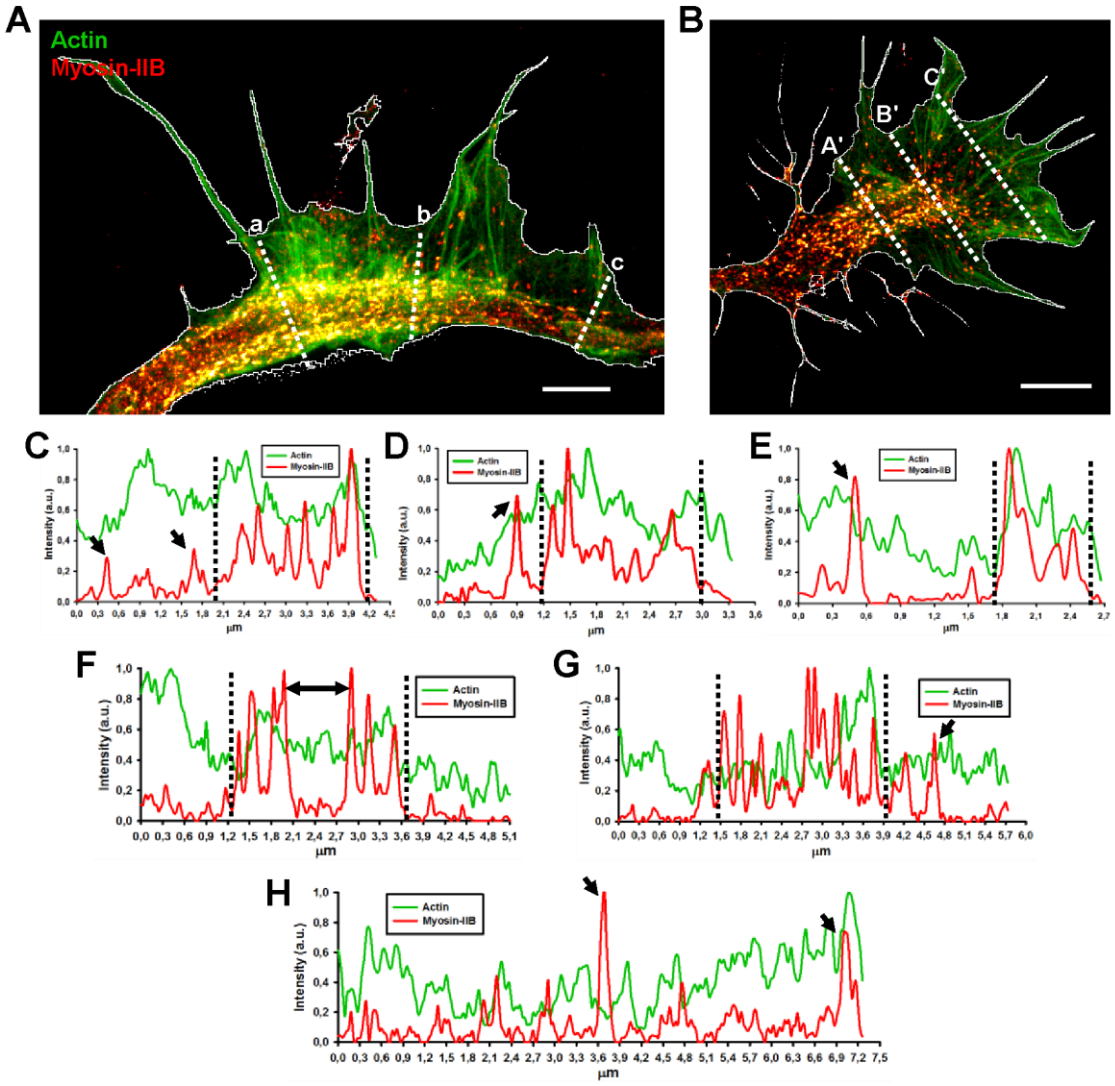

Supplementary Figure 7. Image Profiles reveal differences in acto-myosin organization between GCs and AWs. (A,B) STED images of actin (green) and myosin IIB (red) channels of the AW and GC of the cell in Figure 4. Scalebars in (A, B) = 2µm **(C, D, E)** Image profiles of actin and myosin IIB along the pointed lines in (A), showing different profiles for the rear (a→(C)), the centre (b→(D)) and the front (c→E)) of the travelling AW. The neurite central region is clearly visible in all three profiles (between the black pointed lines in (C, D, E)), where myosin IIB intensity is higher and the puncta are wider, whereas in the peripheral region single spots prevail (black arrows). **(F, G, H)** Image profiles of actin and myosin IIB along the pointed lines in (B), showing different profiles for the rear (A'→(F)), the centre (B'→(G)) and the front (C'→H)) of the GC. The central region of the GC is clearly visible in (F) and (G) (between the black pointed lines), where myosin IIB intensity is higher and the puncta are more frequent. The black double arrow in (F) highlights the lack of myosin puncta that are concentrated along the acto-myosin arcs in the transition zone. In the peripheral region (H) myosin is organized in single puncta that concentrate along actin structures (black arrows).

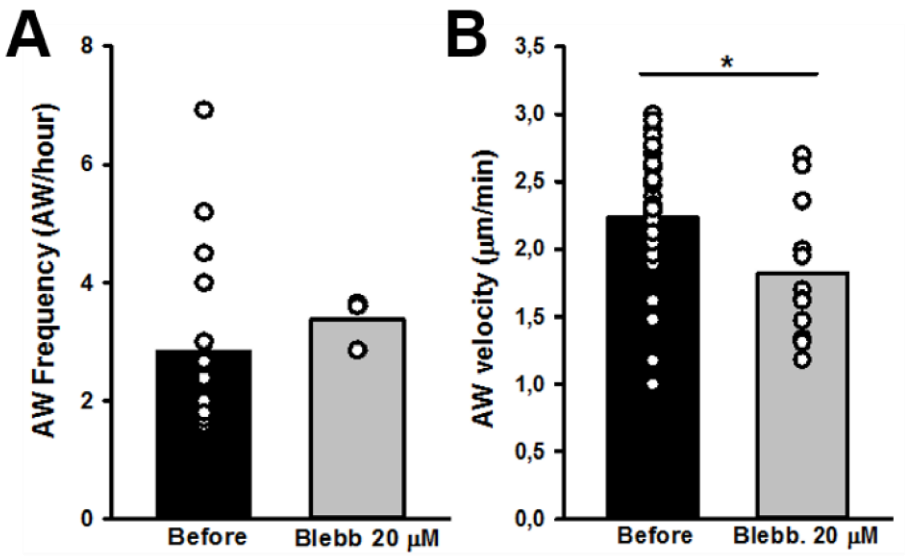

Supplementary Figure 8. Blebbistatin effect on AWs' velocity and frequency. A) Quantification of the AWs frequency calculated on neurons treated with or without blebbistatin for 4 hours and imaged like in Figure 4A-4B. N = 4 neurites **(B)** Quantification of the AWs velocity (µm/min) calculated on neurons treated with or without blebbistatin for 4 hours and imaged like in Figure 6A-6B. N = 18 AWs.

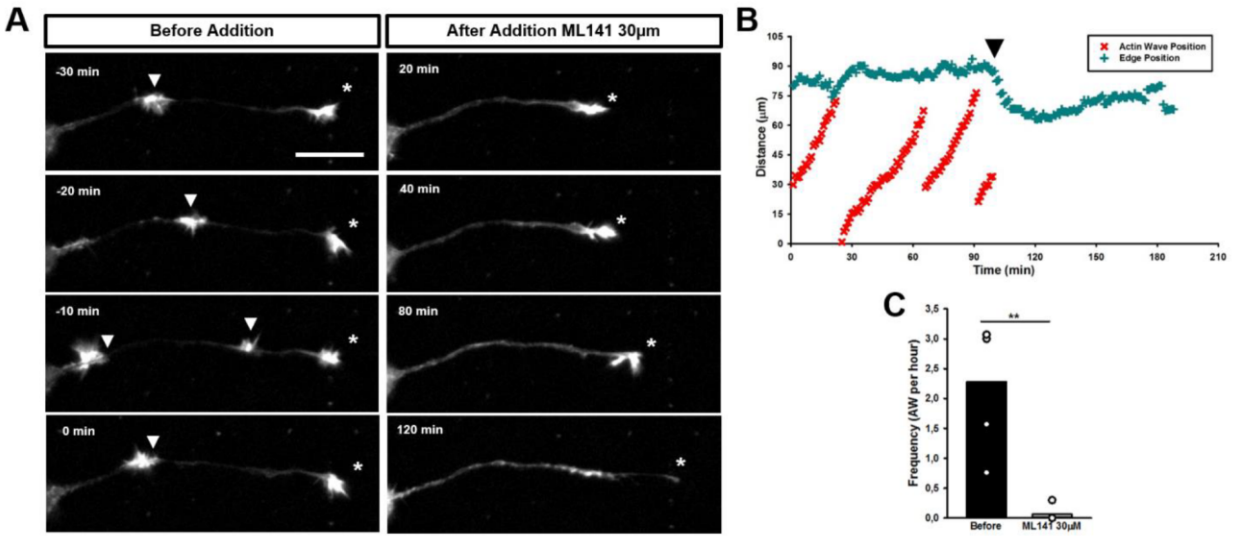

Supplementary Figure 9. Cdc42 potent inhibition affects AW dynamics. (A) Time-lapse live cell imaging of DIV2 rat hippocampal neurons before (left) and after (right) addition of ML141 (30µM). White arrow indicates the growth cone-like AW. The asterisk indicates the GC. Scale bars = 20µm. **(B)** Plot showing the progression of several AWs (red) along the neurite shaft. The edge trace (light blue) highlights neurite retraction concurrent with complete AW disappearence after ML141 treatment. Black arrowhead indicates ML141 addition. **(C)** Quantification of the AWs frequency calculated on neurons treated with or without ML141 for 4 hours and imaged like in (A) and (B). N= 9AWs. Student's test was performed for histograms: **P<0.01.

Supplementary Video

Supplementary Video 1. AWs exhibit a growth cone-like morphology and travel in an anterograde fashion in our 1 and 2 DIV imaging windows. This movie shows time-lapse images from the entire frame of acquisition (8 hrs) for mCherry-LifeAct expressing neurons. Images were collected every 5 seconds and the movie was generated at 15 frames per 1 second. Scale bar= 20 µm.

Supplementary Video 2: This movie shows time-lapse images from the entire frame of acquisition for mCherry-LifeAct expressing neurons plated on poly-D-Lysine substrate. Images were collected every 10 seconds and the movie was generated at 7 frame per 1 second. Scale bar= 20 µm.

Supplementary Video 3: This movie shows time-lapse images from the entire frame of acquisition for mCherry-LifeAct expressing neurons plated on poly-L-L-Ornithine substrate. Images were collected every 10 seconds and the movie was generated at 15 frame per 1 second. Scale bar= 20 µm

Supplementary Video 4. AWs are observed in DIV1 hippocampal neurons stained with a membrane marker. This movie shows timelapse images of a DiI-expressing neuron producing AWs. Images were collected every 5 min and the movie was generated at 29 frames per second. Scale bar= 100 µm.

Supplementary Video 5. Neurites with no or few AWs grow up to 450 µm. This movie shows time-lapse images from the entire frame of acquisition (8 hrs) for mCherry-LifeAct expressing neurons.

Images were collected every 1 min and the movie was generated at 25 frames per second. Scale bar=100 μm.

Supplementary Video 6: Blebbistatin treatment (20μM) changes the morphology of the wave that loses the characteristic growth-cone shape and abolishes completely the GC. This movie shows time-lapse images from the entire frame of acquisition (3 hrs) for mCherry-LifeAct expressing neurons. Images were collected every 10 seconds and the movie was generated at 15 frames per 1 second. Scale bar= 20 μm.

.

2.2 Tubulin twists drive Growth Cone retraction and promote tubulin mixed polarity

Simone Mortal & Vincent Torre

Original Research ARTICLE

Manuscript in preparation

Tubulin twists drive Growth Cone retraction and promote tubulin mixed polarity

Simone Mortal[1*] & Vincent Torre[1,2]

Corresponding Author: smortal@sissa.it

[1] Neurobiology Department, International School for Advanced Studies, Trieste, Italy

[2]Joint Laboratory of Biophysics and Translational Medicine, ISM-SISSA, Suzhou Industrial Park, Jiangsu, 215123, China

Abstract

Microtubules are formed by tubulin heterodimers and are the main building blocks of the cytoskeleton. Microtubules are considered rigid structures and their flexural rigidity is 1000 times larger than that of actin filaments. We performed live cell imaging of developing neurons by staining actin with LifeAct and by marking tubulin with Sirtubulin. Under these conditions, microtubules have sharp bends which are not apparent upon fixation. These Tubulin twists (TT) are often associated with actin waves (AW) and disappear after inhibition of myosin. Formation of TT is promoted by the myosin activator 4'-HAP. TTs represent a fast mechanism for neurites shortening. In addition, TTs remodel the tubulin polarity creating kinks so that following severing of the microtubules, the obtained segments have opposite polarity as seen in dendrites but never explained.

Background

During neuronal development, the cytoskeleton architecture undergoes important modifications as neurites start to sprout out from the soma and explore the surrounding environment. Tubulin and Actin are the key players in this process, and the fast outgrowth of the microtubules provides support and rigidity during neurite elongation[46]. The fast actin remodeling promotes the growth cone mobility for the correct pathfinding and Actin Waves maintain the growth cone shape and provoke the typical pulling effect[3,20]. In the great majority of cases observed so far however, microtubules appear straight and exhibit a significant rigidity prohibiting kinks and sharp bending[67]. In contrast, by performing live imaging using indicators which have only recently become available, we found that tubulin is actually rather dynamic, and bends and twists in concert with actin waves.

What we have done

We performed live cell imaging of developing neurons by staining actin with LifeAct (Ibidi) and tubulin marked with Sirtubulin (Cytoskeleton, Inc). We found that:

- Microtubules can have TTs
- TTs are associated to AWs
- TTs disappear after inhibition of myosin II
- TTs are promoted by the myosin activator 4'-HAP[66]

Results

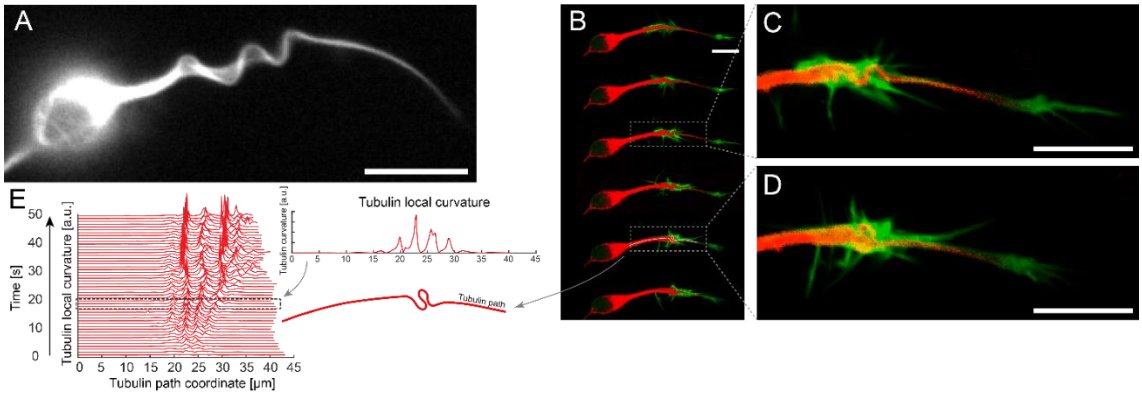

Figure1. Tubulin twists. A. Example of the transient bending of tubulin. B. Time-lapse of a living neuron stained in green for Actin and in red for tubulin. It is possible to observe the appearance of the tubulin twists, in the magnification in C and D. E. Plot of the tubulin local curvature of the neurite for multiple timepoints. Scalebar = 10 µm.

We performed live cell imaging of dissociated neurons during the first three days of development. We observed the appearance of kinks and twists in microtubules (Fig. 1 A, B). Tubulin twists (TTs) were coincident with an Actin Wave (AW), but not all the AW had a TT. While the AW proceeds along the neurite, often the microtubules bend leading to the classical retraction of the growth[3,20]. To quantify these phenomena, we computed the local curvature along the length (Fig 1E).

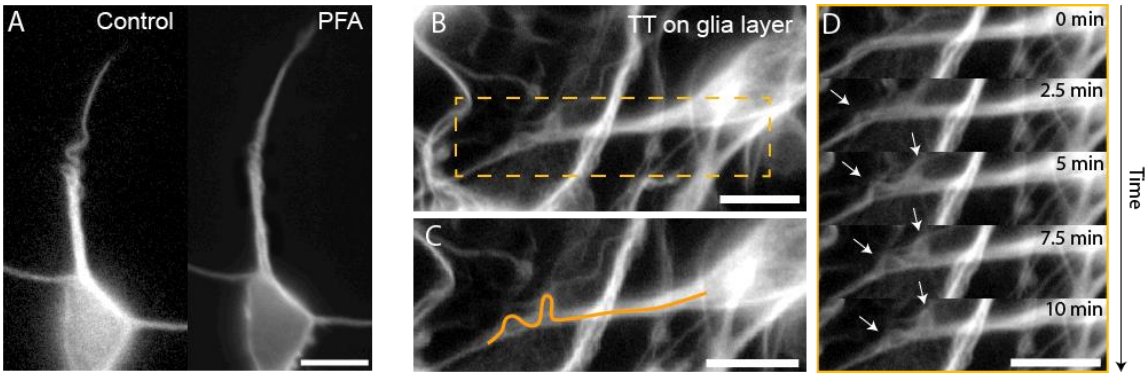

Figure 2. A. Comparison of a TT before and after the addition of 4% PFA. B. TT on an astrocytes carpet. C. Reconstruction (in orange) of the TT shown in B. D. Time-lapse of a living neuron while it performs TTs. Scalebar = 10 µm.

TTs were rarely observed when developing neurons were fixed and tubulin and actin are imaged with conventional immunofluorescence. Therefore, we verified that TT clearly present in live cell imaging experiments disappeared after a fast fixation with PFA (Fig.2A). TTs were still observed when neurons where cultured and grown on a carpet of glia cells (Fig.2B-D).

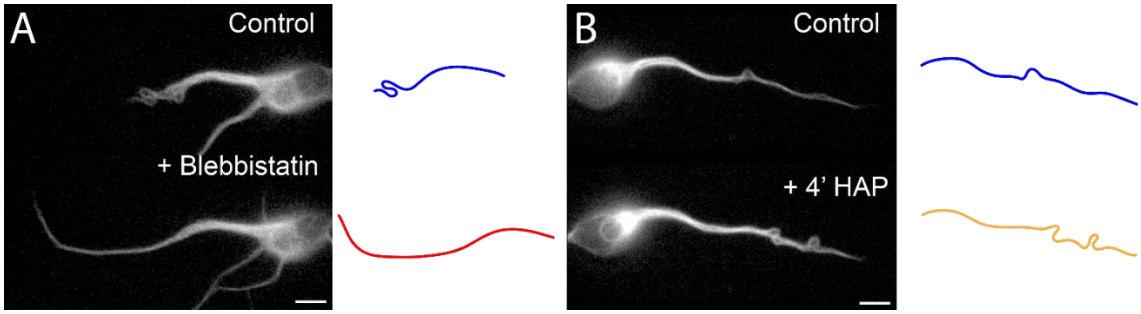

Figure 3. A. Blebbistatin effect, we tested the effect of blebbistatin on TTs before, there is a normal TTs activity. After the addition of blebbistatin 20 µM, we can observe neurite outgrowth and the disappearance of the TTs. B. 4'-HAP effect, after addition of 4'-HAP 50 µM, we can observe an increment in the tubulin twists appearance. Scalebar = 10 µm.

The formation of a TT requires the action of a strong force able to bend the rigid microtubes. We found that the addition of Blebbistatin a well-known inhibitor of myosin II, instantly promotes the neurite outgrowth, modifies the AW and most importantly abolishes the TTs (Fig. 3A). To confirm this AW-TT link, we tested the effect of the application of 4'-HAP, a well-known myosin activator[66]. This compound enhances the myosin contractility and induces more frequent TTs (Fig.3B).

Conclusions

The present MS shows that in contrast with the current view of microtubules, these structures are not rigid and undergo reversible bending. TT have two fundamental functions, never envisaged before:

- TTs represent a fast mechanism (Fig.4A) by which neurites can shorten their length, which is likely to be necessary during development when growth cones have to find their final destination.
- TTs are the cause of the pulling effect previously described Routhel and Banker 1998[3] but never fully understood.
- TTs remodel the tubulin polarity creating kinks so that following severing of the microtubes the obtained segments have opposite polarity (Fig.4B) as seen in dendrites but never explained.

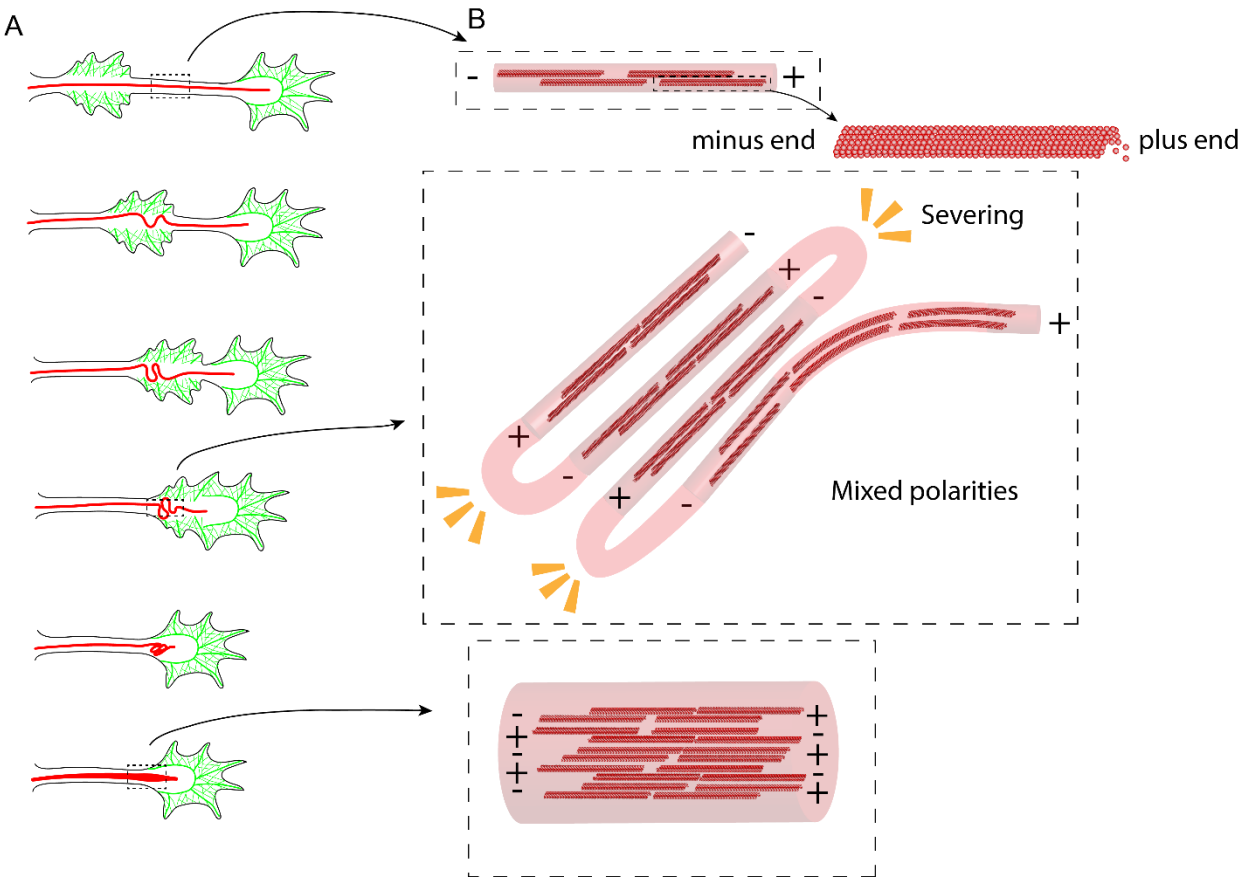

Figure 4. Model of the TT dynamics. A. TT formation during the AW traveling. B. Model to make the microtubules mixed polarity.

Conclusions

AWs were discovered in 1988 by Ruthel and Banker as wave-like membrane protrusions containing actin filaments along the axons and immature neurites of cultured rat hippocampal neurons[3]. These authors proposed a key role for the AWs in transporting actin and associated proteins to the GC at the tip of an extending axon[3,20]. In this 20 years, other groups found a dual role for AWs as drivers in the neurite extension and in the growth cone exploration[21,24,29]. Here we describe AWs generated at a frequency of 1 wave every 20 minutes and with an average speed of ~2-3 μm per minute. Long term live cell imaging experiments reveal that the constant arrival of AWs generates retraction/elongation cycles, resulting in a transient increase of GC size and not in a net neurite elongation. This incongruity with other studies could be related to the use of P1-P2 hippocampal neurons, while previous studies used embryonic mouse or rats[29,51,68]. Indeed, “older” neurons can exhibit a different behaviour. It is also true that my work is the first one to give a complete picture of the long-term behaviour of the AWs, that although not promoting neurite elongation, seems to contribute in neuronal polarization as suggested in other papers[21,28,29]. AWs can even contribute in the GC support. In fact, the GC continuously reduces its size during environment exploration and recover its original size after the arrival of an AW, that provides fresh actin oligomers and other metabolic product.

From there I started wondering if the AWs can influence other cytoskeletal components, so that I investigated the possibility of a crosstalk with microtubules. I found that the pulling effect of the AWs is due to the bending of tubulin and I named this phenomenon as tubulin twist. Despite the large dimensions, this structure was surprisingly never observed, and my explanation is that only the use of live imaging in young neurons combined with new dyes could give the opportunity to observe TTs. In fact, the studies on cytoskeleton are usually done on fixed cells, where is impossible to observe this structures, and historically very poor attention has been reserved to AWs. In addition, the huge problem of transfection in primary cultures has probably contributed to postpone the discovery of TTs.

To conclude, I think that this novel structure producing kinks in the microtubules might produce tubulin segments with opposite polarity. Thus, the microtubule mixed polarity induced by TTs is a fundamental component of the dendrites and part of the axon. Therefore, the TTs should be considered as part of the mechanism that leads the neurites to their maturation in axons and dendrites.

References

1. Dotti, C. G., Sullivan, C. A. & Banker, G. A. The establishment of polarity by hippocampal neurons in culture. *J. Neurosci.* **8**, 1454–1468 (1988).

2. Lien, T. L. *et al.* Can Hippocampal Neurites and Growth Cones Climb over Obstacles? *PLoS ONE* **8**, e73966 (2013).

3. Ruthel, G. & Banker, G. Actin-dependent anterograde movement of growth-cone-like structures along growing hippocampal axons: A novel form of axonal transport? *Cell Motil. Cytoskeleton* **40**, 160–173 (1998).

4. Nixon, R. A. & Shea, T. B. Dynamics of neuronal intermediate filaments: A developmental perspective. *Cell Motil.* **22**, 81–91 (1992).

5. Otterbein, L. R., Graceffa, P. & Dominguez, R. The Crystal Structure of Uncomplexed Actin in the ADP State. *Science* **293**, 708–711 (2001).

6. The nature of the globular- to fibrous-actin transition | Nature. https://www.nature.com/articles/nature07685.

7. Reisler, E. & Egelman, E. H. Actin Structure and Function: What We Still Do Not Understand. *J. Biol. Chem.* **282**, 36133–36137 (2007).

8. Lowery, L. A. & Vactor, D. V. The trip of the tip: understanding the growth cone machinery. *Nat. Rev. Mol. Cell Biol.* **10**, 332–343 (2009).

9. Mattila, P. K. & Lappalainen, P. Filopodia: molecular architecture and cellular functions. *Nat. Rev. Mol. Cell Biol.* **9**, 446–454 (2008).

10. Mattila, P. K. & Lappalainen, P. Filopodia: molecular architecture and cellular functions. *Nat. Rev. Mol. Cell Biol.* **9**, 446–454 (2008).

11. Traction Dynamics of Filopodia on Compliant Substrates | Science. https://science.sciencemag.org/content/322/5908/1687.long.

12. Myosin II functions in actin-bundle turnover in neuronal growth cones | Nature Cell Biology. https://www.nature.com/articles/ncb1367.

13. Dynamic instability of microtubule growth | Nature. https://www.nature.com/articles/312237a0.

14. Rapid Actin Transport During Cell Protrusion | Science. https://science.sciencemag.org/content/300/5616/142.

15. Hu, K., Ji, L., Applegate, K. T., Danuser, G. & Waterman-Storer, C. M. Differential Transmission of Actin Motion Within Focal Adhesions. *Science* **315**, 111–115 (2007).

16. Bard, L. *et al.* A Molecular Clutch between the Actin Flow and N-Cadherin Adhesions Drives Growth Cone Migration. *J. Neurosci.* **28**, 5879–5890 (2008).

17. Mogilner, A. On the edge: modeling protrusion. *Curr. Opin. Cell Biol.* **18**, 32–39 (2006).

18. Robles, E. & Gomez, T. M. Focal adhesion kinase signaling at sites of integrin-mediated adhesion controls axon pathfinding. *Nat. Neurosci.* **9**, 1274–1283 (2006).

19. Koh, C.-G. Rho GTPases and Their Regulators in Neuronal Functions and Development. *Neurosignals* **15**, 228–237 (2006).

20. Ruthel, G. & Banker, G. Role of moving growth cone-like 'wave' structures in the outgrowth of cultured hippocampal axons and dendrites. *J. Neurobiol.* **39**, 97–106 (1999).

21. Flynn, K. C., Pak, C. W., Shaw, A. E., Bradke, F. & Bamburg, J. R. Growth cone-like waves transport actin and promote axonogenesis and neurite branching. *Dev. Neurobiol.* **69**, 761–779 (2009).

22. Strasser, G. A., Rahim, N. A., VanderWaal, K. E., Gertler, F. B. & Lanier, L. M. Arp2/3 Is a Negative Regulator of Growth Cone Translocation. *Neuron* **43**, 81–94 (2004).

23. Tint, I., Jean, D., Baas, P. W. & Black, M. M. Doublecortin Associates with Microtubules Preferentially in Regions of the Axon Displaying Actin-Rich Protrusive Structures. *J. Neurosci.* **29**, 10995–11010 (2009).

24. Katsuno, H. *et al.* Actin Migration Driven by Directional Assembly and Disassembly of Membrane-Anchored Actin Filaments. *Cell Rep.* **12**, 648–660 (2015).

25. Shootin1: a protein involved in the organization of an asymmetric signal for neuronal polarization | JCB. http://jcb.rupress.org/content/175/1/147.short.

26. Vale, R. D. *et al.* Direct observation of single kinesin molecules moving along microtubules. *Nature* **380**, 451–453 (1996).

27. Howard, J. Molecular motors: structural adaptations to cellular functions. *Nature* **389**, 561–567 (1997).

28. Inagaki, N. & Katsuno, H. Actin Waves: Origin of Cell Polarization and Migration? *Trends Cell Biol.* **27**, 515–526 (2017).

29. Winans, A. M., Collins, S. R. & Meyer, T. Waves of actin and microtubule polymerization drive microtubule-based transport and neurite growth before single axon formation. *eLife* **5**, e12387 (2016).

30. Akhmanova, A. & Steinmetz, M. O. Tracking the ends: a dynamic protein network controls the fate of microtubule tips. *Nat. Rev. Mol. Cell Biol.* **9**, 309–322 (2008).

31. Barnes, A. P. & Polleux, F. Establishment of Axon-Dendrite Polarity in Developing Neurons. *Annu. Rev. Neurosci.* **32**, 347–381 (2009).

32. Kuijpers, M. & Hoogenraad, C. C. Centrosomes, microtubules and neuronal development. *Mol. Cell. Neurosci.* **48**, 349–358 (2011).

33. Lipka, J., Kuijpers, M., Jaworski, J. & Hoogenraad, C. C. Mutations in cytoplasmic dynein and its regulators cause malformations of cortical development and neurodegenerative diseases. *Biochem. Soc. Trans.* **41**, 1605–1612 (2013).

34. Reiner, O. & Sapir, T. LIS1 functions in normal development and disease. *Curr. Opin. Neurobiol.* **23**, 951–956 (2013).

35. Baas, P. W. & Lin, S. Hooks and comets: The story of microtubule polarity orientation in the neuron. *Dev. Neurobiol.* **71**, 403–418 (2011).

36. Conde, C. & Cáceres, A. Microtubule assembly, organization and dynamics in axons and dendrites. *Nat. Rev. Neurosci.* **10**, 319–332 (2009).

37. Howard, J. & Hyman, A. A. Growth, fluctuation and switching at microtubule plus ends. *Nat. Rev. Mol. Cell Biol.* **10**, 569–574 (2009).

38. Alushin, G. M. *et al.* High-Resolution Microtubule Structures Reveal the Structural Transitions in αβ-Tubulin upon GTP Hydrolysis. *Cell* **157**, 1117–1129 (2014).

39. Akhmanova, A. & Hoogenraad, C. C. Microtubule Minus-End-Targeting Proteins. *Curr. Biol.* **25**, R162–R171 (2015).

40. Dehmelt, L. & Halpain, S. The MAP2/Tau family of microtubule-associated proteins. *Genome Biol.* **6**, 204 (2004).

41. Subramanian, R. & Kapoor, T. M. Building Complexity: Insights into Self-Organized Assembly of Microtubule-Based Architectures. *Dev. Cell* **23**, 874–885 (2012).

42. Kollman, J. M., Merdes, A., Mourey, L. & Agard, D. A. Microtubule nucleation by γ-tubulin complexes. *Nat. Rev. Mol. Cell Biol.* **12**, 709–721 (2011).

43. Sharp, D. J. & Ross, J. L. Microtubule-severing enzymes at the cutting edge. *J. Cell Sci.* **125**, 2561–2569 (2012).

44. Hirokawa, N., Niwa, S. & Tanaka, Y. Molecular Motors in Neurons: Transport Mechanisms and Roles in Brain Function, Development, and Disease. *Neuron* **68**, 610–638 (2010).

45. Hammond, J. W. *et al.* Posttranslational modifications of tubulin and the polarized transport of kinesin-1 in neurons. *Mol. Biol. Cell* **21**, 572–583 (2010).

46. Kapitein, L. C. & Hoogenraad, C. C. Building the Neuronal Microtubule Cytoskeleton. *Neuron* **87**, 492–506 (2015).

47. Nakata, T. & Hirokawa, N. Microtubules provide directional cues for polarized axonal transport through interaction with kinesin motor head. *J. Cell Biol.* **162**, 1045–1055 (2003).

48. Kapitein, L. C. *et al.* Mixed Microtubules Steer Dynein-Driven Cargo Transport into Dendrites. *Curr. Biol.* **20**, 290–299 (2010).

49. Mechanisms of cell migration in the nervous system | JCB. http://jcb.rupress.org/content/202/5/725.

50. Cáceres, A., Ye, B. & Dotti, C. G. Neuronal polarity: demarcation, growth and commitment. *Curr. Opin. Cell Biol.* **24**, 547–553 (2012).

51. Flynn, K. C. *et al.* ADF/Cofilin-Mediated Actin Retrograde Flow Directs Neurite Formation in the Developing Brain. *Neuron* **76**, 1091–1107 (2012).

52. Nakata, T., Niwa, S., Okada, Y., Perez, F. & Hirokawa, N. Preferential binding of a kinesin-1 motor to GTP-tubulin–rich microtubules underlies polarized vesicle transport. *J. Cell Biol.* **194**, 245–255 (2011).

53. Hellal, F. *et al.* Microtubule Stabilization Reduces Scarring and Causes Axon Regeneration After Spinal Cord Injury. *Science* **331**, 928–931 (2011).

54. Ruschel, J. *et al.* Systemic administration of epothilone B promotes axon regeneration after spinal cord injury. *Science* **348**, 347–352 (2015).

55. Hoogenraad, C. C. & Bradke, F. Control of neuronal polarity and plasticity – a renaissance for microtubules? *Trends Cell Biol.* **19**, 669–676 (2009).

56. Centrosome biogenesis and function: centrosomics brings new understanding | Nature Reviews Molecular Cell Biology. https://www.nature.com/articles/nrm2180?cacheBust=1510042456573.

57. Kapitein, L. C. & Hoogenraad, C. C. Which way to go? Cytoskeletal organization and polarized transport in neurons. *Mol. Cell. Neurosci.* **46**, 9–20 (2011).

58. Woolner, S. & Bement, W. M. Unconventional myosins acting unconventionally. *Trends Cell Biol.* **19**, 245–252 (2009).

59. Hartman, M. A., Finan, D., Sivaramakrishnan, S. & Spudich, J. A. Principles of Unconventional Myosin Function and Targeting. *Annu. Rev. Cell Dev. Biol.* **27**, 133–155 (2011).

60. Odronitz, F. & Kollmar, M. Drawing the tree of eukaryotic life based on the analysis of 2,269 manually annotated myosins from 328 species. *Genome Biol.* **8**, R196 (2007).

61. Kneussel, M. & Wagner, W. Myosin motors at neuronal synapses: drivers of membrane transport and actin dynamics. *Nat. Rev. Neurosci.* **14**, 233–247 (2013).

62. Vicente-Manzanares, M., Ma, X., Adelstein, R. S. & Horwitz, A. R. Non-muscle myosin II takes centre stage in cell adhesion and migration. *Nat. Rev. Mol. Cell Biol.* **10**, 778–790 (2009).

63. Myosin II activity regulates vinculin recruitment to focal adhesions through FAK-mediated paxillin phosphorylation | JCB. http://jcb.rupress.org/content/188/6/877.short.

64. Straight, A. F. *et al.* Dissecting Temporal and Spatial Control of Cytokinesis with a Myosin II Inhibitor. *Science* **299**, 1743–1747 (2003).

65. Shu, S., Liu, X. & Korn, E. D. Blebbistatin and blebbistatin-inactivated myosin II inhibit myosin II-independent processes in Dictyostelium. *Proc. Natl. Acad. Sci.* **102**, 1472–1477 (2005).

66. Surcel, A. *et al.* Pharmacological activation of myosin II paralogs to correct cell mechanics defects. *Proc. Natl. Acad. Sci.* **112**, 1428–1433 (2015).

67. Gittes, F., Mickey, B., Nettleton, J. & Howard, J. Flexural rigidity of microtubules and actin filaments measured from thermal fluctuations in shape. *J. Cell Biol.* **120**, 923–934 (1993).

68. Tomba, C. *et al.* Geometrical Determinants of Neuronal Actin Waves. *Front. Cell. Neurosci.* **11**, (2017).

69. Zhang, P. *et al.* In vivo optophysiology reveals that G-protein activation triggers osmotic swelling and increased light scattering of rod photoreceptors. *Proc. Natl. Acad. Sci.* **114**, E2937–E2946 (2017).

70. Hardie, R. C. & Franze, K. Photomechanical responses in drosophila photoreceptors. *Science* **338**, 260–264 (2012).

71. Lu, Y., Benedetti, J. & Yao, X. Light-induced length shrinkage of rod photoreceptor outer segments. *Transl. Vis. Sci. Technol.* **7**, (2018).

72. Árnadóttir, J. & Chalfie, M. Eukaryotic mechanosensitive channels. *Annu. Rev. Biophys.* **39**, 111–137 (2010).

73. Connelly, T. *et al.* G protein-coupled odorant receptors underlie mechanosensitivity in mammalian olfactory sensory neurons. *Proc. Natl. Acad. Sci.* **112**, 590–595 (2015).

74. Booth, I. R. Bacterial mechanosensitive channels: Progress towards an understanding of their roles in cell physiology. *Curr. Opin. Microbiol.* **18**, 16–22 (2014).

75. Booth, I. R., Miller, S., Müller, A. & Lehtovirta-Morley, L. The evolution of bacterial mechanosensitive channels. *Cell Calcium* **57**, 140–150 (2015).

76. Rojas, E. R., Huang, K. C. & Theriot, J. A. Homeostatic Cell Growth Is Accomplished Mechanically through Membrane Tension Inhibition of Cell-Wall Synthesis. *Cell Syst.* **5**, 578-590.e6 (2017).

77. Falleroni, F., Torre, V. & Cojoc, D. Cell mechanotransduction with piconewton forces applied by optical tweezers. *Front. Cell. Neurosci.* **12**, 1–11 (2018).

78. Delmas, P. & Coste, B. Mechano-gated ion channels in sensory systems. *Cell* **155**, 278 (2013).

79. Clapham, D. E., Runnels, L. W. & Strübing, C. The TRP ion channel family. *Nat. Rev. Neurosci.* **2**, 387–396 (2001).

80. Maroto, R. *et al.* TRPC1 forms the stretch-activated cation channel in vertebrate cells. *Nat. Cell Biol.* **7**, 179–185 (2005).

81. Neuman, K. C. & Block, S. M. Optical trapping. *Rev. Sci. Instrum.* **2787**, (2004).

82. Egawa, T. *et al.* Calcium ion and its application to multicolor neuronal Imaging. *J. Am. Chem. Soc.* 14157–14159 (2011) doi:10.1021/ja205809h.

83. Lu, Y., Wang, B., Pepperberg, D. R. & XIncheng, Y. Stimulus-evoked outer segment changes occur before the hyperpolarization of retinal photoreceptors. *Biomed. Opt. Express* **8**, 8139–8145 (2017).

84. Suchyna, T. M. *et al.* Identification of a peptide toxin from grammostola spatulata spider venom that blocks cation-selective stretch-activated channels. *J. Gen. Physiol.* **115**, (2000).

85. Spassova, M. A., Hewavitharana, T., Xu, W., Soboloff, J. & Gill, D. L. A common mechanism underlies stretch activation and receptor activation of TRPC6 channels. *Proc. Natl. Acad. Sci.* **103**, 16586–16591 (2006).

86. Bae, C., Sachs, F. & Gottlieb, P. A. The mechanosensitive ion channel Piezo1 is inhibited by the peptide GsMTx4. *Biochemistry* **50**, 6295–6300 (2011).

87. Gnanasambandam, R. *et al.* GsMTx4 : Mechanism of Inhibiting Mechanosensitive Ion Channels. *Biophysj* **112**, 31–45 (2017).

88. Bocchero, U., Tam, B. M., Chiu, C. N., Torre, V. & Moritz, O. L. Electrophysiological Changes During Early Steps of Retinitis Pigmentosa. *Invest. Ophthalmol. Vis. Sci.* **60**, 933–943 (2019).

89. Lamb, T. D. & Hunt, D. M. Evolution of the calcium feedback steps of vertebrate phototransduction. *Open Biol.* (2018).

90. Farrens, D. L. & Gobind, K. H. Structure and function of Rhodopsin. *J. Biol. Chem.* **270**, 5073–5076 (1995).

91. Molnar, T. *et al.* Store-operated channels regulate intracellular calcium in mammalian rods. *J. Physiol.* **15**, 3465–3481 (2012).

92. Williams, D. S., Hallett, M. A. & Arikawa, K. Association of myosin with the connecting cilium of rod photoreceptors. *J. Cell Sci.* **190**, 183–190 (1992).

93. Burns, M. E., Mendez, A., Chen, J. & Baylor, D. A. Dynamics of Cyclic GMP Synthesis in Retinal Rods. *Neuron* **36**, 81–91 (2002).

94. Gross, O. P. & Burns, M. E. Control of rhodopsin' s active lifetime by arrestin-1 expression in mammalian rods. *J. Neurosci.* **30**, 3450–3457 (2010).

95. Berry, J. *et al.* Effect of rhodopsin phosphorylation on dark adaptation in mouse rods. *J. Neurosci.* **36**, 6973–6987 (2016).

96. Yue, W. W. S. *et al.* Elementary response triggered by transducin in retinal rods. *Proc. Natl. Acad. Sci.* **116**, 5144–5153 (2019).

97. Vuong, T. M., Chabre, M. & Stryer, L. Millisecond activation of transducin in the cyclic nucleotide cascade of vision. *Nature* **311**, 659–661 (1984).

Appendix (side projects)

Rod photoreceptors require mechanosensitivity for optimal phototransduction

Simone Mortal[1§], Fabio Falleroni[1§], Ulisse Bocchero[1§], Trevor Lamb[2] & Vincent Torre[1,3*]

[1] Neurobiology Department, International School for Advanced Studies, Trieste, Italy

[2]Eccles Institute of Neuroscience, John Curtin School of Medical Research, The Australian National University, Canberra, ACT 2600, Australia

[3]Joint Laboratory of Biophysics and Translational Medicine, ISM-SISSA, Suzhou Industrial Park, Jiangsu, 215123, China

Corresponding Author: torre@sissa.it

Abstract

Photoreceptors are specialized cells devoted to the transduction of the incoming visual signals. Rods are able also to shed from their tip old disks and to synthetize at the base of the outer segment (OS) new disks. By combining electrophysiology, optical tweezers (OT) and biochemistry we investigate mechanosensitivity in the rods of Xenopus laevis and we show that: i- that mechanosensitive channels (MSC), TRPC1 and Piezo1 are present in rod inner segments (IS); ii- mechanical stimulation – of the order of 10 pN – applied briefly to either the OS or IS evokes calcium transients; iii- inhibition of MSCs decreases the duration of photoresponses to bright flashes; iv- bright flashes of light induce a rapid shortening of the OS; v- the genes encoding the TRPC family has an ancient association with the genes encoding families of protein involved in phototransduction. These results suggest that MSCs play an integral role in rods' phototransduction.

Introduction

Photoreceptors are thought to be specialized cells devoted to the transduction of the incoming visual signals. Nevertheless, rod photoreceptors are known to shed from their tip old disks and to synthetize at the base of the outer segment (OS) new disks. Following strong illumination rod outer segments (OSs) from mice [69] and fly photoreceptors [70] have been reported to increase their length, but rod OSs from *Xenopus laevis* frogs shrink their length by about 0.4-0.6 µm [71]. These observations indicate the existence of a mechanical machinery inside rod OSs but its action and role in phototransduction are completely unknown.

Mechanosensitive channels (MSCs) [72] are not expressed only in specialized sensory neurons but have been found in olfactory sensory neurons [73] and possibly are expressed in many - if not all - neurons of the central nervous system. In bacteria MSCc are supposed to play a major role in keeping osmotic equilibrium across their membrane especially during hypo-osmotic conditions: in these conditions, the opening of poorly selective MSCs contribute to the control of osmotic equilibrium [74]; [75]; [76]. MSCs in eukaryotic cells can be activated by light mechanical forces in the 10 pN [77].

There are now several classes of ion channels implicated in the eukaryotic mechanotransduction machinery, including TRP channels and Piezo channels [78]. The TRP channels are non-selective permeable cationic channels with a selectivity ratio Ca2+/Na+ that varies between the different family members [79]. Within the TRPC family, TRPC 1 and TRPC6 have been reported to be activated directly by membrane stretch and curvature [80].

By combining electrical recordings, OT and biochemical tools in the present manuscript we demonstrate that: i- weak mechanical stimulation – of the order of 10 pN – applied briefly to either the OS or IS evokes a clear calcium transient; ii- inhibition of MSCs decreases the duration of photoresponses to bright flashes, and the magnitude of this effect increases with flash intensity; iii- bright flashes of light induce a rapid shortening – of the order of 200-300 nm – of the rod OS; iv- the genes encoding the TRPC family of MSCs appear to have an ancient association with the genes encoding three families of protein that are directly involved in phototransduction in the rod OS. We show also that the MSCs TRPC1

and Piezo1 are present abundantly in rod inner segments; whereas, our analysis together with two proteomic studies investigating the protein composition of the disks (Panfoli et al., 2008) and of the OSs (Kwok et al., 2008), do not support their expression in OS.

Results

To investigate mechanosensitivity in rod photoreceptors we decided to use OT [81], which was used previously in our lab to trigger calcium transients in response to very weak forces, in the 10 pN range [77]. Application of this approach requires that the rods be held in an environment of high mechanical stability, for example lying on a rigid substrate, and this makes it extremely difficult to simultaneously record their electrical responses using either suction or patch pipettes. Instead, we chose to measure the functionality of rods that were isolated in this configuration by using the new infra-red-sensitive calcium indicator dye, CaSiR-1 [82]. Specifically, we loaded retinas using the AM-ester of this dye (see Methods), and then we mechanically dissociated individual rod photoreceptors and/or outer segments. We viewed the preparation using IR illumination at 750 nm and an IR-sensitive video camera attached to the microscope. Then, from regions of interest, we recorded the fluorescence emitted by CaSiR-1 upon excitation with deep red 650 nm light (Fig. 1A). This established that outer segments lacking an inner segment fluoresced intensely (Fig.1A, left inset), and showed further that this fluorescence was not reduced by illumination with green light. Thus, isolated outer segments were unresponsive to green light.

More-nearly intact rods, in which the outer segment remained connected to at least part of its inner segment, fell into two categories. On the one hand, we found one category of 'unresponsive' cells that showed no change in fluorescence upon exposure to blue light (Fig.1E). These cells were characterized by approximately uniform fluorescence along the OS, at a moderate to high level, and often showed a high level of fluorescence in the IS (Fig.1E, n >40). A second category of 'responsive' cells exhibited a distinct drop in OS fluorescence in response to blue light (Fig.1D, blue trace; n = 10), together with a marked gradient of fluorescence along the outer segment, with the basal section fluorescing only weakly (Fig.1A right inset, and Fig.1B; n > 30). We hypothesize that this second category represents functional rods, that exhibited a light-induced decrease in OS free intracellular calcium concentration, as a result of the combination of activation of the phototransduction cascade and the existence of a circulating 'dark current' (Lamb & Pugh 2006) driven by the ion gradients maintained by IS metabolism. The longitudinal gradient in OS calcium concentration is likely to arise from a gradient of Na^+-Ca^{2+}-K^+ exchanger activity along the OS, as a result of the gradient in Na^+ ion concentration

caused by longitudinal diffusion of Na^+ ions towards the 'sink' for intracellular Na^+ provided by Na-K-ATPase activity in the IS (Lamb & Pugh 2006). For the unresponsive cells (and for isolated OSs), it is plausible that there is a physical disconnect between the IS and OS that disrupts the maintenance of the required low Na^+ ion concentration in the OS.

For our experiments using OT, we conclude from the results above that we can identify the functionality of rods lying on a rigid substrate: the cells need to have been pre-loaded with CaSiR-1, and then their emitted fluorescence is viewed upon excitation with 650 nm light. Functional rods display a pronounced longitudinal gradient of emitted fluorescence, with the basal end appearing dark. In separate electrophysiological experiments we measured the effect of the 650 nm excitation light on the circulating current of functioning rods measured by presentation of a bright flash (Fig.1F). Compared with dark-adapted conditions (black trace), the circulating current in the presence of the 650 nm excitation light (red trace) was reduced to about 40% (response amplitude 14 ± 2.5 pA in darkness, and around 5.5 ± 2 pA with excitation; n = 7). Therefore, our measurements of changes in calcium concentration elicited by mechanical stimulation were performed during the equivalent of dim to moderate illumination of the rod, and we refer to this as 'semi-dark-adapted' conditions.

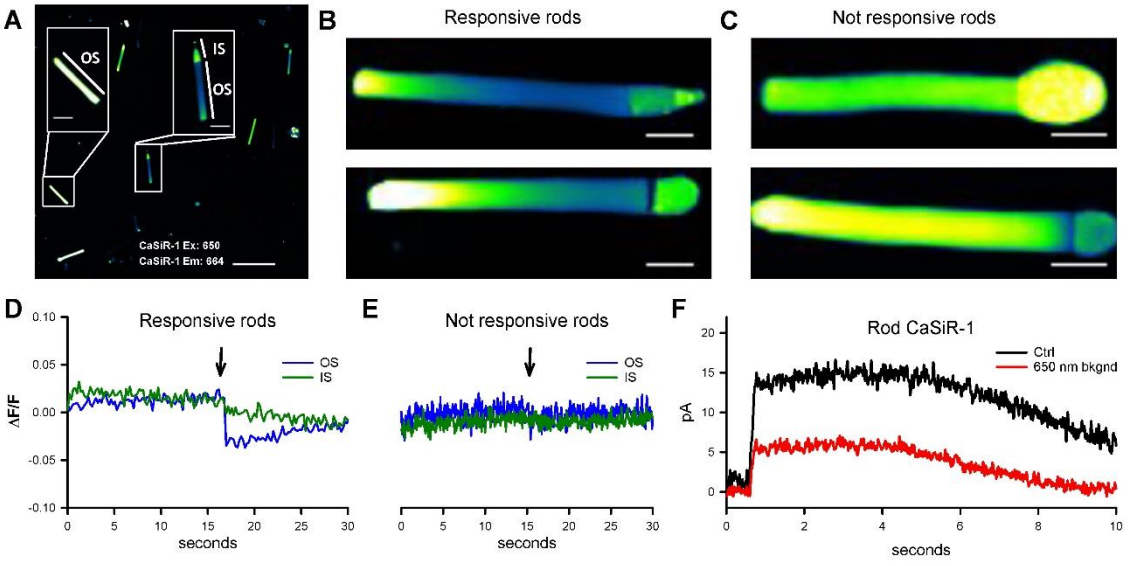

Figure 1: *Fluorescence emitted by the calcium-sensitive indicator, CaSiR-1, incorporated into rods isolated from the Xenopus laevis retina. A: Isolated rods in a dish, showing a mixture of rods comprising both an isolated OS (left) and an OS that remains*

connected to its IS (right) (scale bar 100 µm). B: Intact rods comprising an OS+IS typically display a pronounced longitudinal gradient of fluorescence, with the base of the OS quite dim. These two rods were responsive to green light, as typified by panel D (scale bar 10 µm). C: Some OS+IS exhibited fairly uniform high fluorescence along the outer segment, and were unresponsive to green light, as typified by panel E (scale bar 10 µm). D: Photoresponses from an OS+IS of the kind shown in panel B, from a ROI corresponding to 100x300 pixels of the OS (blue trace), and from an ROI corresponding to the IS (green trace). E: No photoresponse was seen from the OS of OS+IS of the kind shown in panel C. F: Suction pipette recordings in response to stimulation by bright blue flashes (~2500 photoisomerization (R)) from an OS+IS loaded with CaSiR-1, in the absence (black trace) and in the presence (red trace) of the intensity of 650 nm light used for calcium imaging in the other panels.*

Mechanosensitivity of rods

Using the criteria developed above, we identified responsive isolated rods that had been loaded with the calcium-sensitive dye CaSiR-1, and we applied mechanical stimuli of approximately 10 pN to either the OS or the IS, by means of an oscillatory optical trap (see Fig. SI 3 and [77]. In semi-dark-adapted conditions, a mechanical pulse applied to a silica bead contacting the IS (Fig.2A) evoked a local increase in fluorescence (Fig.2B), with a magnitude DF/F that could reach around 0.2 in 10–20 s (Fig.2C). The increase in fluorescence began with little delay from the mechanical stimulus (270 ms ± 80, n=12, $p < 0.05$), and the fluorescence signal remained localized to the IS, with no propagation to the OS (Fig.2B). Comparable results were obtained when the stimulating bead was touching the OS (Fig.2E): upon mechanical stimulation, the fluorescence increased locally (Fig.2F), reaching peak in about 10 s (Fig.2G), after a delay of no more than ~300 ms (Fig.2H). Collected results from 12 experiments on the IS and 8 experiments on the OS indicate a peak fluorescence increase (DF/F) of 0.14 ± 0.03 and 0.07 ± 0.01, respectively (Fig.2I and statistically different with $p < 0.05$); whereas the mean duration of these transients was around 35.1 s ± 4.05 in the IS and 33.2 s ± 4 in the OS (Fig.2L). In several experiments we repeated the same mechanical stimulation for at least three times and we observed that the initial and fast component of the calcium transients [77] was reproducible, but the second and larger component – presumably caused by the calcium release

from internal stores – declined (Fig.2 SI).In 3 experiments in which mechanical stimulation of the OS evoked a calcium transient, application of 5 □□M GsMTx-4 abolished the response to subsequent mechanical stimulation.

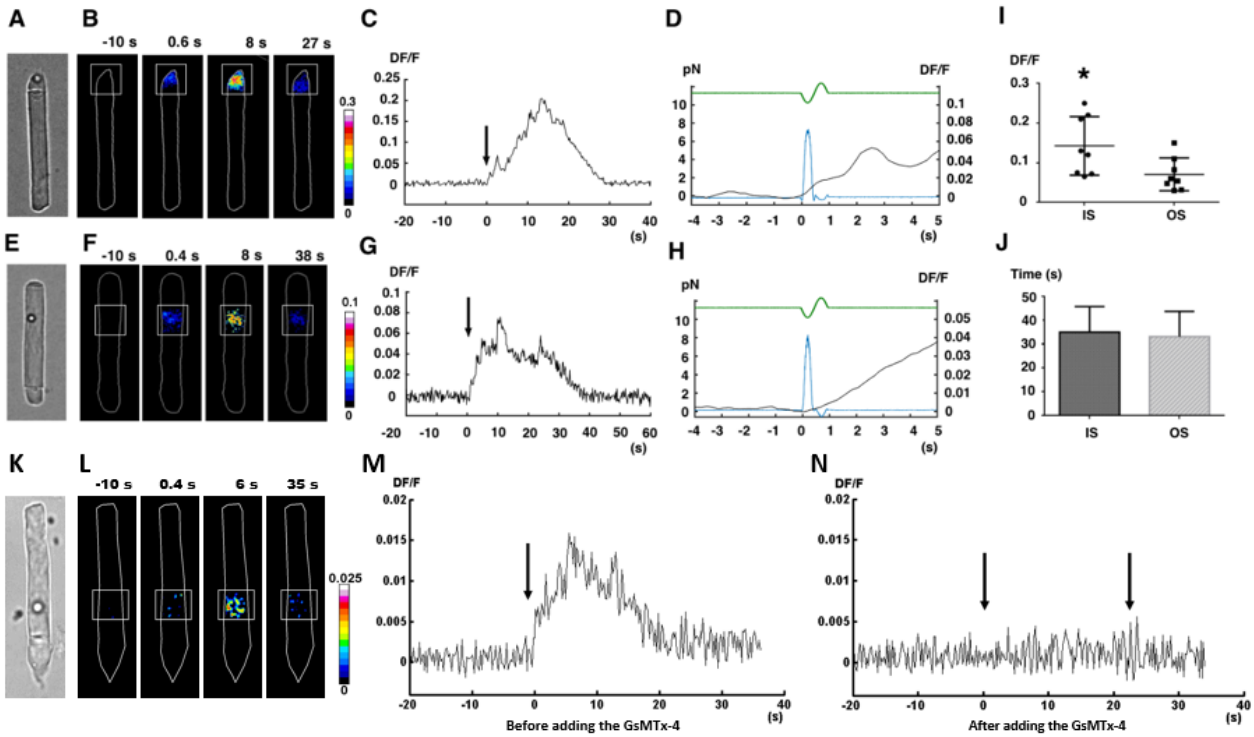

***Figure 2**: Calcium response of Xenopus leavis rods (OS+IS) to weak mechanical stimulation applied along the vertical direction. A: A trapped bead in contact with the tip of the rod IS, under bright-field IR imaging. B: Fluorescence change (DF/F) images, showing the ROI used to quantify the fluorescence change vs time. C: Time course of the evoked DF/F change from the ROI in B. Mechanical stimulation was applied at time zero, as indicated by the arrow. D: Trace from panel C on an expanded time-base, additionally showing the FTL driving command (green trace) used to move the trapped bead, and the resulting force pulse (blue trace); the force applied to the IS was about 8 pN. E, F, G and H: As in A, B, C, D but for mechanical stimulation of the rod OS. I: Collected results for peak DF/F (mean ± SD) induced by mechanical stimulation, for IS and OS respectively. J: Mean duration of calcium transients, for IS and OS respectively. A* calcium *transient was detected when DF/F was above 0.004, approximately equivalent to 5-fold the background noise. Termination of detected transients occurred when DF/F decreased below 0.004.*

These results indicate compartmentalization of calcium dynamics within the rod cytoplasm, and they suggest that rods are indeed mechanosensitive, i.e. that they express channels that can be activated by direct mechanical stimulation.

Light-induced changes in rod outer segment length

Given that *Xenopus* rods respond to mechanical stimuli, we decided to test whether they also exhibited changes in OS length upon illumination, such as the shrinkage of about 0.4–0.6 µm reported by Lu et al [7183 71]. We chose to use OT, because of its high sensitivity, of the order of 1–10 nm, and rapid temporal resolution, in the ms range [81]; see also Methods and Fig. SI 3.

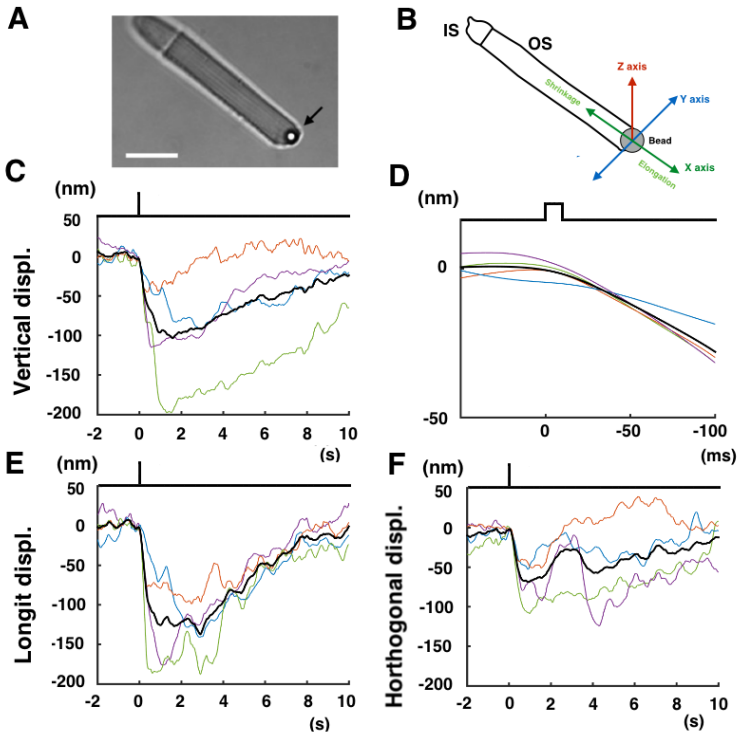

Figure 3: *Mechanical response of a Xenopus leavis rod to light flashes. The position of a bead sealed against the tip of the rod OS is monitored with OT (see Methods). Following a bright flash of 490 nm, equivalent to about 10^4 R*, a transient shrinkage is observed. A: Bright-field IR image, showing a trapped bead in contact with the tip of the rod OS (scale bar 20 µm). B: Detail of the 3D tracking system. C: Light-induced vertical shifts of the trapped bead (downward is negative). Different colors indicate traces from different OS+ISs – and each trace is the average of at least two responses and the black*

trace is the average from 5 different experiments. D: Expansion of the time-base in B, to examine the delay between light stimulus and bead movement. E: Bead displacement along the direction of the rod OS. F: Bead displacement in the direction perpendicular to the rod OS axis (shrinkage is negative and elongation is positive).

We used the OT to position a silica bead above the tip of a rod OS, and then gently lowered the bead until it made contact with the OS (Fig.3A), and then established good adhesion, as indicated by a decrease of the noise in the quadrant photodetector (QPD) trace [77]. Once the bead has sealed to the tip of the OS in this way, its precise position (monitored by the OT) provides a measure of the length of the OS, so that any light-induced changes in OS length are recorded as displacements of the bead. We were able to measure the bead displacement in the X, Y and Z directions, and we could then express the motion in terms of a longitudinal displacement in the X, Y plane along the direction of the OS (monitoring OS shrinkage or elongation) and a displacement in its orthogonal direction and along the vertical Z axis (see Fig.3B).

Fig.3 shows bead displacements in response to brief flashes delivering around 2500 R*/rod. We consistently observed a light-induced shortening of the OS, of the order of 100–200 nm in different experiments (different colors in Fig.3). The delay of the onset of the bead displacement was less than 50 ms (Fig.3C, mean 42.5 ms ± 12, n=5), which is similar to the delay in the electrical response to flashes of this intensity. The shortening was transient, and in all experiments the bead returned to its original position within about 10 s, which is again faster than recovery of the electrical response to a flash of this intensity.

To avoid the possibility of artifacts caused by the optical trap, we decided to use conventional video imaging to measure OS length. Thus, we turned off the IR laser used for optical trapping, and used IR video imaging; by comparing bright-field images obtained before and after a stimulus, we could detect small movements, though inevitably the resolution was much lower (Fig.3 SI). For isolated rods (OS+IS) visualized using 750 nm illumination, the same flash intensities as used in Fig.3 elicited shortening of the OS of 2–4 camera pixels, corresponding to approximately 100–300 nm. The combination of these two approaches confirms that flashes delivering approximately 2500 R*/rod trigger

transient shortening of *Xenopus laevis* rods, similar to that reported recently [83], who referred to it as transient retinal phototropism.

Rod photoresponses in the presence of MSC inhibitor

Given that rod photorerceptors show mechanosensitivity, we investigated their role in phototransduction by recording rod photocurrents with a suction pipette and then applying the MSC inhibitor GsMTx-4 [84]. GsMTx-4 is a small peptide obtained from a spider venom, and has been shown to inhibit several MSCs from both the Piezo and TRP families [8586]. It is thought to act at the interface between the lipids in which the MSC is embedded [87], thereby reducing the effective magnitude of the mechanical stimulus acting on the MSC gate: thus, GsMTx-4 is a gate modifier rather than a specific ion pore blocker. We delivered GsMTx-4 using a second similar pipette connected to a picospritzer and positioned 50-100 □m from the OS of the recorded rod (Fig.4A). Prior to drug exposure, presentation of bright flashes of about 2500 R*/rod [88] triggered suppression of the rod circulating current for 2–5 s (Fig.4B and C). When the inhibitor was gently injected into the bath, using around 4 psi of pressure, the OS of the recorded rod was displaced from its original position (compare upper and lower panels in Fig.4A) signaling the arrival of GsMTx-4. The same illumination then elicited photoresponses of shorter duration (compare black and red traces in Fig.4C; n=13). Subsequently, after the injection of GsMTx-4 had been terminated, the photoresponses recovered their original time course (compare black and blue traces). When the same experiment was repeated in the absence of GsMTx-4 in the pipette, but with a similar degree of OS displacement, no significant shortening of photoresponses was observed (Fig.4D and E; n=15).

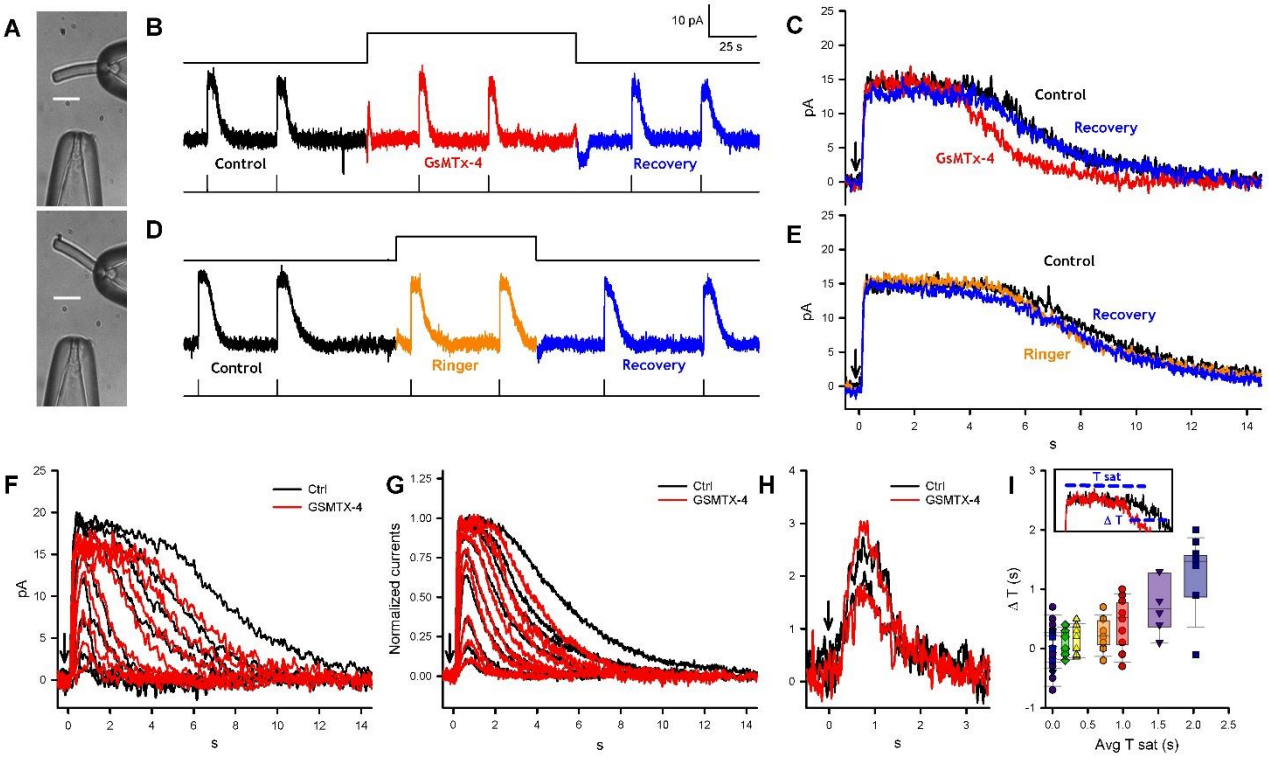

Figure 4*: The effect of MSC blocker GsMTx-4 on photoresponses from Xenopus rods. A: The upper pipette records the photocurrent of an isolated rod, while the lower pipette is connected to a picospritzer and can be used to expose the rod OS to the MSC inhibitor GsMTx-4. When the picospritzer was activated (lower panel), the rod OS tilted, and then returned to its initial position upon termination of injection (not shown)(scale bar 20 µm). B: The photocurrent elicited by flashes of about 2500 R*/rod, before, during, and after an exposure to GsMTx-4 lasting 120 s. C: Exposure to GsMTx-4 (red trace) shortens the duration of the bright-flash photoresponse by about 2 s compared with those obtained immediately before (black) and immediately after (blue) exposure to GsMTx-4; mean duration 4.7 ± 1.8 sec in control and 3.4 ± 1.3 sec when GSMTX was injected through the pipette ($p < 0.001$). D and E: As in B and C but the picospritzer injected Ringer solution. Mean duration 6.2 ± 1.7 sec in control and 5.9 ± 1.9 sec when Ringer was injected through the patch pipette with no significant statistical difference. F: Comparison of photoresponses in control conditions (black traces) and in the presence of GsMTx-4 (red traces), for one cell exposed to flash intensities of approximately 5, 10, 25, 50, 100, 250, 500, 1000 and 2500 R*/rod. G: As in F, but in this case each trace was averaged over photoresponses obtained from 6-7 different rods. The amplitude of the maximal photoresponse was normalized to unity, for recordings both in Ringer (black traces) and in the presence of GsMTx-4 (red traces). H: The effect of GsMTx-4 on dim flash*

photoresponses for one cell; the flash intensities were 5 and 10 R/rod. For each trace, 6-7 photoresponses have been averaged. I: Relation between the GSTMX-4-induced shortening (ΔT) of photoresponse duration and the saturation time (Tsat) of the response. For 250, 500, 1000 and 2500 R*/rod, the shortened time courses were of 0.3 s, $p < 0.05$; 0.5 s, $p < 0.01$; 0.7 s, $p < 0.05$ and 1.3 s, $p < 0.001$ respectively. In all experiments, the concentration of GsMTx-4 in the pipette connected to the picospritzer was 5 □M, and we estimate that the concentration reaching the rod OS following activation of the picospritzer was in the micromolar range; n= 6-7.*

We analyzed the effect of GsMTx-4 on photoresponses to flashes with intensity ranging from dim (5 R*/rod) to bright (2500 R*/rod); compare black and red traces in Fig.4F and G (n = 7 rods). Application of the MSC inhibitor had negligible effect on photoresponses to dim flashes (n = 8; Fig.4H), and it had relatively little effect for flashes of intermediate intensity (Fig.4F, G, I). It was only for flashes of saturating intensities (i.e. greater than ~100 R*/rod) that the time-course was shortened by GsMTx-4, and for these saturating flashes the magnitude of the response shortening increased with increasing flash intensity (see Fig.4I).

Relationship of the TRPC1 gene to the genes underlying vertebrate phototransduction

We examined molecular phylogeny gene and synteny for both TRPC1 and Piezo1, and we discovered that the TRPC1 gene is closely associated with several genes that encode proteins involved in the vertebrate phototransduction cascade. In particular, TRPC1 is clearly a member of the paralogon that comprises the visual GRKs, the arrestins, and the visual GCs (guanylyl cyclases). In contrast, if any such relationship exists for the Piezo1 gene, we were unable to detect it.

The syntenic relationship between the TRPCs and the three other families of genes mentioned above is summarized in Fig.5; note that, for purposes of illustration, we have chosen to show just four families and just two species from the much larger set that is presented in Supplementary Information. Each column represents the remaining members of the quartet of genes that were generated from a single ancestral gene through two rounds of whole-genome duplication (2R WGD) in a proto-vertebrate organism some 500 Mya (million years ago); thus, ARRB1, ARRB2, ARR3 and SAG arose through quadruplication of a single

ancestral arrestin gene. Each row shows a region of either one or two chromosomes in an extant organism, and where two regions are shown this is presumed to be the result of chromosomal rearrangements over 500 My. Examination of the larger dataset in SI provides powerful evidence that each of the four rows is contiguous and represents the current re-arrangement of genes on the four ancestral chromosomes that existed shortly after 2R WGD. Furthermore, for each of the four gene families, analysis of molecular phylogeny shows clear evidence of expansion during 2R WGD; for the TRPCs this is shown in Fig. SI ?, and for the GRKs, GCs and arrestins was established by Lamb & Hunt [89].

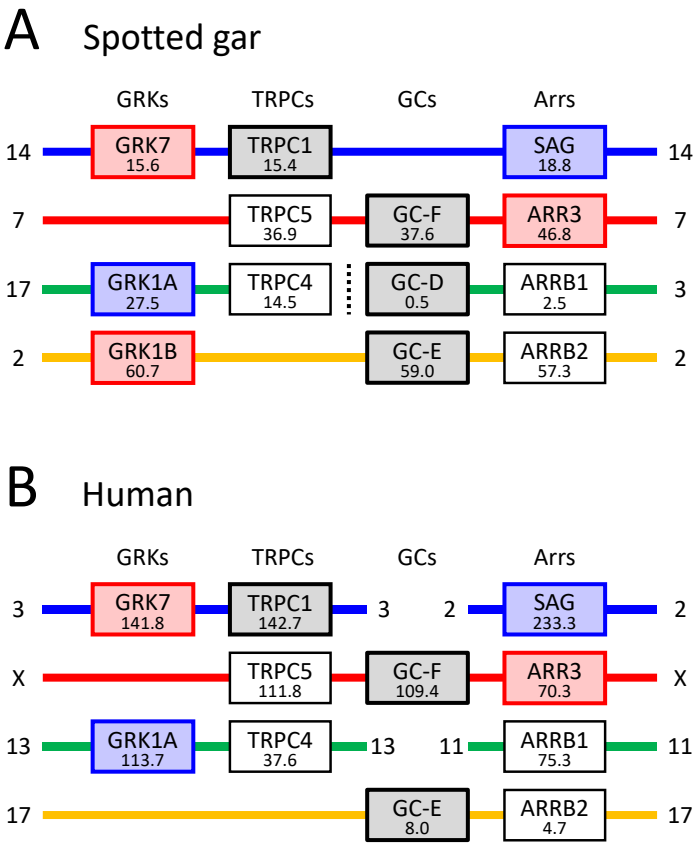

Figure 5. Summary of synteny for four gene families from two species. *Gene locations are shown for TRPCs, visual GRKs (G-protein receptor kinases), visual GCs (guanylyl cyclases), and arrestins. Number under each gene name represents the gene position in Mb on the indicated chromosome. Note that there is strong evidence that each interrupted row (where there is a break in continuity of a chromosome) corresponds*

to a contiguous set of genes in the ancestral quadruplicated genome. See Fig. SI Y and Table SI Y for synteny across XX gene families and four species.

In Fig.5, the proximity of TRPC family members to members of the other three families is impressive. For example, the distance from TRPC1 to GRK7 is just 0.2 Mb in both spotted gar (Fig.5A) and chicken (Fig. SI ?B), and is <1 Mb in both human (Fig. 6B) and opossum (Fig. SI ?C). Likewise, the distance from TRPC5 to GC-F (=*GUCY2F*) is <1 Mb in spotted gar (Fig.5A) and <2.5 Mb in human (Fig.5B); in the other two species, the loss of the gene for GC-F precludes this comparison. Furthermore, as shown previously [89], in several cases members of the other three families of phototransduction genes are close to each other; e.g. GRK1B, GE-E and ARRB2 are close to each other in spotted gar (Fig. 6A). Such proximity in extant chromosomes is an important telltale sign of ancient proximity, because of the very low likelihood that random chromosomal rearrangements could bring so many genes into mutual proximity; instead, random rearrangements are likely to obscure any proximity that originally occurred. Therefore, we conclude that it is very likely that in a proto-vertebrate organism the ancestral genes (TRPC, visual GRK, visual GC, and arrestin) were arranged in close proximity to each other, prior to quadruplication during 2R WGD.

Localization of MSCs in Xenopus laevis rods

To better investigate the expression of MSCs Piezo1 and TRPC1 in rods, we stained retinas by immunofluorescence, with antibodies for Piezo1 and TRPC1 MSC (see Methods). Immunolabelling for Piezo1 (Fig.6A) shows a clear staining in rods, with a punctate expression in the ellipsoid region of the IS, whereas TRPC1 staining displays a broader expression along the OS (Fig.6B). However, from these images we were not able to determine conclusively whether TRPC1 channels were located also in OS. Indeed, the significant presence of autofluorescence in rod OSs, presumably associated to the high density of rhodopsin molecules [90] could be responsible of a false positive detection of TRPC1 in rod OS and the bright green staining of Fig.6B could be an artifact.

[91]TRPC1 are expressed mostly in rod inner segments in mouse, using RNA in situ hybridization with nitroblue tetrazolium. To get clearer evidences on the expression patterns of TRPC1, we decide to perform immunohistochemical staining of Xenopus retinas with the same antibody used for the immunofluorescence. Indeed, immunohistochemical staining confirmed that TRPC1 is expressed primarily on the IS membrane of rod photoreceptors (Fig.6C) with possible weaker staining also in the OSs. We isolated OS (Fig.6D), IS+OS by purification on a sucrose density gradients (McDowell 1993) and we performed standard WB with antibodies for TRPC1 and Piezo 1 (Fig6E) . This analysis shows that TRPC1 and Piezo 1channels are abundantly present in the retina and in ISs , but not in the OSs(Fig.6D). This conclusion is in agreement with the conclusions of previous proteomic studies (Panfoli et al., 2008; Kwok et al., 2008) which did not report the presence of Piezo and TRP channels neither in OS nor in discs. We were not able to determine by WB analysis the presence or absence of TRPC1 and Piezo1 channels in a population of isolated and purified disks (data not shown).

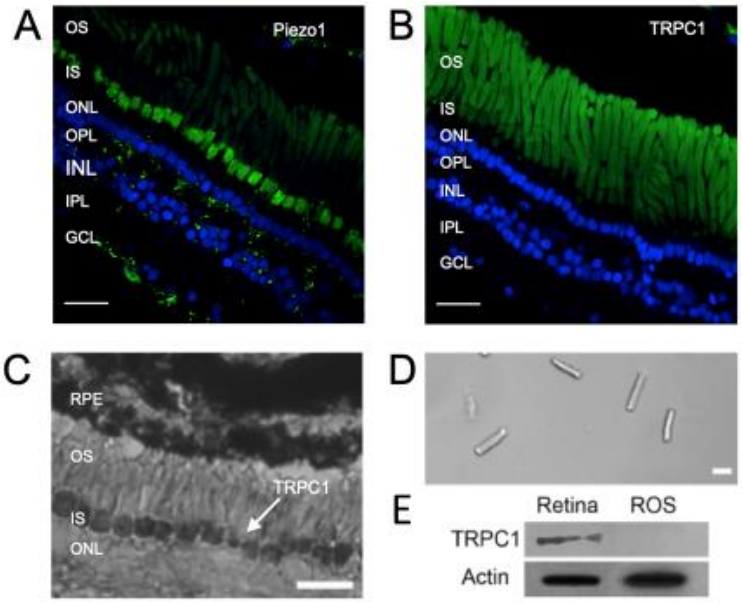

Figure 6: *Expression of mechanosensitive channels in the Xenopus laevis retina: A: immunofluorescence for TRPC1 in green and DAPI in blue. B: immunofluorescence for Piezo1 in green and DAPI in blue. C: immunohistocemistry for TRPC1. D: isolated OS obtained by sucrose centrifugation; E: western blot for TRPC1 from the whole retina and isolated ROS as those shown in D.*

Discussion

The present manuscript shows a number of novel features of rod photoreceptors involving mechanosensitivity and mechanosensitive channels. TRPC1 and Piezo1 MSCs are present in rod photoreceptors; in addition, it has long been known that the actomyosin complex is associated with the ciliary machinery linking the light-sensitive OS to the IS [92]. Interestingly, weak mechanical stimulation – of the order of 10 pN – applied briefly to either the OS or IS evoke clear calcium transients, which are inhibited by the toxin GsMTx-4. Moreover, the inhibition of MSCs through GsMTx-4 decreases the duration of photoresponses to bright flashes, and the magnitude of this effect increases with flash intensity. The genes for the TRPC family appear to have an ancient association with the genes for three other families of genes that are directly involved in phototransduction in the rod OS. These results suggest that MSCs play an integral role in the regulation of rod phototransduction.

Both TRPC1 and Piezo1 channels are multimodal, and have been reported to be gated and modulated by temperature and second messengers. The observation that very weak mechanical stimulation of the IS elicits a transient increase in intracellular calcium concentration is consistent with the view that these ionic channels in the IS are mechanosensitive. Mechanosensitivity in OSs seems to have a more complex origin: weak mechanical stimulations evoke brief calcium transients (Fig.1) but we have not been able to determine in a conclusive way the presence of TRPC1 and Piezo1 and 2 channels in OSs. It is possible, however, that in the OSs there are additional MSCs or that mechanosensitivity has a different origin: it is conceivable, indeed, that the small indentation occurring during the applied mechanical stimulations – in the order of some hundreds of nm – disrupt disks, known to be filled by calcium ions (Chen et al., 2002) and therefore inducing a localized transient calcium increase. In some experiments (see SI 4), we observed that in the presence of GSMTX-4 mechanical stimulations did not evoke any calcium transients, but spontaneous calcium transients could be observed. This observation suggests that calcium transients could occur in absence of any apparent mechanical stimulation and that mechanical stimulations could modulate and increase the frequency of these transients.

We observed that GsMTx-4 caused a shortening of the duration of bright flash responses (Fig. 4B and C). The exposure to GSMTX-4 does not induce any measurable change in the amplitude of the saturating current (Fig.4C), indicating either that MSCs are not activated in dark adapted conditions, i.e. before the exposure to the bright light and/or that the ionic current flowing through MSCs is small and cannot be easily measured. On the basis of these observations, we suggest that in the presence of GSMTX-4, a bright flash results in a more pronounced light-induced drop in calcium concentration because the MSCs are inhibited. Thus, the inhibition of MSCs will block an influx of calcium into the cytoplasm, that is normally stimulated by mechanical movement of the OS triggered by the bright flash, and thereby result in a larger decline in free calcium concentration. The ensuing shortening of the bright-flash photoresponses could result from an effect of the lowered calcium concentration via either increased cyclase activity [93] or decreased R* lifetime [94;95], or both.

If MSC channels are activated during phototransduction, a key issue is *what mechanical stimulation activates them*? Three possibilities spring to mind: activation of the actomyosin complex; a drop of intracellular osmotic pressure caused by the transient abolition of the photocurrent and dimensional changes, such as the light induced shortening of the rod OS (Fig.3 and [83], 2018). We suggest that the first of these is unlikely, because although the IS is rich in actin but in the OS actin is present only at its base and is not present in the whole OS (see Fig.6).

We have not been able to estimate the magnitude of any light-induced change in intracellular osmotic pressure, though we expect it will be small. Although suppression of the dark current of 50 pA corresponds to a reduction in the entry into the OS of around $3x10^8$ monovalent cations per s, this is counterbalanced by an equal reduction of current flow out of the OS and into the IS (Lamb & Pugh 2006). Therefore following a saturating flash of light, it is possible the development of a drop of the osmolarity but the cessation of the ionic flux through the light sensitive channels is likely to be compensated by a the cessation of an equal flux of positive charge from the outer segment to the inner segment through the ciliary neck. Furthermore, we are not aware of any experimental evidence for a significant change in intracellular ionic concentration during the light response.

In agreement with previous observations [83], we confirm that bright flashes of light elicit a transient shortening of the rod OS. These light flashes-induced movements begin with a delay around 50 ms for a flash of about 2500 R*/rod (Fig.3) not longer than the onset of the suppression of the photocurrent. This transient shortening of OSs, also referred as transient retinal phototropism is thought to be associated with early, disk-based stages of the phototransduction cascade [83], and is not caused by the light-induced suppression of the photocurrent. Transmission electron microscopy shows that the shrinkage is associated with a decrease in the space between disks, rather than any change in thickness of the disk itself [83], and this decrease in OS cytoplasmic volume will necessarily cause an increase in osmotic pressure. Hence, we propose that activation of MSCs is elicited either directly by the change in inter-disk spacing (especially if MSC channels are located in the disk membranes), or secondarily by the change in cytoplasmic osmotic pressure. We are aware, however, that this reduction of inter-disk spacing will initiate adjustments of the hydrostatic pressure and of water volume, which have to be properly addressed and understood.

The transient shortening of rod OS is likely to play a major role in phototranduction, which is at the moment not entirely understood. This shortening is associated to the early stages of phototransduction occurring within some tens of milliseconds following rhodopsin activation [83] and it is not clear how the biochemical cascade initiated by the absorption of photons by rhodopsin lead to a shrinkage of the inter-disk space: we strongly believe that this shrinkage represents a missing step for a complete and full understanding of phototransduction. We speculate that the activation of phosphodiesterase, which occurs in the OS cytoplasm [96] and in the inter-disk space before the suppression of the photocurrent [97] could be involved - or even responsible - of this shrinkage.

Although it is widely thought that sensory neurons (such as photoreceptors) are specialized to transduce just a single sensory modality, the present investigation shows that rods not only express mechanosensitive channels but also demonstrated that they display mechanosensitivity. We hypothesize that rod photoreceptors require such mechanosensitivity, firstly for the optimal operation of the phototransduction machinery, and for the maintenance of cellular integrity through processes such as disk shedding.

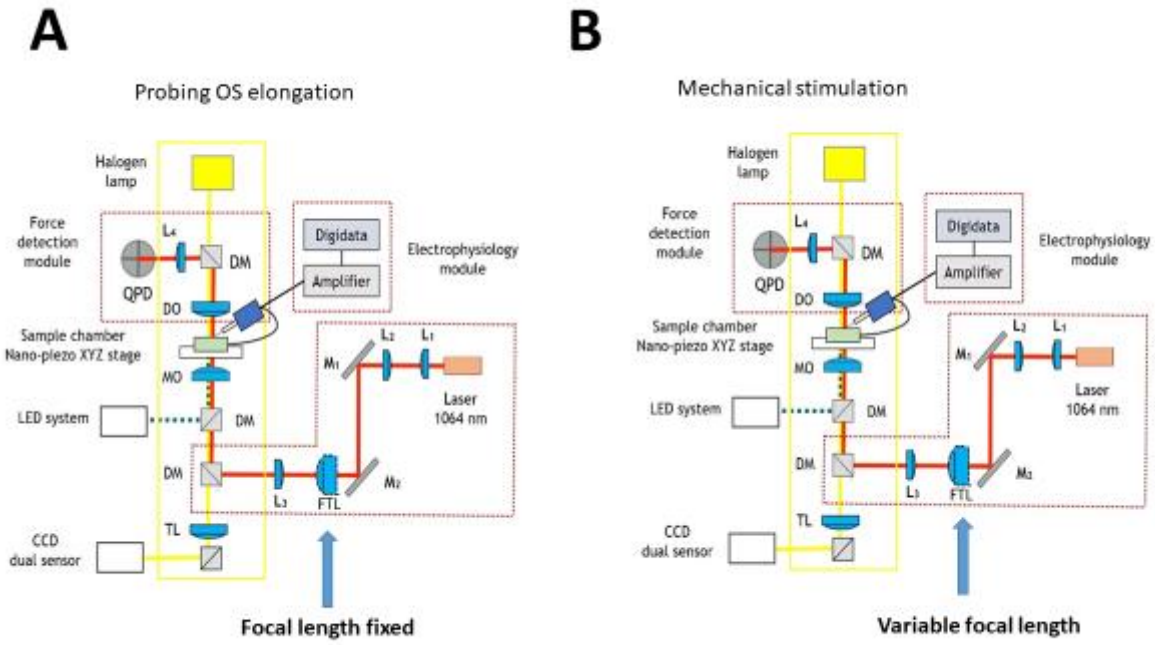

Fig. SI 1: Optical manipulation and imaging setup Optical manipulation and imaging setup: 1, inverted microscope; 2, oscillatory optical trap OOT; 3, Force measurement module. Optical components: L1, L2, convergent lenses, f1 = f2 = 100mm; M1, mirror; FTL, Focus Tunable Lens, fFTL = 55–90mm; FL, Fixed focal Lens, f = 150mm; DM1, dichroic mirror (900 dcsp, Chroma); DM2, dichroic mirror (XF22045, Chroma); TL, Tube Lens; MO, Microscope Objective, Olympus 60X, NA 1.4, oil immersion; DO, condenser objective, 10 X, NA 0.3; DM3, Dichroic Mirror (900dcsp, Chroma); L3, convergent lens, f = 40mm; QPD, Quadrant Photo Diode.

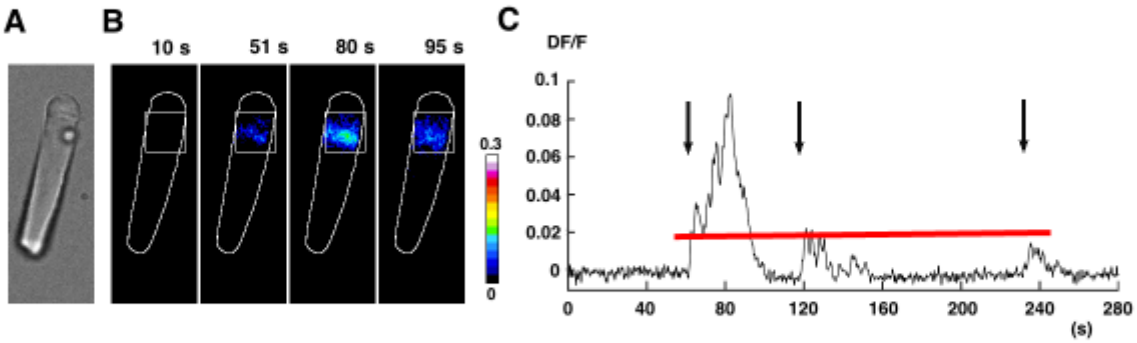

Fig2 SI: The effect of repeated mechanical stimulations: A: A: trapped bead in contact with the tip of the rod OS, under bright-field IR imaging. B: Fluorescence change (DF/F) images, showing the ROI used to quantify the fluorescence change vs time C: Calcium transients evoked by the repeated mechanical stimulations (indicated by the dark arrow). The amplitude of the first and fast calcium transient (indicated by the horizontal red line) is reproducible, while the second and larger component declines.

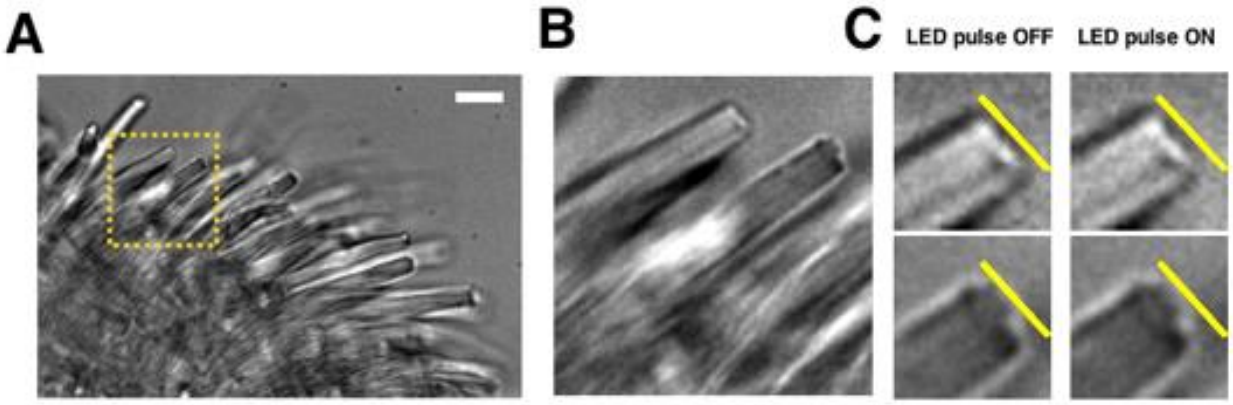

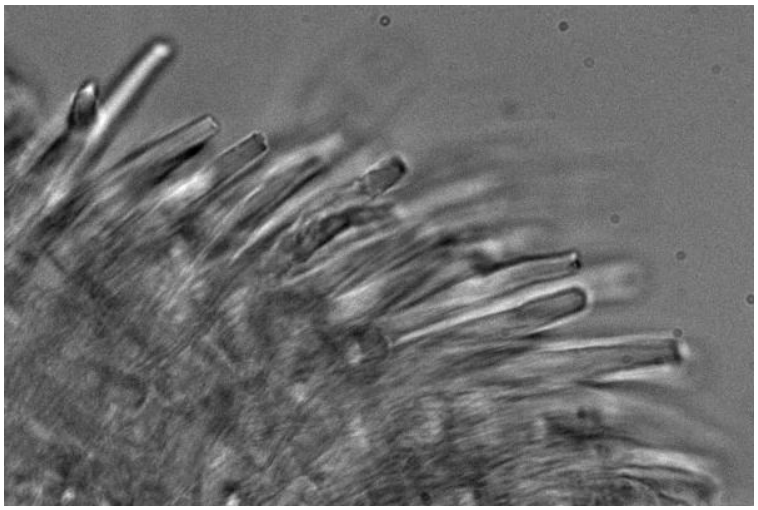

Fig.3 SI: Video imaging of the effect of light on the length of rod OS. A: a Bright field view of a piece of retina under IR light at 750 bn. B: zoom of the yellow dotted box in A. C: zoom of the tips of OS in the yellow dotted squares before, during illumination and after 20 sec. The light induced shortening of the rod OS correspond to 2-4 pixels: given that a pixel corresponds to approximately 120 nm the shortening is in the order of 200-400 nm. The enclosed video provides addi tional support to the light induced OS shortening.

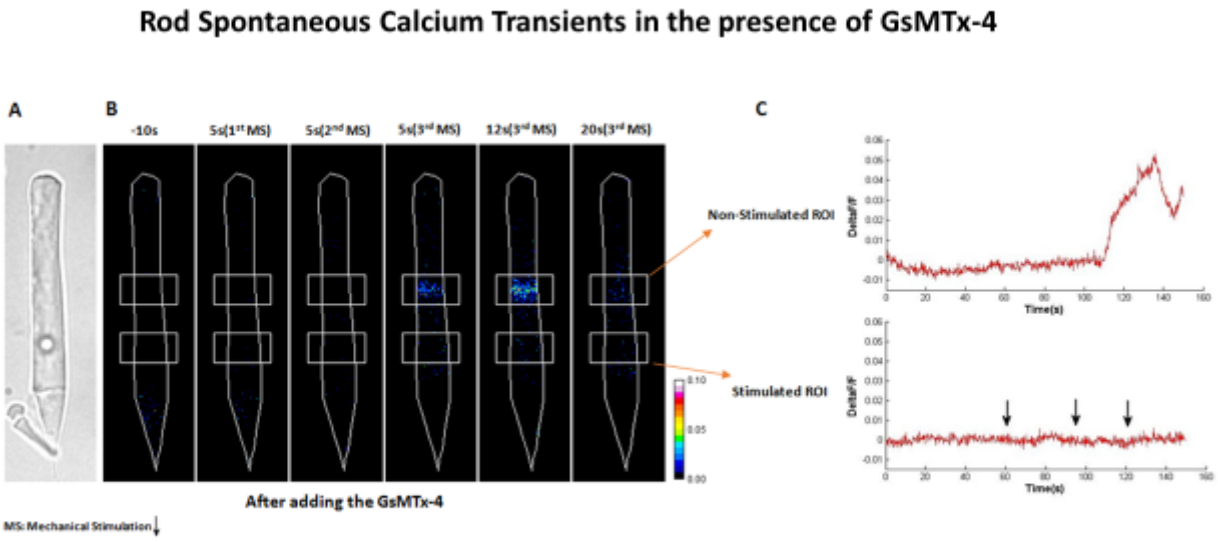

Fig.4 SI: Spontaneous calcium transients in the presence of GSMTX-4. A: A trapped bead in contact with the rod OS, under bright-field IR imaging. B: Fluorescence change (DF/F) images, showing the two ROIs used to quantify the fluorescence change vs time. C: Time course of the evoked DF/F change from the two ROIs in B. Mechanical stimulation (MS) as indicated in B . In the presence of GSMTX-4 mechanical stimulation did not evoke any calcium transients, but spontaneous calcium transients could be observed.

Methods

Immunofluorescence

Retinas were fixed with 4% paraformaldehyde for 60 min at room temperature followed by permeabilization with PBS plus 0.1% Triton X-100, blocked with 1% BSA (Bovine Serum Albumin) and incubated overnight with primary antibodies anti Piezo1 (1:300) or anti Trpc1(1:300) from Alomone Labs. Retinas were then washed with cold PBS three times for 5 min each, and incubated with Alexa 488-labeled goat anti-mouse secondary antibody (1:400) or Alexa 594-labeled goat anti-rabbit secondary antibody (1:400) and and Actin (Phalloidin) (1:50) at room temperature for 1 h and then stained with Hoechst (all from Life Technology). Retinas were examined with a NIKON A1R confocal microscope equipped with 405, 488 and 561 excitation lasers, 40x objective (NA 0.75) and 60x oil immersion objective (NA 1.40).

Isolation of Photoreceptors and electrical recordings

Eyes of Xenopus laevis were enucleated and hemisected under infrared 820-nm illumination. Dissociated rods were obtained as reported previously (Bocchero et al 2018). Isolated intact rods obtained by mechanical dissociation were immersed in Ringer solution containing (in mM) 110 NaCl, 2.5 KCl, 1 $CaCl_2$, 1.6 $MgCl_2$, and 3 HEPES-NaOH, 0.01 EDTA, and 10 glucose (pH 7.7–7.8 buffered with NaOH). All chemicals were purchased from Sigma-Aldrich (St. Louis, MO, USA). All experiments were performed at 22°C to 24°C. Images were acquired using HCImage software 4.3.1.33 (Hamamatsu Corporation, Bridgewater, NJ, USA).

After mechanical isolation, electrical recordings were obtained as described in Bocchero et al 2018. Rods were viewed under 900-nm light using two cameras (Hamamatsu ORCA-Flash 4.0; Hamamatsu Corporation, Bridgewater, NJ, USA; and Jenoptic ProgRes MF; JENOPTIK I Optical Systems, Goeschwitzer, Jena, Germany) at two magnifications and stimulated with 491-nm diffuse light (Rapp OptoElectronic, Hamburg, Germany) from the ×10 objective of an inverted microscope (Olympus IX71; Olympus Corporation, Tokyo, Japan). Photoresponses were recorded using an Axopatch 200A (Molecular Devices, LLC., San Jose, CA, USA) in voltage clamp-mode. The current was

low-pass filtered at 20 Hz and digitized at 100 Hz. All recordings were processed, analyzed, and baselines corrected with Clampfit 10.3 (Molecular Devices).

Calcium Imaging

Retinas were loaded with a cell-permeable calcium dye CasIR-AM (Life Technologies) and Pluronic F-127 20% solution in DMSO (Life Technologies) at a ratio of 1:1 in Krebs-Ringer's solution containing 119 mM NaCl, 2.5 mM KCl, 1 mM NaH_2PO_4, 2.5 mM $CaCl_2$, 1.3 mM $MgCl_2$, 11 mM D-glucose, and 20 mM HEPES (pH 7.4) at 37°C for 45 min. After incubation the isolated rods were washed three times for at least 15 min total to allow complete intracellular de-esterification of the dye then transferred to the stage of an Olympus IX-81 inverted microscope equipped with LED illumination (X-Cite XLED1 from Excelitas Technologies). The experiments were performed at room temperature (between 22 and 24 C), and images were acquired using Micromanager software with an Apo-Fluor 60x/1.4 NA objective at a sampling rate of 5 Hz for 3–10 min.

Mechanical l Stimulation Using the Oscillatory Optical Trap

To mechanically stimulate the cell, we used a polystyrene bead with a diameter d = 3.5-µm diameter (G. Kisker GbR,) optically manipulated in an oscillatory optical trap (OOT) (Fig. 1 SI). The main component of the OOT is the Focused Tunable Lens (EL-10-30-NIR-LD, Optotune AG), of which its focal length can be precisely tuned to change the vertical position of the trapped bead. Cell stimulation is achieved by trapping the bead above the cell and then moving it against the cell membrane. A complete description of all components of the used set-up are found in Falleroni et al 2018. The set-up can be used for measuring displacements (Fig.5) and for applying forces (Fig.4) and the shift from the two modes of operation is obtained by inserting in the optical path of the laser the Focused Tunable Lens when applying forces (see Fig. 1 SI).

Data and Statistical Analysis

For calcium experiment the DF/F was quantified by custom developed code Matlab (MathWorks, Inc.) and Imagej software v1.6 (National Institutes of Health). All the results are presented as mean ± SD and statistically differences were determined using a t-test, as appropriate with $p < 0.05$ considered statistically significant (GraphPad Prism 7, GraphPad software, San Diego, CA).

For electrophysiological experiments, the parameters of rod responses were analyzed with Clampfit 10.3 and the statistical significance was determined using the paired t-test in SigmaPlot 13.0.

Bibliography

Árnadóttir, J., and Chalfie, M. (2010). Eukaryotic mechanosensitive channels. Annu. Rev. Biophys. *39*, 111–137.

Bae, C., Sachs, F., and Gottlieb, P.A. (2011). The mechanosensitive ion channel Piezo1 is inhibited by the peptide GsMTx4. Biochemistry *50*, 6295–6300.

Berry, J., Frederiksen, R., Yao, Y., Nymark, S., Chen, J., and Cornwall, C. (2016). Effect of rhodopsin phosphorylation on dark adaptation in mouse rods. J. Neurosci. *36*, 6973–6987.

Bocchero, U., Tam, B.M., Chiu, C.N., Torre, V., and Moritz, O.L. (2019). Electrophysiological Changes During Early Steps of Retinitis Pigmentosa. Investig. Ophthalmol. Vis. Sci. *60*, 933–943.

Booth, I.R. (2014). Bacterial mechanosensitive channels: Progress towards an understanding of their roles in cell physiology. Curr. Opin. Microbiol. *18*, 16–22.

Booth, I.R., Miller, S., Müller, A., and Lehtovirta-Morley, L. (2015). The evolution of bacterial mechanosensitive channels. Cell Calcium *57*, 140–150.

Burns, M.E., Mendez, A., Chen, J., and Baylor, D.A. (2002). Dynamics of Cyclic GMP Synthesis in Retinal Rods. Neuron *36*, 81–91.

Chen, C., Jiang, Y., and Koutalos, Y., (2002). Dynamic behavior of rod photoreceptor Disks. Biophysical Journal 83(3), 1403–1412

Clapham, D.E., Runnels, L.W., and Strübing, C. (2001). The TRP ion channel family. Nat. Rev. Neurosci. *2*, 387–396.

Connelly, T., Yu, Y., Grosmaitre, X., Wang, J., Santarelli, L.C., Savigner, A., Qiao, X., Wang, Z., Storm, D.R., and Ma, M. (2015). G protein-coupled odorant receptors underlie mechanosensitivity in mammalian olfactory sensory neurons. Proc. Natl. Acad. Sci. *112*, 590–595.

Delmas, P., and Coste, B. (2013). Mechano-gated ion channels in sensory systems. Cell *155*, 278.

Egawa, T., Hanaoka, K., Koide, Y., Ujita, S., Takahashi, N., Ikegaya, Y., Matsuki, N., Terai, T., Ueno,

T., Komatsu, T., et al. (2011). Calcium ion and its application to multicolor neuronal Imaging. J. Am. Chem. Soc. 14157–14159.

Falleroni, F., Torre, V., and Cojoc, D. (2018). Cell mechanotransduction with piconewton forces applied by optical tweezers. Front. Cell. Neurosci. *12*, 1–11.

Farrens, D.L., and Gobind, K.H. (1995). Structure and function of Rhodopsin. J. Biol. Chem. *270*, 5073–5076.

Gnanasambandam, R., Ghatak, C., Yasmann, A., Nishizawa, K., Sachs, F., Ladokhin, A.S., Sukharev, S.I., and Suchyna, T.M. (2017). GsMTx4 : Mechanism of Inhibiting Mechanosensitive Ion Channels. Biophysj *112*, 31–45.

Gross, O.P., and Burns, M.E. (2010). Control of rhodopsin' s active lifetime by arrestin-1 expression in mammalian rods. J. Neurosci. *30*, 3450–3457.

Hardie, R.C., and Franze, K. (2012). Photomechanical responses in drosophila photoreceptors. Science (80-.). *338*, 260–264.

Michael C. M. Kwok, Juha M. Holopainen, Laurie L. Molday, Leonard J. Foster, Robert S. Molday (2008). Proteomics of photoreceptor outer segments identifies a subset of SNARE and Rab proteins implicated in membrane vesicle trafficking and fusion. Molecular & Cellular Proteomics, (6) 1053-1066.

Lamb, T.D., and Hunt, D.M. (2018). Evolution of the calcium feedback steps of vertebrate phototransduction. Open Biol.

Lu, Y., Wang, B., Pepperberg, D.R., and XIncheng, Y. (2017). Stimulus-evoked outer segment changes occur before the hyperpolarization of retinal photoreceptors. Biomed. Opt. Express *8*, 8139–8145.

Lu, Y., Benedetti, J., and Yao, X. (2018). Light-induced length shrinkage of rod photoreceptor outer segments. Transl. Vis. Sci. Technol. *7*.

McDowell, H. Preparing Rod Outer Segment Membranes, Regenerating Rhodopsin, and Determining Rhodopsin Concentration Methods in Neurosciences Volume 15, 1993, Pages 123-130

Maroto, R., Raso, A., Wood, T.G., Kurosky, A., Martinac, B., and Hamill, O.P. (2005). TRPC1 forms the stretch-activated cation channel in vertebrate cells. Nat. Cell Biol. *7*, 179–185.

Molnar, T., Barabas, P., Birnbaumer, L., Punzo, C., Kefalov, V., and Kriz, D. (2012). Store-operated channels regulate intracellular calcium in mammalian rods. J. Physiol. *15*, 3465–3481.

Neuman, K.C., and Block, S.M. (2004). Optical trapping. Rev. Sci. Instrum. *2787*.

Panfoli, I., Musante, L., Bachi, A., Ravera, S., Calzia, D., Cattaneo, A., Bruschi, M., Bianchini, P., Diaspro, A., Morelli, A., Pepe, I.M., Tacchetti, C., and Candiano, G. (2008). Proteomic Analysis of the Retinal Rod Outer Segment Disks. Journal of Proteome Research 2008 7 (7), 2654-2669

Rojas, E.R., Huang, K.C., and Theriot, J.A. (2017). Homeostatic Cell Growth Is Accomplished Mechanically through Membrane Tension Inhibition of Cell-Wall Synthesis. Cell Syst. *5*, 578-590.e6.

Spassova, M.A., Hewavitharana, T., Xu, W., Soboloff, J., and Gill, D.L. (2006). A common mechanism underlies stretch activation and receptor activation of TRPC6 channels. Proc. Natl. Acad. Sci. *103*, 16586–16591.

Suchyna, T.M., Johnson, J.H., Hamer, K., Leykam, J.F., Gage, D.A., Clemo, H.F., Baumgarten, C.M., and Sachs, F. (2000). Identification of a peptide toxin from grammostola spatulata spider venom that blocks cation-selective stretch-activated channels. J. Gen. Physiol. *115*.

Vuong, T.M., Chabre, M., and Stryer, L. (1984). Millisecond activation of transducin in the cyclic nucleotide cascade of vision. Nature *311*, 659–661.

Williams, D.S., Hallett, M.A., and Arikawa, K. (1992). Association of myosin with the connecting cilium of rod photoreceptors. J. Cell Sci. *190*, 183–190.

Yue, W.W.S., Silverman, D., Ren, X., Frederiksen, R., Sakai, K., Yamashita, T., Shichida, Y., Cornwall, M.C., Chen, J., and Yau, K.-W. (2019). Elementary response triggered by transducin in retinal rods. Proc. Natl. Acad. Sci. *116*, 5144–5153.

Zhang, P., Zawadzki, R.J., Goswami, M., Nguyen, P.T., Yarov-Yarovoy, V., Burns, M.E., and Pugh, E.N. (2017). In vivo optophysiology reveals that G-protein activation triggers osmotic swelling and increased light scattering of rod photoreceptors. Proc. Natl. Acad. Sci. *114*, E2937–E2946.